IMPLEMENTING THE MATERIALS GENOME INITIATIVE: BEST PRACTICES FOR DEVELOPING MEANINGFUL EXPERIMENTAL DATA SETS IN ALUMINUM-ZINC-MAGNESIUM-COPPER ALLOYS

A Thesis
Presented to
The Academic Faculty

by

Ashley Nelson Goulding

In Partial Fulfillment
of the Requirements for the Degree
Doctor of Philosophy in the
School of Material Science and Engineering

Georgia Institute of Technology
May 2016

IMPLEMENTING THE MATERIALS GENOME INITIATIVE: BEST PRACTICES FOR DEVELOPING MEANINGFUL EXPERIMENTAL DATA SETS IN ALUMINUM-ZINC-MAGNESIUM-COPPER ALLOYS

Approved by:

Dr. Tom H. Sanders Jr., Co-Advisor
School of Materials Science and Engineering
Georgia Institute of Technology

Dr. Richard W. Neu, Co-Advisor
George W. Woodruff School of Mechanical Engineering
School of Materials Science and Engineering
Georgia Institute of Technology

Dr. Preet Singh
School of Materials Science and Engineering
Georgia Institute of Technology

Dr. David L. McDowell
George W. Woodruff School of Mechanical Engineering
School of Materials Science and Engineering
Georgia Institute of Technology

Dr. Seung-Kyum Choi
George W. Woodruff School of Mechanical Engineering
Georgia Institute of Technology

Date Approved: April 4, 2016

Later on, when they had all said "Good-bye" and "Thank-you" to Christopher Robin, Pooh and Piglet walked home thoughtfully together in the golden evening, and for a long time they were silent.

"When you wake up in the morning, Pooh," said Piglet at last, "what's the first thing you say to yourself?"

"What's for breakfast," said Pooh. "What do you *say, Piglet?"*

"I say, I wonder what's going to happen exciting today*?" said Piglet.*

Pooh nodded thoughtfully. "It's the same thing," he said.

For Sean,

and for breakfast sandwiches.

ACKNOWLEDGEMENTS

As with any large body of work or life milestone, this dissertation would not have been possible without the assistance and support of an extremely long list of people. First and foremost on this list are my co-advisors. I must begin by thanking Professor Richard Neu for all of the support and advice he has provided on this project, as well as the plethora of opportunities he has provided me with to grow, not only as a researcher, but also as a mentor, a manager, and a whole person. I also have to profusely thank Professor Tom Sanders, without whom I surely would have quit grad school years ago. Despite everything, or perhaps because of it, he has pushed me and challenged me to be more and do more than I ever thought I possibly could. Under his mentorship I have grown as a teacher, a mediator, and as a friend.

I have also been fortunate to have on this project a truly wonderful committee in Professors David McDowell and Preet Singh, as well as Assistant Professor Seung-Kyum Choi, who have provided me not only with advice and thoughts on the project and its impact, but also on my personal impact and my career moving forward. I'd also like the thank Professors Arun Gohkale and Surya Kalidindi for various discussions throughout the course of this project, which were immensely helpful. The experimental work that was conducted in this project was immense and required the help of several undergraduate students. Most notably I'd like to thank Chris Stephens, Marika Manuud, and Hayden McLeod, for possibly being the best team of undergrads I could have asked to work with for the last year of this project. I'd also like to acknowledge Blake Cotney, Tushar Gupta, Thiago Alvim, and Chris Hauser,

who all assisted with aspects of this project in various ways. In addition to the students who assisted this work, I'd also like to thank my colleagues who supported various parts of the project, including our MPRL research technician JD Huggins and Nathan Maudlin in the machine shop.

Additionally, everyone has colleagues and co-workers, but not everyone has colleagues they can also call friends. In particular, I'd like to thank Kyle Brindley, my co-lab manager at MPRL, my travel buddy, and one of my closest friends. Other members of both research groups, past and present must include Mike Kirka, Sean Neal, Sanam Gorgannejad, Ernesto Estrada, Justin Lamb, and Judy Dickson. It has been such a huge pleasure working with you all. I'd also like the thank my academic mom, Susan Bowman, for being there for me for every step of this process, and for being so gracious as to schedule her retirement so that it coincided with my defense. I'm also particularly grateful to my friends all across the Georgia Tech campus, for all of the support they've shown me and the joy that we've shared. In particular, I'd like to thank Cait Meree, Ken Pradel, Philip Brooke, Gordon Waller, Alex Bryant, Dalar Nazarian, Perry Ellis, Jen Breidenrich, Brian Doyle, Adrienne Muth, David Scripka, Matt Priddy, Aaron Tallman, Paul Kern, Rene Diaz, and Ben DeGlee.

For all of the continual support they have shown me, I'd be remiss not to thank my family. I'm blessed to have more supportive parents than any one person has a right to, but I'd especially like to thank my Mom, for always pushing me to grow outside my comfort zone and for teaching me that if you're going to do something, you might as well give it 110%. I'm also particularly grateful to my brother Taylor, for always being a source of calm and strength for me, even all the way in Switzerland. Last, but certainly not least, I must thank my fabulous husband Sean. I'm not sure how many six-month-old marriages could stand the rigor and strain that comes with

one spouse attempting to finish their doctorate, but I'm glad ours has. You have been the absolute model of a supportive spouse and a loving husband through this entire process, and I'm convinced it will take me the rest our lives to deserve it. I can't wait.

TABLE OF CONTENTS

LIST OF TABLES

LIST OF FIGURES

SUMMARY

The Materials Genome Initiative was announced by the White House in June of 2011, and is a multi-agency initiative which calls the materials community to find ways to discover, develop, manufacture, and deploy advanced materials systems faster and more cost-efficiently. Currently, the amount of time it takes to discover and develop a new material system, optimize its properties, integrate it in to a system, certify that system, and develop the manufacturing capability so that it can be deployed in a commercial component takes at least 20 years. Since this trend holds regardless of the material system in question, the implication is that it is the process by which we as a community move through these seven steps, which causes the lengthy timeline. Historically, the discovery, development, and property optimization of a material system relies heavily on deep scientific knowledge, intuition and trial-and-error physical experimentation. Therefore much of the design and testing of materials in these early stages is currently performed through time-consuming and repetitive experimental and characterization feedback loops. Some of these feedback loops could be eliminated in the property optimization step with improved powerful and accurate computational modeling tools. However, while the ability of computational models to be used in this way is not new, models that have been developed in this space have consistently underperformed. Oftentimes, these models fail because they fail to accurately account for the various physical and chemical mechanisms that are driving the system, or because they fail to account for all of the variables which must be included. Here we propose a standard method of communication for these relationships in the form a process-structure-property-performance map, which leverages

the known knowledge database of the material system to clearly and visually communicate the relevant variables and their various relationships in a defined materials design space. Such a map is developed here for high-strength Al-Zn-Mg-Cu alloys, which offer a good example of a material system which could benefit from such a standard. This class of alloys, which are typically utilized in aircraft components, have been incorporated in commercial components for nearly 75 years, and due to its long history is a well characterized and well developed system that is highly suited to this kind of examination.

In Part I of this work, we develop this standard by first examining the known knowledge database in this system to deduce what the important process, microstructure, and mechanical property variables are that are of interest. Once these variables and the relationships between them are identified, they are organized into a PSPP map according to a proposed set of steps, and can act as a visual standard that can clearly communicate critical information about the mechanisms of the system. For example, if a model developed within this system does not include a variable or a mechanism depicted within the map, it can be used to communicate the ways in which the model will be constrained. Similarly, when experimental data is collected within this space the map can be used to clearly communicate which variables in the space were held constant, which variables were tracked and accurately measured, and if any variables were unaccounted for. This information can help to communicate what situations the data can be used in, and how the space that the experimental data can be used in is constrained.

In Part II of this work, we vary multiple parameters within the high-strength Al-Zn-Mg-Cu system defined in Part I, and attempted to track and measure as many of the variables within the space as possible using commonly available testing and

characterization methods. In tackling such a large project in the complicated materials system of high-strength wrought Al-Zn-Mg-Cu alloys, we are able to understand which current testing and characterization methods are well suited to tracking these variables when the number of test specimens becomes quite large and when variability among those specimens is involved. We are also able to identify opportunities for future work in this area, which could be focused on improving our ability to implement projects of the scope that is required here. In addition to evaluating the feasibility of the various measurement and characterization methods, the raw data and the analyzed results for this work are cataloged in an associated data repository and have been made available for use in future work in this and other areas.

PART I: DEVELOPMENT OF PROCESS-STRUCTURE-PROPERTIES-PERFORMANCE MAP FOR HIGH-STRENGTH AL-ZN-MG(-CU) ALLOYS

Introduction

The Materials Genome Initiative was announced by the White House in June of 2011, and is a multi-agency initiative which calls the materials community to find ways to discover, develop, manufacture, and deploy advanced materials systems faster and more cost-efficiently. Currently, the amount of time it takes to discover and develop a new material system, optimize its properties, integrate it in to a system, certify that system, and develop the manufacturing capability so that it can be deployed in a commercial component takes at least 20 years. Since this trend holds regardless of the material system in question, the implication is that it is the process by which we as a community move through these seven steps, which causes the lengthy timeline. Therefore the Materials Genome Initiative calls on the materials community to embrace open innovation and to change the way that we approach the process, specifically by enabling early steps in the process such as discovery and development of a material system and property optimization, or the modeling of the developed process-structure-property-performance linkages, to be done concurrently or in a more integrated way.

Historically, the discovery, development, and property optimization of a material system relies heavily on deep scientific knowledge, intuition and trial-and-error physical experimentation. Therefore much of the design and testing of materials in these early stages is currently performed through time-consuming and repetitive experimental and characterization feedback loops. Some of these feedback loops could be eliminated in the property optimization step with improved powerful and accurate computational modeling tools. However, while the ability of computational models to be used in this way is not new, models that have been developed in this space have consistently underperformed. Oftentimes, these models fail because they fail to

accurately account for the various physical and chemical mechanisms that are driving the system, or because they fail to account for all of the variables which must be included. This inaccuracy arises from the simple fact that two different sets of researchers are typically responsible for these steps. In the materials community, the discovery and development of a material system is typically done by researchers with a deep knowledge in the material system being examined, and their expertise within the system allows them to rely on their scientific intuition to design, develop, and deduce meaning from the physical experiments that are predominately used in this stage. However, researchers who build computational modeling tools for property optimization purposes often have a deep expertise in computational modeling and data sciences, and are often unfamiliar with the physical and chemical mechanisms that drive the material system they are attempting to model. In many situations, the reason that these efforts fail can largely be traced back to the fact that no standard method of communicating information about the important variables in the system or the physical and chemical mechanisms that drive the relationships between such variables exists.

Al-Zn-Mg-Cu alloys offer a good example of a material system which could benefit from such a standard. This class of alloys, which are typically utilized in aircraft components, have been incorporated in commercial components for nearly 75 years, and due to its long history is a well characterized and well developed system that is highly suited to this kind of examination. Additionally, alloys in this class remain highly industrially relevant, and are constantly being redeveloped and redesigned in order to be deployed in new and ever-changing component systems. Despite the need for expedient property optimization, response from the materials community in this system can often be frustratingly slow, and computational modeling tools have had

little success in predicting various relationships in this space due to the complex nature of the process-structure-property-performance relationships involved.

Since the ultimate goal is to model these process-structure-property-performance (PSPP) relationships in the material system, a standard method of communication should be able to track what the important variables or elements are that need to be included in each of these categories (i.e. Process, Structure, Property, and Performance), and also to communicate which of these elements are known to share a causality relationship and which are known to be independent of each other. Since material systems are being continuously improved and developed, it is also important that this standard be able to communicate what relationships in the material system have not been explored or are not adequately understood and be a living standard which can be continually updated and changed as new information becomes available.

Here we propose such a standard method of communication for these relationships in the form a process-structure-property-performance map, which leverages the known knowledge database of the material system to clearly and visually communicate the relevant variables and the various relationships in a defined materials design space. Such a map is developed here for high-strength Al-Zn-Mg-Cu alloys which are utilized in aircraft applications by first examining the known knowledge database in this system to deduce what the important process, microstructure, and mechanical property variables are that are of interest. Once these variables and the relationships between them are identified, they are organized into a PSPP map according to a proposed set of steps, and can act as a visual standard that can clearly communicate critical information about the mechanisms of the system.

CHAPTER 1

CASTING, SOLIDIFICATION, HOMOGENIZATION, AND FORMING

The casting, solidification, and general forming process for aluminum alloys has many steps that all influence a variety of different aspects in the microstructure through a series of complicated and unclear relationships. However, the overall process including the different steps, the variables involved, and their influence on different microstructure characteristics are all remarkably similar regardless of the specific composition or application, especially within the realm of heat-treatable wrought aluminum products. This chapter covers the first half of these formation processing steps, including the casting and solidification of the initial ingot, the homogenization of that ingot, and the plastic deformation of the ingot into a commercial stock part. Since primary casting research is typically no longer priority of university research, at least in the USA, academic research in aluminum alloys development often relies on industrial aluminum suppliers to obtain bulk alloys if sufficient size and volume. Therefore, steps related to the casting and forming of the alloys prior to their heat treatment are usually conducted by an industrial aluminum supplier, and are rarely controlled in academic work. Since the processing history of the alloy through these first initial steps is not reported, it is important to understand what aspects of the final microstructure these processing parameters can influence.

1.1 Composition Limits

The American National Standards Institute (ANSI) maintains the alloy and temper designation system for aluminum and its various alloys [1]. Wrought aluminum alloys have a four-digit numeric designation system. The first digit identifies the main alloying element of the material, where a 7xxx series material is designated as a Al-Zn-Mg alloy. The third and fourth digits together do not have any physical basis in the composition of the alloy like they do in pure aluminum (1xxx series) or in low carbon steels. Rather they serve to differentiate different alloy compositions. The second digit indicates a modification to a particular alloy composition, where modifications digits are assigned sequentially. For example, 7150 is the first modification of the alloy 7050. Explicit rules exists and are maintained by the Aluminum Association to differentiate between what constitutes a modification to an existing alloy composition, and what counts as a new alloy [1]. The composition limits for various alloys discussed in this work are included in Table 1.1[1, 2].

Table 1.1: ANSI chemical composition limits of various Al-Zn-Mg-Cu alloys, in weight percent.

Alloy	Zn	Mg	Cu	Cr	Mn	Zr	Ti	Fe	Si	Al
7050	5.7-6.7	1.9-2.6	2.0-2.6	0.04	0.10	0.08-0.15	0.06	0.15	0.12	rem
7075	5.1-6.1	2.1-2.9	1.2-2.0	0.18-0.28	0.30	0.25-Ti	0.20	0.50	0.40	rem
7150	5.9-6.9	2.0-2.7	1.9-2.5	0.04	0.10	0.08-0.15	0.06	0.15	0.12	rem
7055	7.6-8.4	1.8-2.3	2.0-2.6	0.04	0.05	0.08-0.25	0.06	0.15	0.10	rem
7175	5.1-6.1	2.1-2.9	1.2-2.0	0.18-0.28	0.10	–	0.10	0.20	0.15	rem
7475	5.2-6.2	1.9-2.6	1.2-1.9	0.18-0.25	0.06	–	0.06	0.12	0.10	rem
7079	3.8-4.8	2.9-3.7	0.40-0.80	0.10-0.25	0.10-0.30	–	0.10	0.40	0.30	rem
7049	7.2-8.2	2.0-2.9	1.2-1.9	0.10-0.22	0.20	–	0.10	0.35	0.25	rem
7449	7.5-8.7	1.8-2.7	1.4-2.1	–	0.20	0.25-Ti	0.25-Zr	0.15	0.12	rem

1.2 Casting and Solidification

1.2.1 The Casting Process

Most commercial 7xxx-series aluminum alloys are produced by melting and mixing molten material together and then freezing the material into a solid ingot (sometimes called a billet) through a direct chill or semi-continuous casting method [1, 3, 4]. Although other casting methods such as simple gravity casting can be used, they are often plagued by quality control issues[4]. Direct chill casting is usually carried out in the conventional two-stage vertical set up that was originally patented by Alcoa in 1942, shown in Figure 1.1 [1, 3]. In the first stage, molten metal is solidified in the mold, which is water cooled, until it forms a shell. In the second stage, the shell is lowered at a constant rate and continuously spray-cooled with water [3, 4].

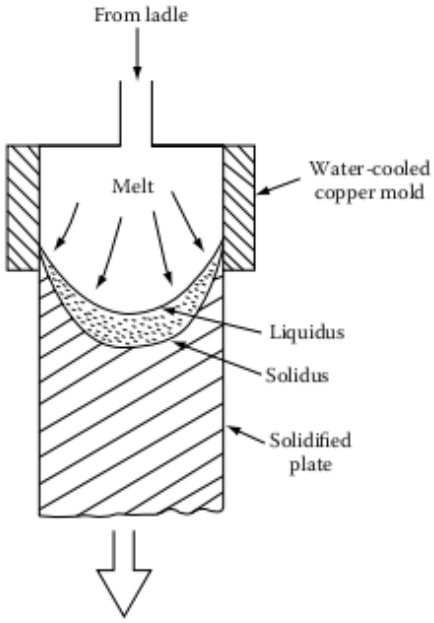

Figure 1.1: A schematic of the Direct Chill casting system.

As a result of this dynamic, rather than static, solidification process, the ingot microstructure differs from those that result from a more traditional gravity casting system. Traditional gravity cast ingots will generally have three distinct regions,

arranged as shown in Figure 1.2[3]. In continuous casting, this structure is slightly altered based on the elongated isotherms that result from the dynamic nature of the process. Figure 1.3[3] shows both the elongated nature of these isotherms and the resulting effect on the columnar and equiaxed dendritic regions.

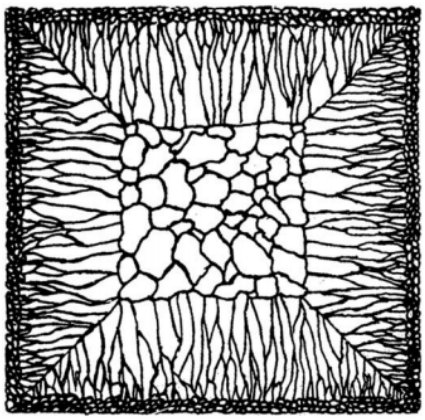

Figure 1.2: Schematic of an-cast microstructure resulting from a traditional gravity casting system showing the three different regions.

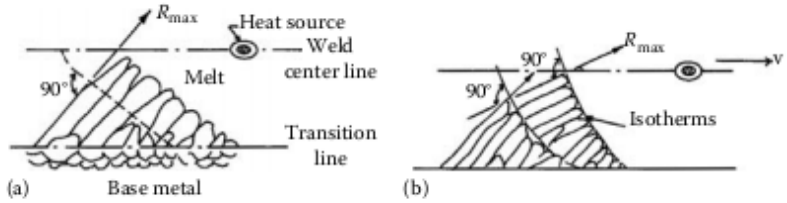

(a) Elongated isotherms

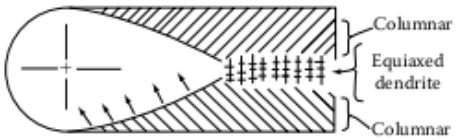

(b) Resulting grain structure

Figure 1.3: Schematics showing the elongated isotherms that result in the material during DC casting and the resulting effect on the various grain regions

Because the microstructure of the as-cast material is dendritic in nature, the resulting grain structure will be highly cored, with a primary phase that is non-uniform across

the grains and a divorced eutectic of intermetallic phases in between them, shown in Figure 1.4. [3, 4, 5].

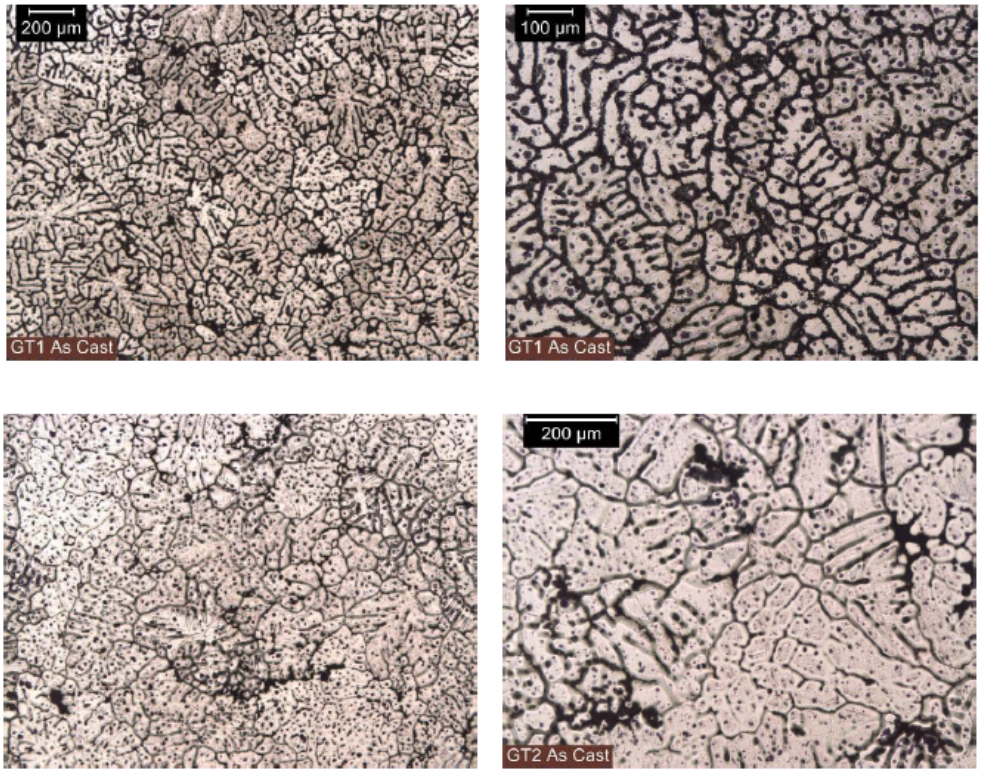

Figure 1.4: Images showing the as-cast microstructure of various Al-Zn-Mg-Cu alloys.

The low strength in these intermetallic regions compared to the primary grains can cause fracturing under the stresses generated in the ingot during the freezing and subsequent cooling processes [5]. Such fracturing is referred to as hot cracking or solidification-cracking when it occurs during solidification and cold-cracking when it occurs in non-stress relieved ingots following the solidification process [4, 5]. An example of cold cracking in an ingot is shown in Figure 1.5 [5]. Because cold cracking is a major issue in non-stressed relieved aluminum, ingots are often heated to a sub-homogenization temperature for several hours before being air cooled. This process helps to relieve stress from the ingot prior to homogenization [4].

Figure 1.5: An example of cold cracking in a DC ingot 7178 alloy, approximately 15"x60" in size.

1.2.2 Methods to Control or Alter the As-Cast Microstructure

Similar to traditional gravity casting systems, the growth of equiaxed structures in the center of the ingot can be promoted and controlled with a source of heterogeneous nucleation to reduce the size of the columnar region. In most commercial 7xxx series alloys, this is accomplished through the addition of an Al-Ti-B grain refiner, which forms soluble Al_3Ti and insoluble TiB_2 particles that can be dispersed throughout the alloy. By promoting a more fine and equiaxed grain structure, these refiners both reduce segregation and decrease the susceptibility of the ingot to hot cracking. They can also improve the response of the ingot to subsequent hot or cold forging steps and surface finishing techniques [4]. However, care must be taken to routinely clean all involved casting equipment, since even a small excess of boron can lead to the formation of large agglomerated particles which have detrimental effects on the machinability, fracture toughness, and appearance of the resulting alloy [1, 5]. An example of an inclusion stringer of borides resulting from an excess amount of grain refiner is shown in Figure 1.6 [5]. In addition to introducing quality control issues,

this can also present a challenge in the field of recycling of aluminum alloys.

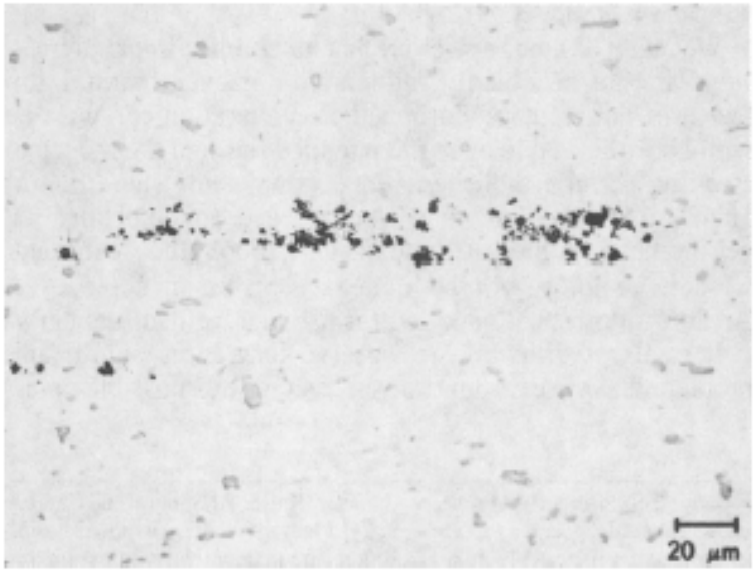

Figure 1.6: An example of a boride stringer containing Al_4.

Elements such as Cr, Zr, and to a lesser extent Mn are often added to aluminum alloys to facilitate the precipitation of fine well dispersed particles during the homogenization step. These dispersoid particles help to pin grain boundaries and inhibit recrystallization during the solution heat treatment step, assist grain refinement during rolling, and act as nucleation sites for equilibrium η (Mg_2Zn) particles [1, 4, 6]. While some aluminum alloys such as 7049, 7075, and their improvements use Cr as a grain refiner, it has been observed that these materials become inherently susceptible to the formation of large $CrAl_7$ particles. These constituents then go undissolved in the homogenization process and during subsequent plastic deformation processes are broken up in to a stringer defect. The presence of such defects decreases the mechanical properties of the alloy by increasing recrystallization through particle stimulated nucleation and acting as sites for fatigue crack formation. An example of a coarse primary crystal and the resulting stringer is shown in Figure 1.7 [1, 5]. The continued occurrence of this phenomenon, even when Cr levels are relatively low, can be attributed to the "chromium equivalence", which claims that primary Cr particles

form even at relatively low concentrations due to the presence of Ti, Mn, Fe, and V substituting in for Cr atoms in the phase structure [4, 5].

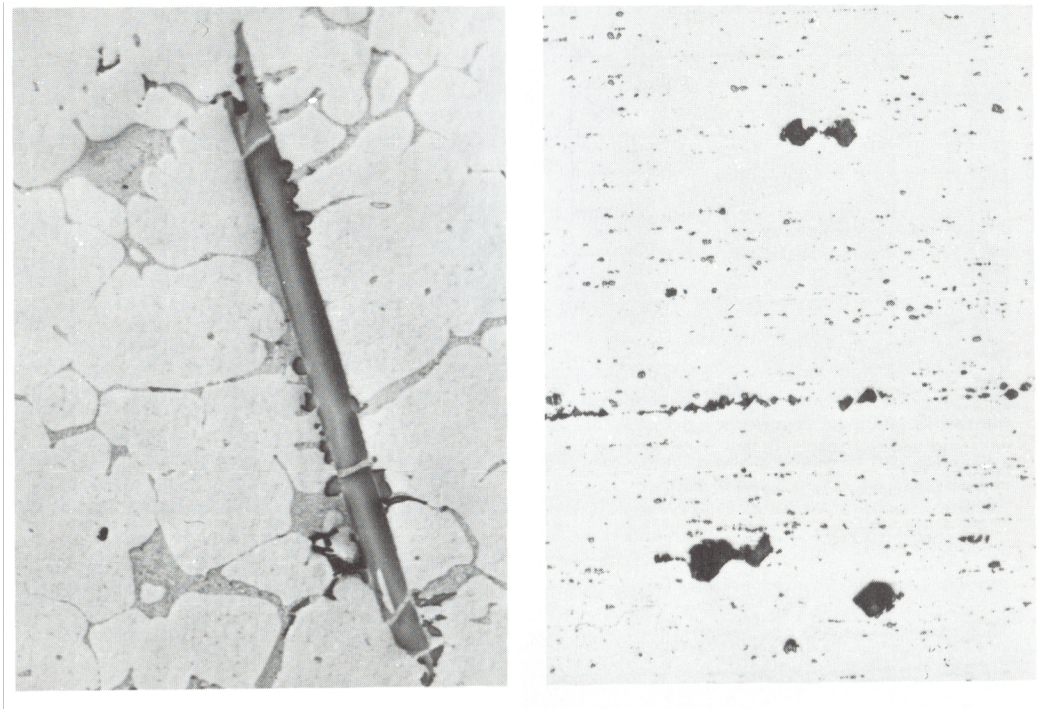

Figure 1.7: An example of a coarse Cr primary crystal on the left, and the stringer which results after rolling on the right.

Other aluminum alloys, including 7050, use Zr as a dispersoid forming element instead of Cr to form small particles of Al_3Zr [1]. However, Zr can also form primary particles and is subject to a similar "zirconium equivalence" in 7050-type materials. This equation is given by [5]

$$\mathrm{Zr} + 0.2\mathrm{Ti} + 0.02\mathrm{V} \geq 0.13 \tag{1.1}$$

Changing the amount of alloying elements in the ingot can also significantly influence aspects of the casting and solidification process. By changing the alloy content, the freezing range of the alloy, or the distance between the liquidus and solidus lines, is altered. As a result, the volume fraction of non-equilibrium eutectic present in the as-cast microstructure and the alloys susceptibility to cracking will change [1, 4]. Indeed, Cr and Cu have been shown to increase the susceptibility of hot cracking,

while Zr and Mn have been shown to decrease it [4].

As with all solidification processes, but particularly in off-eutectic alloys which are prone to dendritic growth, the cooling rate (i.e. the rate of under-cooling) is critically important in controlling (1) the size of the equiaxed dendrites, (2) the distribution of the constituent particles, and (3) the amount of grain refining dispersoid elements (Zr, Cr, and Mn) that remain in super saturated solid solution [1, 4]. In general, higher cooling rates will produce finer and more equiaxed microstructures. However, the cooling rate can also affect the recrystallization resistance of the alloy by altering the size of the constituent particles and their ability to induce particle stimulated nucleation (PSN) [1, 4, 6]. At low cooling rates, constituent particle sizes are large but their number density is small. As cooling rates begin to increase this produces smaller and more distributed particles. Eventually, at high cooling rates these particles are too small to instigate PSN, and the recrystallization resistance increases [4].

1.3 Homogenization

As mentioned in the previous section, the resulting as cast microstructure is largely made up of primarily dendritic regions that exhibit a significant amount of solute segregation, or coring, due to non-equilibrium cooling conditions [1, 4]. In between these grains are inter-dendritic regions containing a divorced eutectic of intermetallic phases, typically reported as Al_7Cu_2Fe, Al_2CuMg, and Mg_2Si [4, 5, 6, 7]. The primary goal of homogenization is to heat the alloy to an elevated temperature for an extended period of time in an attempt to increase diffusion and allow for the redistribution of the solutes in the system [1, 4]. As a result, the time and temperature of homogenization is often chosen to dissolve as many of the coarse constitutive phases in the inter-dendritic region as possible without causing melting [4, 6, 8].

This microsegregation across the dendritic region occurs because of the difference between the solid and liquid solubility levels of the different alloying elements at a given temperature, which are usually reported as a ratio, k [1, 3].

$$k = \frac{C_s}{C_l} \tag{1.2}$$

When an alloy of composition C_0 (which is all liquid such that $C_l = C_0$) is cooled to a temperature T below the liquidus line, it forms a solid of composition C_s. The tip of the dendrite, and therefore the center of the dendritic structure, will have a composition of C_s, or kC_l. As solidification happens further behind the tip of the dendrite at lower temperatures, the liquid that is solidifying is increasingly solute rich (assuming that $k < 1$) since $kC_l < C_0$. This process repeats and as solute is continually rejected in to the liquid it gathers in the inter-dendritic regions, finally forming a divorced eutectic of intermetallic particles. The α-Al grains, which are increasingly solute rich towards the outer edge of the dendrite, fill in the space around these coarse constituent particles by the coarsening of the secondary dendrite arms. The solute distribution, or the coring, in these grains can be described with reasonable accuracy by the Scheil equation [1, 3].

$$C_s = C_0 k(1 - f_s)^{k-1} \tag{1.3}$$

Where C_0 is the concentration of a solute in the alloy, k is the distribution coefficient, and C_s is the composition at weight fraction solid f_s.

Most alloying elements, including Cu, Mg, and Zn, have a relatively low solid solubility in Al and a $k < 1$. As a result, these solutes will segregate towards the inter-dendritic region. However, Zr segregates in the opposite direction and tends to be clustered towards the center of the alpha primary grain and depleted at the boundary. This is a result of the peritectic reaction ($k > 1$) in the Al-Zr phase diagram [6, 8]. Often the segregation of Cu, Mg, and Zn towards the grain boundaries can be seen in the

as-cast microstructure in the form of highly concentrated η-phase particles in this region [4, 6]. These particles usually precipitate out during air-cooling following the stress-relieving process. The as-cast microstructure of a 7050 aluminum alloy after stress relieving is shown in Figure 1.8, showing the presence of such particles [6].

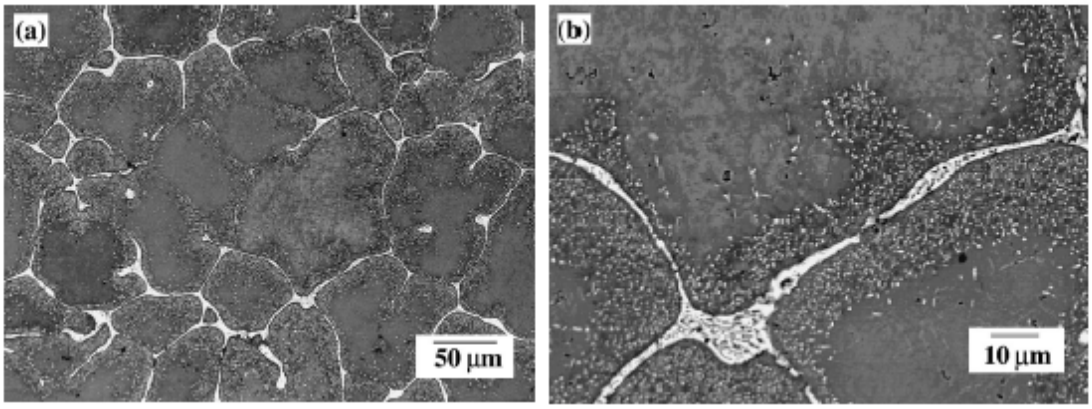

Figure 1.8: (a)Low and (b) high magnification images of the as-cast microstructure showing the segregation of Cu, Zn, and Mg towards the grain boundaries.

However, a secondary goal of homogenization in 7050 is to facilitate the precipitation and growth of small Al_3Zr dispersoids, usually between 20-50nm in diameter, intended to pin grain boundaries and reduce recrystallization during subsequent processing steps [1, 4, 5, 6, 8]. Because these dispersoids are, along with high-angle grain boundaries, the primary precipitation sites for heterogeneous nucleation, controlling their size, number density, and distribution is of critical importance [4, 6, 8]. The characteristics of these particles will directly affect the quench sensitivity and precipitation kinetics of the alloy in the remaining processing steps. Unfortunately, due to solute segregation during casting, dispersoid-forming elements such as Cr and Zr are also inhomogeneously distributed. The clustering of the dispersoid particles that result is considered highly non-optimal, so homogenization procedures are often designed specifically to obtain well distributed dispersoids.

In regions of the grain where Zr concentration is very high, homogeneous nucleation of small Al_3Zr particles is relatively easy, leading to a large number density and small average particle size. Conversely, there exists near the dendritic boundary a dispersoid free zone (DFZ), where the concentration of Zr is too small to form particles (less than the 0.08wt% necessary at 500°C). In between these two regions, a few dispersoids are present in larger, elongated clusters consisting of 10 or more small spherical particles. Here, the same η particles that are present inside the edge of the grain, act as heterogeneous nucleation sites for these dispersoids. After homogenization, these particles are dissolved, leaving only the dispersoids behind [6]. These dispersoids limit the ability of the material to recrystallize by existing in sufficient numbers to induce whats known as the Zener drag effect. The pressure exerted by a dispersion of randomly spaced, spherical particles is proportional to the volume fraction of those particles over their radius [4, 8]. Since the volume fraction of particles is typically fixed, the pressure exerted by the dispersoids can be best increased through the controlled precipitation of small, well dispersed, coherent particles and a minimization of the dispersoid free zone (DPZ) near inter-dendritic regions [4, 6, 8].

Optimization of the homogenization treatment has been thoroughly explored, and homogenization treatments to achieve maximum properties including non-conventional multi-step treatments are typically highly proprietary [4]. In general, 7050 and other Al-Zn-Mg-Cu alloys are restricted to a limited homogenization temperature range, typically between about 470-485°C due to the presence of low melting temperature eutectics. However, it has been shown that lowering the homogenization temperature only has a limited effect on decreasing the average dispersoids size and that it has no effect at all on decreasing the size of the DPZ. Even using ramp heating as opposed to isothermal treatments only gives moderately improved results. Rather, the most effective changes in achieving optimal dispersoid size, number density, and DPZ width

comes with increasing the amount of Zr within the allowable range [6].

1.4 Plastic Deformation

High-strength aluminum alloys can be plastically deformed into stock material by a variety of processes. By far the two most important deformation processes for commercial applications are hot rolling and extrusion [4, 7, 8]. In general, these plastic deformation processes have a great deal of influence on the final microstructure of the material, especially in determining the final grain size, the amount of high- or low-angle grain boundaries, the likelihood of the material to recrystallize or recover during solution heat treatment, and the general uniformity of the microstructure across the stock piece [1, 4, 7, 8]. The variable parameters at play during each of these processes and their result on the final microstructure of the alloy are briefly reviewed. Forging in 7050 aluminum is not covered in this work as the relative forgeability of 7xxx series alloys is quite low [1]. A more in-depth review of rolling, extrusion, and forging in high-strength and other aluminum alloys can be found elsewhere [1, 4, 9, 10, 11].

1.4.1 Rolling

Rolling is the primary method for forming commercial plates and sheets of 7050. Generally, a rolled product is considered plate if it is at least 0.250 (6.3mm) and can be regularly ordered in thicknesses of up to 6.00 (152.4mm). Sheet is considered to be rolled product with a thickness between 0.006 (0.15mm) and 0.187 (4.75mm), with anything thinner usually being referred to as a 'foil' [4, 12, 13]. Roll forming consists of passing the ingot in between one or more pairs of rollers to incrementally decrease the thickness of the ingot until the desired thickness is obtained. The difference between the initial and final thickness of the rolling process is typically referred to as the 'draft' [4].

Roll forming is typically done at an elevated temperature, allowing for the breakdown

of the as-cast microstructure as deformation is applied and resulting in an elongated microstructure in the rolling direction [4, 13]. Although cold rolling can be used to obtain a better surface finish, hot rolling is typically the preferred method [4]. While the temperature of rolling, the rolling reduction, and the deformation rate have all been known to affect the degree of recrystallization experienced by the alloy during solution heat treatment, 7050 does not undergo dynamic recrystallization during this process [7, 8]. Rather, the material dynamically recovers during hot rolling, forming equiaxed sub-grain cells throughout the microstructure. The resulting stored energy is distributed inhomogeneously throughout the material, often concentrated around constituent particles that are still maintained in the microstructure [7]. This increase in the stored energy density means that these areas will have a greater driving force for recrystallization, which is the basis behind particle stimulated nucleation (PSN) in these materials. As a result, an increase in the hot rolling temperature, an increase in the amount of rolling reduction, and an increase in the deformation rate will all cause an increase in the amount of stored energy in the material and therefore increase the amount of recrystallization in the final microstructure. It is also important to note that rolling can produce extremely non-uniform microstructures throughout the thickness of the plate. Since the majority of deformation and strain energy is being stored at the edges of the plate where the ingot is in contact with the roller, these areas often contain significantly higher amounts of recrystallization [1, 4]. These changing microstructure features throughout the thickness of the alloy is important to consider in the application of the material. For example, 7050 has superior properties in thicknesses over 2", and as a result plates of it are often used in fuselage frames and bulkheads, where components can require section thicknesses between 2"- 6" [12].

1.4.2 Extrusion

Extrusion is also a popular form of plastic deformation in 7xxx series alloys, though it is less commonly applied to 7050 commercially than to other popular alloys in this series, such as 7075 [1, 4, 12]. In general, extrusion offers many advantages in manufacturing since it can be accomplished relatively quickly and can create a large variety of cross sections and shapes. It is often applied to aluminum alloys in part because, compared to many other alloying systems, aluminum alloys are quite malleable. However, 7xxx series aluminum in particular becomes more difficult to extrude with increasing amounts of Zn, Mg, and Cu, and exhibits flow stresses that are significantly higher than those for mild steel [1]. Regardless, 7050 is still available in extruded form commercially, and so those processing variables that affect the final microstructure during the extrusion process should be briefly considered [12].

Extrusion usually occurs in one of two forms, either through direct or indirect extrusion. While direct extrusion is more popular when considering all aluminum alloys, indirect extrusion is usually preferred in 7xxx series alloys due to the lack of friction forces between the billet and the container, which reduces the likelihood of recrystallization [4, 13]. The main variables in the extrusion process include the extrusion ratio, the ram speed, and the extrusion temperature [4]. However the real driving variable in this process is the strain rate in the material, which is required to model the extrusion process [4]. The real difficulty in modeling the extrusion process as a function of the physical deformation mechanisms, arise in part from the extreme temperature gradients and the non-uniform strain rate that occur in the material. The Zener-Hollomon parameter attempts to relate the temperature-compensated strain rate to the flow stress of the material, thereby allowing for more effective modeling. Various phenomenological equations relating this parameter to the flow stress have been proposed for different temperature and strain regions in the seventy-two years

since this parameter was first introduced [4]. While regression analysis to determine the coefficients for these various phenomenological laws is still the primary method of modeling the relationship between the temperature, strain rate, and flow stress, the real value of the Zener-Hollomon parameter continues to lie with its ability to be directly correlated to final properties of the alloy in terms of strength, fatigue, and even corrosion resistance [4].

1.5 Summary

This chapter discussed the first several steps in the casting of a commercial aluminum alloy product, which when processed using the most up-to-date industrial processes, can be highly complicated and require a level of expertise and equipment not always available to academic studies. Additionally, many of these steps are often proprietary in nature. Therefore, although the effect of these steps may be well understood industrially, they are more difficult to account for academically. This mainly results from the common practice in academic studies of ordering a commercially available material and re-treating it, and the fact that the processing parameters and exact steps that were executed are not reported with the final material product that is received. However, it is clear from the work examined above that all of these processing steps have a significant impact on the final microstructure. One method of negating this effect within a given study would be to ensure that all of the material used was processed in the same way, presumably by ordering the same commercial material designation from a single supplier. While this does help to ensure that the processing parameters chosen for the materials within a particular study are consistent, this does not allow for the meaningful comparison of multiple studies across the literature unless this processing history can be reported, or otherwise accounted for.

1.6 References

[1] J. R. Davis, editor. *Aluminum and Aluminum Alloys*. ASM International, 1993.

[2] The Aluminum Association. International alloy designation and chemical composition limits for wrought aluminum and wrought aluminum alloys, January 2015.

[3] David A. Porter, Kenneth E. Easterling, and Mohamed Y. Sherif. *Phase Transformation in Metals and Alloys*. CRC Press, 3rd edition edition, 2009.

[4] Justin Lamb. *Decomposition and its effects on Mechanical Properties in Al-Zn-Mg-Cu Alloys*. PhD thesis, Georgia Instiute of Technology, 2015.

[5] J. B. Hess. Physical metallurgy of recycling wrought aluminum alloys. *Metallurgical Transactions A*, 14A:323–327, 1983.

[6] J. D. Robson and P. B. Prangnell. Dispersiod precipitation and process modelling in zirconium containing commercial aluminum alloys. *Acta Materialia*, 49:599–613, 2001.

[7] N. U. Deshpande, A. M. Gokhale, D. K. Denzer, and John Liu. Relationship between fracture toughness, fracture path, and microstructure of 7050 aluminum alloy: Part I. quantitative characterization. *Metallurgical and Materials Transactions A: Physical Metallurgy and Materials Science*, 29A:1191–1201, 1998.

[8] X. Zhang, W. Liu, S. Liu, and M. Zhou. Effect of proprocess parameters on quench sensitivity of an AA7050 sheet. *Materials Science & Engineering, A: Structural Materials: Properties, Microstructure and Processing*, 528:795–802, 2011.

[9] G. E. Dieter, H. A. Kuhn, and S. L. Semiatin. *Handbook of Workability and Process Design*. ASM International, 2003.

[10] H. J. McQueen, S. Spigarelli, M. E. Kassner, and E. Evangelista. *Hot Deformation and Processing of Aluminum Alloys*. CRC Press, 2011.

[11] T. Sheppard. *Extrusion of Aluminum Alloys*. Kluwer Academic Publishers Group, 199.

[12] Alcoa. Alloy 7050 plate and sheet, 2016.

[13] J. Gilbert Kaufman. *Introduction to Aluminum Alloys and Tempers*. ASM International, 2000.

CHAPTER 2

SOLUTION HEAT TREATMENT, QUENCHING, AND AGING

Wrought aluminum alloy products that have been formed and then annealed by the processes discussed in Chapter 1 are designated with an -O temper. While alloys can be purchased in an -O temper, it is not common. These materials have been annealed in such a way as to produce the lowest possible strength of the alloy. To increase the strength and obtain other desired mechanical properties, the material is subjected to a solution heat treatment at an elevated temperature similar to the homogenization treatment discussed in the previous chapter. After quenching from this elevated temperature the material carries a -W temper, which is highly unstable in Al-Zn-Mg-Cu alloys. The final processing step applied to wrought products is the aging treatment, which plays a vital role in determining the final microstructure of the material. This chapter discusses each of these steps in detail to understand how they effect the microstructure, and as an end result, the mechanical properties.

2.1 Solution Heat Treatment

The primary function of the solution heat treatment (SHT) process involves heating the alloy to a temperature near the solvus line to help dissolve coarse constituent particles and to increase the equilibrium concentration of both solute and vacancies [1]. This process results in a supersaturated solid solution, which will drive the precipitation kinetics involved in the aging process. Although higher temperatures would mean a higher amount of constituents dissolved and a higher degree of supersaturation, caution must be taken due to the presence of low melting temperature phases. Therefore

it is common to keep the temperature of the SHT below the eutectic temperature, at least until these phases are dissolved. Two-step solution treatments, with a primary step at a temperature below T_E and a second step such that $T_E < T_{SHT} < T_{solvus}$, are common in industrial processing [2, 3]. Due to an increase in the number of excess vacancies and a higher degree of supersaturation, it is expected that increasing the solution heat treatment temperature would result in an increase in some of the mechanical properties of the alloy after aging. While this is true for initial increases, as the SHT temperature continues to increase, the properties of the alloy begin to fall off. This effect has been well documented and can be seen in Figure 2.1 [4].

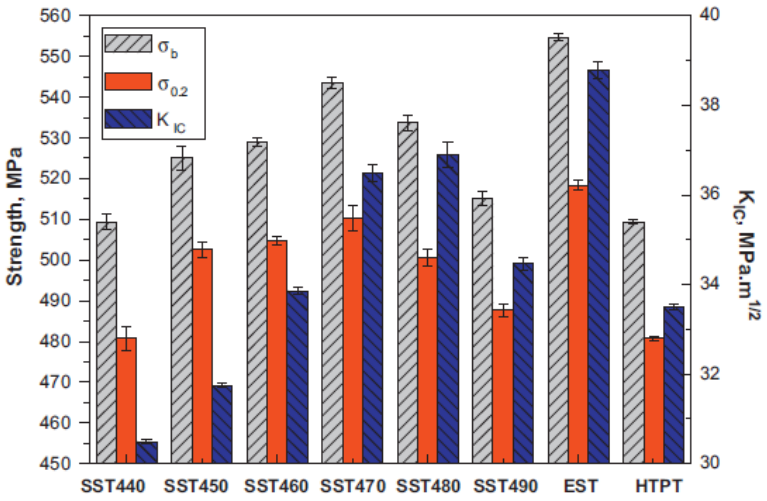

Figure 2.1: Tensile strength and fracture toughness of aged 7050 solution heat treated at different temperatures and various multi-step treatments[4].

To understand this behavior, it is necessary to examine the affect that the increasing SHT temperature has on some aspects of the microstructure. As the SHT temperature approaches first 480 and then 490 °C, it is observed that the volume fraction of constituent phase particles does decrease as expected. However, increasing the SHT temperature also causes an increase in the extent of recrystallization, which causes

the strength and fracture toughness of the material to fall off again at high temperatures [4].

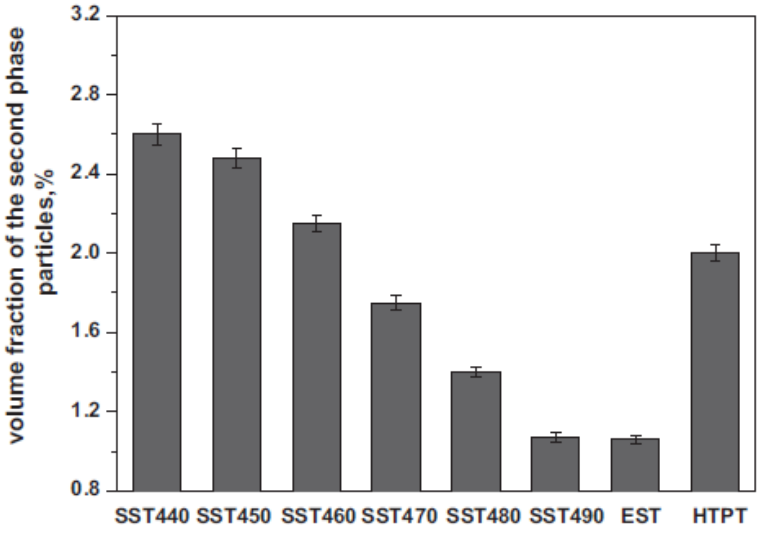

Figure 2.2: Volume fraction of second phase constituent particles in 7050 solution treated at different conditions[4].

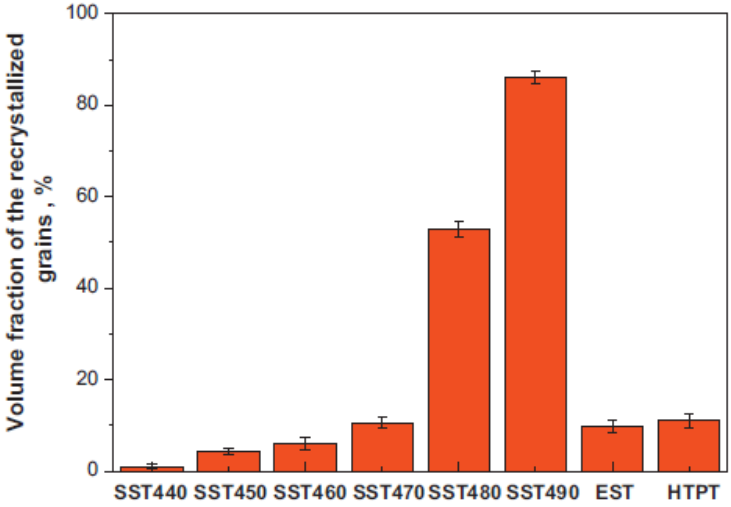

Figure 2.3: Volume fraction of recrystallized grains in 7050 solution treated at different conditions[4].

As discussed in previous sections, increasing the amount of stored energy in the microstructure through rolling and other plastic deformation processes and facilitating the nucleation of dispersoids to increase the Zener drag are just a few methods of

altering the amount of energy required to nucleate and perpetuate recrystallization in the alloy. Therefore, although recrystallization is usually observed during the SHT process, the entire processing history of the alloy plays a critical role in the likelihood that it will be observed.

2.2 Quenching

The rate of cooling, or the quench rate, of the alloy from the solution heat treatment temperature to room temperature can greatly impact the final microstructure and mechanical properties of the system. Typically in 7xxx series aluminum, a sufficiently fast cooling rate is required to (1) "quench in" excess vacancies and (2) prevent the nucleation of undesirable precipitates from the supersaturated solid solution [2].

As discussed in the previous section, part of the role of the SHT is to increase the equilibrium vacancy concentration of the system. When these vacancies are "quenched in" with a sufficiently fast cooling rate they enable the nucleation and growth of strengthening precipitates in two ways. The first is by providing sites for the heterogeneous nucleation of strengthening particles, either Guinier-Preston (GP) Zones or the metastable $\eta\prime$ phase. Given time, vacancies in excess of the equilibrium concentration will attempt to anneal out of the material and will either be driven towards grain boundaries or will segregate together to form vacancy rich clusters (VRCs). With enough time and driving force, these VRCs will collapse into dislocation loops. Either VRCs or dislocation loops can serve as heterogeneous nucleation sites for this precipitation to occur [1, 5, 6]. The second method is by increasing the ability of solute atoms to diffuse through the matrix, facilitating the formation of solute rich clusters which are a precursor for the formation of GP Zones. Since the presence of individual or even small vacancy clusters cannot be resolved individually, even by TEM analysis, a deduction of the role that excess vacancies play in the aging process

must be indirect and is the subject of much debate [5, 6, 7, 8, 9, 10, 11]. Therefore, it is to be expected that decreasing the cooling rate will decrease the precipitation kinetics that drive the aging process by allowing more time for vacancies to anneal themselves out of the material during the quench [1, 5].

The addition of different alloying elements can also affect the role of vacancies in the early aging process, especially if the addition has a high solute-vacancy binding energy [5, 12]. Although solute-vacancy binding energies can be notoriously difficult to measure experimentally, a robust first-principles study was conducted in the last decade by Wolverton to calculate many of these binding energies in aluminum. In this work, Wolverton observed that the solute-vacancy binding energy for Cu calculated was rather small, and in the case of Mg was actually negative [12]. This contradicts the long held assumption that Mg, and Cu to a lesser extent, possesses a strong solute-vacancy binding energy and that this binding is responsible for the formation of GP Zones from Mg-rich clusters [9, 10, 13, 14, 15]. The results reported by Wolverton are however, consistent with other studies that have shown the binding energy for Mg to be small in aluminum.

In general, Wolverton notes a strong correlation between the size of the solute and its vacancy binding energy, shown in Figure 2.4. While this is to be expected, since large atoms will cause a strain in the matrix which the presence of a vacancy can help to relieve, Mg, Sc, and Zr are notable for being large solutes that lack a correspondingly high vacancy-binding energy. Similarly, Cu, Zn, and Ag are all shown to have a size smaller than that of Al, but still possess slightly positive vacancy binding energies. This may help to explain the effects of Ag and Cu on the precipitation process.

It has been shown by multiple authors that the addition of very small amount of Ag help to decrease the width of the precipitate free zone (PFZ) and increase the

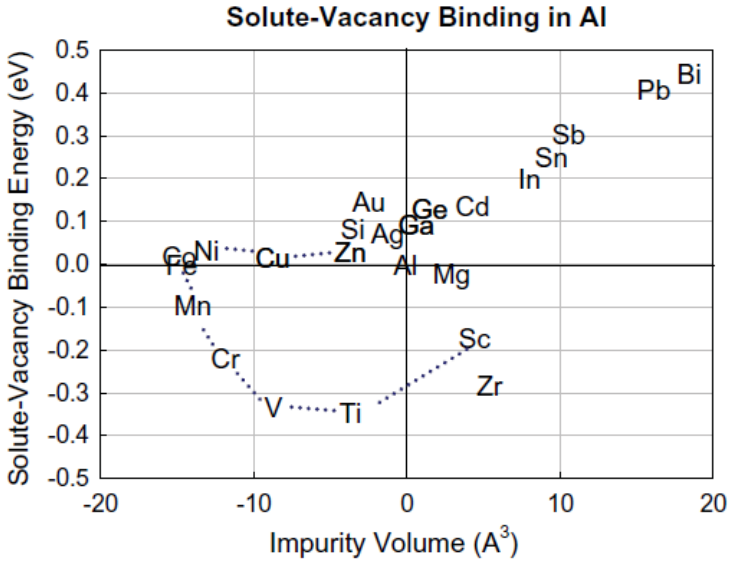

Figure 2.4: The calculated solute-vacancy binding energy versus the impurity volume in Al of various elements[12].

dispersion of fine $\eta\prime$ particles in the matrix [8, 14, 16]. Because of the relatively high binding energy of Ag, excess vacancies are pinned in the matrix, and thus less able to anneal out near grain boundaries. The presence of these vacancies near the grain boundaries when they would not otherwise be present can account for these very small PFZ widths. Additionally an increase in the vacancy concentration can increase the diffusivity of solute atoms, which is critical in the formation of GP Zones [3, 5]. This was confirmed by Maloney et al.[8], who observed that the presence of Ag caused the preferential co-clustering of Zn and Ag at early aging times. These Zn-Ag clusters were seen to occur earlier than Zn-Mg clusters are observed in the non-Ag alloy system, and initiate Zn-Mg-Ag clusters that are the precursor to $\eta\prime$ phase [8]. This confirmed earlier work by Ringer and Hono, who postulated the same effect [14].

The presence of Cu is also believed to increase the clustering ability of solutes at low temperatures and early aging times. As early as forty years ago, Sanders and Starke observed that the presence of Cu altered the aging process by decreasing the

barrier for homogeneous nucleation of GP Zones in Al-Zn-Mg systems [17]. This effect has since been confirmed by others [10, 14, 18]. In 3D atom probe microscopy studies of solute clusters during early aging, Sha and Cerezo showed that the concentration of Cu in small solute clusters was quite high and decreased as solute clusters became larger and more Zn-rich [10]. The authors concluded that Cu increased the nucleation kinetics of early aging precipitates, but that it had little effect on the growth kinetics. This observation was later confirmed by Gupta et al. [18]. It may be of interest to note that this effect is observed for both Cu and Ag, possibly either because or in spite of, the low diffusivity of these elements in aluminum as compared to Zn and Mg [3]. Thus the exact role of quenched-in vacancies in the aging process continues to be debated.

The other role of rapid quenching is to prevent the nucleation of secondary phases. At elevated temperatures such as those seen during the SHT, the equilibrium concentration of solutes dissolved in the matrix is also increased. Similar to the need of a sufficiently fast cooling rate to quench in vacancies, it is also important to maintain this supersaturated solid solution and keep these solutes from precipitating the equilibrium η phase at heterogeneous nucleation sites such as grain boundaries or dispersoids [2, 19, 20, 21]. One method, therefore of decreasing the quench sensitivity is to decrease the degree of recrystallization and lower the mis-orientation angle of sub-grain boundaries [21]. Once again, it is noted that a large number of variables, including the composition of the alloy, the homogenization process, the plastic deformation and thickness of the piece, as well as the solution heat treatment all affect the quench sensitivity of 7xxx series alloys.

Compared to other alloys in the 7xxx series, 7050 aluminum is considered to be relatively quench insensitive, and thus it is commonly used in thick component parts

[19, 20, 21, 22]. However, while the cooling rate seen by the material during the quench has relatively little effect on the strength of the material, it has been shown to have a much larger effect on the fracture toughness and stress corrosion cracking susceptibility [19, 20]. Indeed while changing the quench rate may affect the yield strength of the material by as little as 10%, it can change the critical energy release rate, G_{IC}, by as much as a factor of 2 [20]. This is attributed to the high rate of nucleation of η precipitates on grain boundaries, which increases the amount of intergranular fracture seen by the material by facilitating the void coalescence stage, as discussed in Chapter 3 [19, 20].

2.3 Aging Heat Treatment

Precipitation hardening, or aging, was discovered by accident in an Al-Cu alloy in 1904 and led to the creation of duralumin, the first commercially important aluminum alloy. This discovery was followed by two reports published in 1919 by the then U.S. Bureau of Standards, which explored the possibility that other alloys could also show induced precipitation hardening through the use of elevated temperature treatments based on the examination of various phase diagrams. This discovery sparked a golden age in the field of physically metallurgy, which led not only to the discovery of hundreds of precipitation-hardened alloys, but also inspired the close exploration of hundreds of phase diagrams, confirmed the concept of solid solubility, pioneered a better understanding of meta-stability and phase transformations, and even spawned the introduction of dislocation theory [23]. It is therefore, no surprise that the precipitation kinetics involved in this process were, and continue to be, the subject of much interest and debate.

2.3.1 Precipitation Kinetics

It was originally reported that precipitation occurred in Al-Zn-Mg alloys as [6]

$$\alpha - SSSS \rightarrow GPZ_{spherical} \rightarrow \eta\prime \rightarrow \eta(MgZn_2) \tag{2.1}$$

Where the homogeneous nucleation of Guinier-Preston (GP) Zones was dependent on the quenched in vacancy concentration, similar to the Al-Cu system in which duralumin was based [6]. TEM studies had shown a hexagonal phase structure for both $\eta\prime$ and η, though it was noted that at higher aging temperatures this precipitation sequence yielded the cubic $T\prime$ and T ($Mg_{32}(Al,Zn)_{49}$) phases instead [6, 24]. More recent work has suggested that this precipitation phase is preferred when the Zn:Mg ratio is low [24, 25].

However even as early as fifty years ago, anomalies were reported that suggested that the precipitation process was not quite so simple. While the presence of spherical GP zones was observed at 135 °C, at 180 °C these zones were observed to be more angular or even plate-like, and to be either FCC with an ordered AuCuII structure or hexagonal [6]. Further complicating this understanding of a simple precipitation processes was the observation a decade later that GP zones formed in the ternary system at temperatures below 120 °C, even without the presence of excess vacancies [7]. At temperatures higher than 120 °C, the presence of excess vacancies induced the homogeneous nucleation of the $\eta\prime$ phase directly. When these vacancies were not present in the system due to step-quenching, the formation of any phase at these higher temperatures was stalled. This curious observation is detailed in the resistivity curves of both a step-quenched and water-quenched alloy, shown in Figure 2.5 [7].

Even though GP Zones can form either with or without the presence of quenched-in vacancies, the changing kinetics with vacancies and aging temperature suggest that the leading mechanism of cluster formation is still solute-vacancy migration [9]. This is supported by the fact that additions of Cu, which trap vacancies and remove their mobility and ability to assist Mg and Zn migration, slows down the precipitation kinetics at low temperature and mimics the response when no vacancies are present

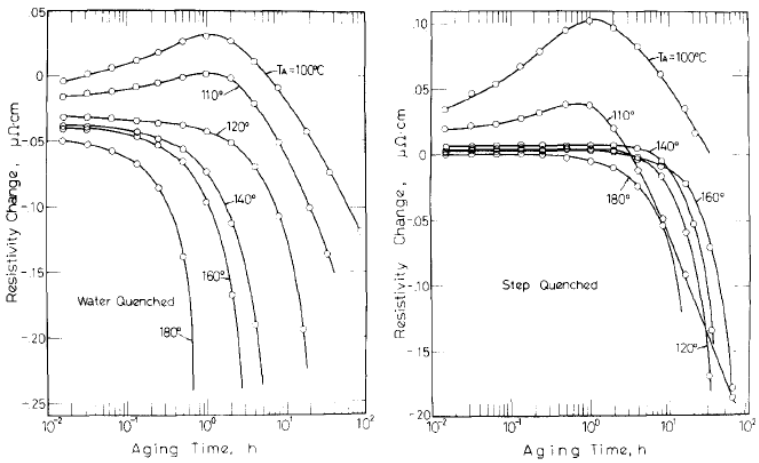

Figure 2.5: Resistivity-aging curves of water-quenched and step-quenched Al-6Zn-1.2Mg alloy, respectively[7].

[9, 12]. These initial observations showed that the formation of GP zone solute clusters in Al-Zn-Mg alloys was more complicated that originally suspected. In 1978 Chou reported an updated precipitation sequence involving two types of GP zones

$$\alpha - SSSS \rightarrow GPZ_{unordered} \rightarrow GPZ_{ordered} \rightarrow \eta\prime \rightarrow \eta(MgZn_2). \tag{2.2}$$

Where the unordered GP zones were FCC solute rich clusters, and the ordered GP zones possessed a hexagonal phase structure and a spherical morphology. These ordered hexagonal clusters acted as a precursor to the formation of the plate-like $\eta\prime$ phase, which was consistent with earlier observations [6, 26]. The presence of two types of GP zones came to be widely accepted, with their role in the precipitation process eventually reported as a dual-pathway process, shown in Figure 2.6 [11].

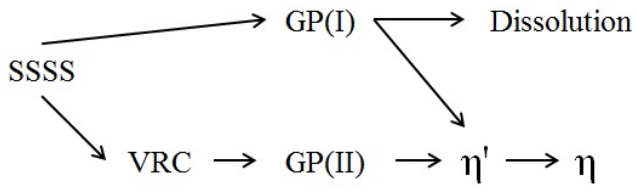

Figure 2.6: The precipitation process in Al-Zn-Mg-Cu alloys as reported by Werenskiold et al.

GP(I) zones are considered to be coherent, spherical, and possibly Mg-rich clusters that are ordered on the $\{001\}_{Al}$ plane and which are formed over a wide temperature range and therefore not dependent on the presence of quenched-in vacancies [10, 11, 27]. While these zones do appear in the material prior to the formation of $\eta\prime$, the formation of $\eta\prime$ on large stable GP(I) zones is not the dominant mechanism of nucleation [10]. The presence of Cu has been shown to stabilize small GP(I) zones and allow for the transformation of these clusters into $\eta\prime$, but more often GP(I) zones are believed to dissolve back in the matrix, allowing for the recombination of solutes into the $\eta\prime$ phase [10, 11]. By contrast GP(II) zones are Zn-rich solute clusters that appear on the $\{111\}_{Al}$ plane and are ordered internally through elongation in the <110> direction [10, 27]. These GP zones do require the presence of excess vacancies, and are only nucleated at temperatures greater than 70 °C [10, 11, 27]. It is these ordered zones which were originally suspected to the be a precursor to the $\eta\prime$ formation, and eventually Maloney et al. confirmed that this process occurs via direct transformation of the GP zones into the hexagonal η phase, rather than through nucleation of a new phase on a heterogeneous nucleation site [8].

The composition of the metastable $\eta\prime$ phase was originally assumed to be the same as the equilibrium η phase ($MgZn_2$). However, since the formation of $\eta\prime$ is sensitive to solute clustering in the alloy, it is not surprising that the composition of $\eta\prime$ is closer to that of the precursor GP zones [8, 10, 24, 28]. While the Zn:Mg ratio has been reported as anything from 1:1 to 1.5:1, a direct correlation between the overall alloy composition and the composition of GP zones and the $\eta\prime$ phase was first reported by Maloney et al.. This work reported a linear relationship between the atomic Zn:Mg and (Zn+Cu):Mg solution ratio found in the parent alloy and in the GP zones and $\eta\prime$ precipitates, as seen in Figure 2.7 [24].

This relationship may help explain the presence of two different types of GP zones

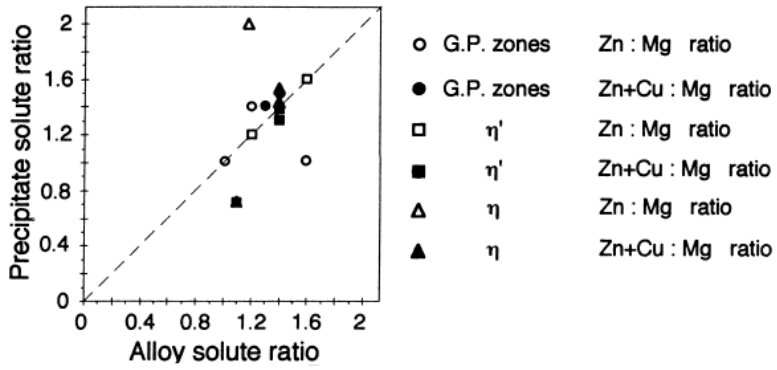

Figure 2.7: The measured solute ratio of various precipitates versus the alloy solute ratio.

that are alternatively either Mg- or Zn- rich, and the effect of Cu on stabilizing small Mg-rich GP(I) zones and inducing their elongation and transformation to $\eta\prime$ precipitates [10]. This elongation and transformation into $\eta\prime$ precipitates is the same process that Zn-rich GP(II) clusters undergo in their precipitation sequence [8]. Therefore, it is possible that what drives the difference between GP(I) and GP(II) zones and determines their ability to transform into $\eta\prime$ platelets is the (Zn+Cu):Mg ratio in the solute cluster, which may in turn be controlled by the (Zn+Cu):Mg ratio of the parent alloy. This theory of GP zone transformation is also consistent with the observation of $T\prime$ and T phases at low Zn:Mg ratios, and maybe help explain the different hexagonal phase orientations of $\eta\prime$ and η that have been observed [14, 26].

The presence of GP zones and $\eta\prime$ precipitates is generally associated with the peak strength condition of the alloy, but with additional aging $\eta\prime$ transforms in to the equilibrium η phase with a Zn:Mg ratio of 2:1, as expected [24]. The equilibrium phase is also the predominant precipitate found on grain boundaries. It has been observed by numerous authors that the addition of Cu in the parent alloy leads to the incorporation of Cu in these equilibrium grain boundary precipitates, but only in the over-aged

condition [18, 29, 30, 31, 32, 33, 34, 35]. While many have postulated that Cu substitutes for Zn in these precipitates, Wert reported that these Cu-containing precipitates are actually a solid solution of the isomorphous phases $MgZn_2$ and Mg(AlCu), both of which possess a C14 hexagonal crystal structure [29].

The notion that a critical aging temperature must be reached before Cu begins to incorporate into the grain boundary precipitates is well supported, since the effect is not observed in peak-aging treatments at lower temperatures [30, 31]. However there is also evidence to suggest that there is a critical concentration of Cu in the parent alloy that is required for the solid solution to form. A recent study by Gupta et al. observed that grain boundary precipitates in 7150 had 16x as much Cu as the same precipitates in 7079, even though 7150 only contains twice as much Cu in the parent alloy [18]. Once these conditions are met, the equilibrium or maximum possible amount of Mg(AlCu) increases, both with increasing the amount of Cu in the parent alloy and with increasing the temperature of aging, causing the particles to become more stable [18, 30, 31, 32]. One explanation of this phenomenon would be that as the amount of Zn near the grain boundaries is depleted, the precipitates continue to grow by the addition of Cu instead. However, this is not the case, since it has been well documented that as the amount of Cu in the grain boundary precipitates increases, the amount of Zn in those same precipitates decreases and that the total particle size stays the same [18, 31, 32]. The substitution is well illustrated by Marlaud et al. in Figure 2.8.

This suggests instead that as the alloy continues to age, the precipitate is approaching a solid solubility containing an equilibrium mole fraction of $MgZn_2$ and Mg(AlCu). Wert reported the mole fraction of the two phases to be .70 and .30, respectively, and described the solid solution particle as $Mg(Zn_2,AlCu)$ [29]. More recently Marlaud

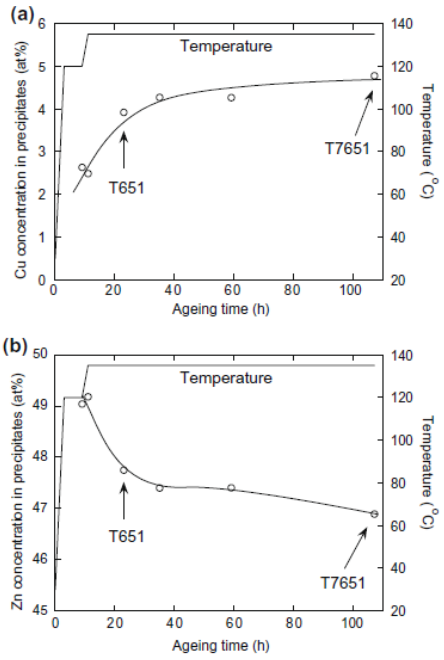

Figure 2.8: Evolution of (a)Cu and (b)Zn concentrations in the grain boundary precipitates during aging treatment.

et al. suggested an equilibrium totaling 33at% Mg, 13at% Cu, 10-15at% Al, and a balance of Zn, which suggests a mole fraction of .40 Mg(AlCu) [31].

2.3.2 Traditional Processes

When the modern version of 7075 was first introduced by Alcoa in 1943, it was initially used for aerospace products with a peak-strength (T6) heat treatment in thin sections, mainly sheets and some extrusions. The alloy became highly valued in the aerospace field for its high strength-to-weight ratio, and was increasingly incorporated into aircraft design, perhaps most famously during its inclusion on the B-29 Flying Fortress. However, as 7075 was utilized for increasingly thick components manufactured from large forgings, extrusions, and thick plate it became increasingly apparent that although 7075-T6 possessed great strength, other properties such as fracture toughness, fatigue properties, and stress corrosion cracking (SCC) resistance were lacking [1, 3, 36, 37]. As a result, various heat treatments and alloy modification were

designed with the aim of improving these properties. One of these high-purity alloy modifications, intended to improve the fracture toughness, was 7050 [1]. Early heat treatments that were developed in the 1960s included T73 to improve stress corrosion cracking resistance, T76 to improve exfoliation corrosion, and T74 [1, 36].

The degree of aging in the material has been traditionally measured by tracking the conductivity of the material with respect to time at a certain temperature. When the change in the resistivity of the material reaches a peak, the material is presumed to also reach a peak in strength due to the presence of finely dispersed GP zones or η precipitates in the grain bulk [1, 3, 7]. An example of this type of curve is seen in Figure 2.5. This T6, or peak-strength, heat treatment is usually carried out at a single moderate aging temperature such as 120 °C for a long period of time, usually 24 hours [2, 38]. Over-aged heat treatments such as T73, T74, or T76 usually consist of a first step at this same temperature to create this same fine dispersion of precipitates, followed by a second step at an elevated temperature, usually 163 °C for anywhere from 6 to 24 hours to coarsen the grain boundary η precipitates in an attempt to improve the corrosion properties [2, 36, 38]. While these tempers do shown an improvement in corrosion and fracture toughness properties, it comes with a sacrifice in the tensile strength of the material [2, 17, 19, 22, 36, 39, 40, 41, 42, 43].

2.3.3 Experimental Treatments

Since then, the exploration of heat-treatments to optimize the trade-off between strength, fracture toughness, ductility, and corrosion properties has been constant. Some of the most notable treatments include retrogression and re-aging (RRA) treatments, Alcoa's T77 treatment, and the newly developed T6I6 and T6I4 treatments.

In 1974, Cina first introduced a three-step aging process termed "retrogression and re-aging" [3]. This process was found to improve corrosion and fracture toughness properties in 7xxx series alloys with a minimal loss in strength [2, 3, 36, 40, 44, 45, 46, 47, 48, 49]. Retrogression and re-aging (RRA) treatments were originally based on the theory that the presence of dislocations other than grain boundaries contributed to lower SCC resistance. Therefore the process involves first heating the material to a T6 temper, then increasing the aging temperature to a high enough temperature to promote the annealing or retrogression of dislocations (typically about 200 °C) for a short enough period of time to not allow for over-aging (usually on the order of minutes), and then re-aging the material with another T6 heat-treatment [2]. While the improvement on the properties was observed as expected, the reasons for that improvement were not due to the annealing of dislocations in the matrix. Rather, the treatment works by partially dissolving the GP zones and $\eta\prime$ particles that are present in the bulk of the grain during the retrogression, while still allowing the η particles at the grain boundaries to stabilize and grow. During re-aging the GP zones and $\eta\prime$ particles are reformed in the grain bulk to nearly the same size and density as they were under the original T6 treatment, but are more thermodynamically stable [44, 46, 47]. The two controlling factors of this heat treatment then, are the amount of time and the temperature at which the retrogression takes place.

Ideally, the retrogression step would be controlled to allow the strengthening particles to have dissolved as much as possible, but not last so long as to allow for precipitation to reoccur at this elevated temperature. It can be expected then, that at a constant retrogression temperature, increasing the amount of time at this step would result in a gradual change of the grain bulk properties, mainly tensile strength, from that of a peak-aged temper to an over-aged temper. And indeed this relationship is observed by Li et al. for multiple retrogression temperatures, as seen in Figure 2.9 [46].

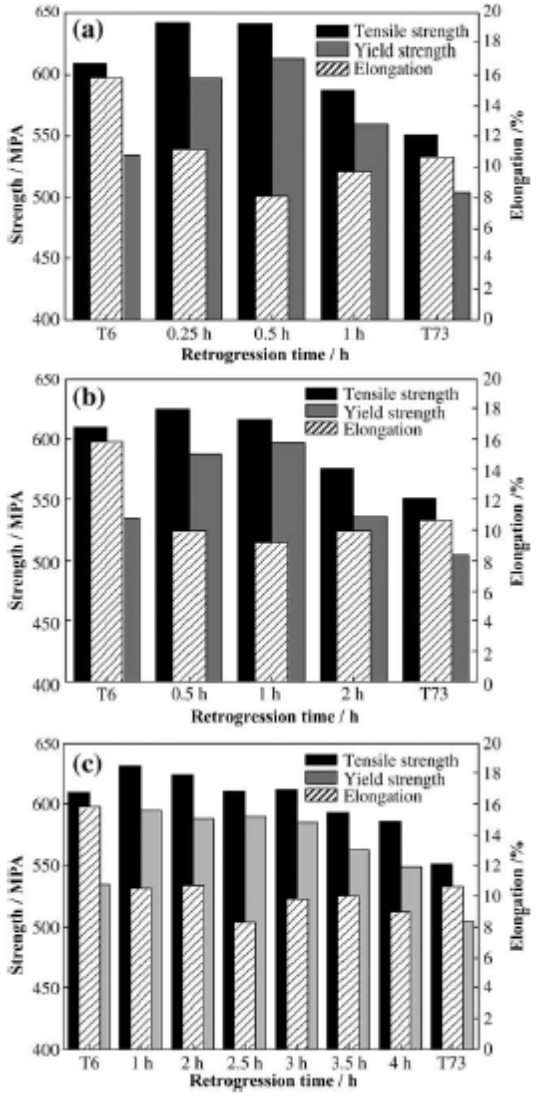

Figure 2.9: Strength and elongation of 7150 retrogressed for various times at retrogression temperatures of (a)195°C, (b)185°C, and (c)175°C; followed by re-aging.

Similarly, it is expected that increasing the temperature of the retrogression step would mean that shorter times are required for the particles to dissolve. What is surprising is that it has also been observed that increasing the retrogression temperature increases the thermodynamic stability of the precipitates on re-aging [47]. This may be explained by the higher levels of Cu observed by Ning et al. in both grain bulk

and grain boundary precipitates after RRA, as compared to the original T6 treatment [48].

Treatment	Position	Zn	Mg	Cu
100 ℃, 24 h	Grain boundary	6.50	3.90	3.10
	Grain interior	6.45	4.05	3.00
100 ℃, 24 h+200 ℃, 7 min	Grain boundary	6.90	4.55	2.55
	Grain interior	6.90	6.00	2.60
100 ℃, 24 h+200 ℃, 7 min+100 ℃, 24 h	Grain boundary	6.30	4.90	3.70
	Grain interior	3.70	4.40	4.20

Figure 2.10: Molar fraction (%) of elements in grain interior and grain boundary precipitates of Al-Zn-Mg-Cu alloy after different treatments.

More evidence for this increased stability is also observed by Ning et al. As the (Zn+Cu):Mg ratio increased in the different alloys that were tested, the alloys showed an increasing drop in the strength with retrogression time, as shown in Figure 2.11. This implies that increasing the (Zn+Cu):Mg ratio, which is known to increase the stability of the GP Zones and enable their transformation into η particles, similarly enables the precipitation process at retrogression temperatures and likely enhances the incorporation of Cu into precipitates upon re-aging even further [48].

Although RRA treatments have been shown to improve the overall performance of 7050 and other high-strength aluminum alloys, other heat-treatments have continued to be explored in an effort to find even more improvement. A decade after the RRA treatment was introduced, Alcoa patented its own three-step aging process, known at T77 [3, 36]. This treatment has been known to provide excellent exfoliation resistance, similar to the T76 temper, but with no sacrifice to strength and improved SCC resistance over the T6 temper [36]. The beneficial performance that came with improved combinations of strength, corrosion, and fracture toughness properties has made 7150-T77 parts critical in modern aircraft applications [36, 39, 49]. Even though both the T77 and RRA treatments involve three steps, they are not as similar as one

Alloy No.	Zn	Mg	Cu
1	6.28	2.19	1.60
2	9.99	2.50	1.72
3	12.2	2.48	2.00

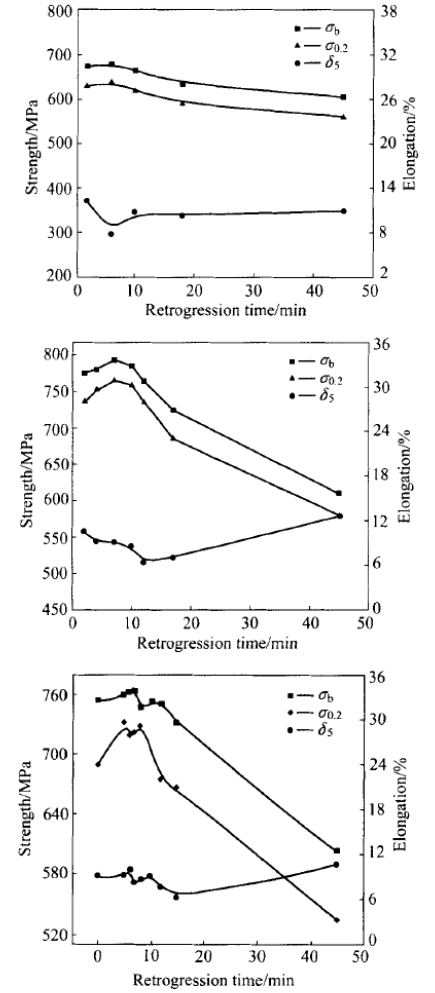

Figure 2.11: The strength of three different Al-Zn-Mg-Cu alloys that were retrogressed at 200°C for various times, measured following re-aging.

might expect. Rather, the T77 is similar to other over-aging tempers, but with an initial step at a lower pre-aging temperature of approximately 100 °C. After this step, a more traditional two-step aging process follows. This heat treatment seems to be particularly effective for improving parts in thick or poorly quenched components [3].

A more recent heat-treatment that has been shown to result in an improved performance profile is the development of interrupted aging treatments T6I6 and T6I4 by Lumley, Polmear, and Morton [50, 51, 52, 53]. This class of heat-treatments utilizes secondary precipitation at relatively low aging temperatures to form a dispersion of $\eta\prime$ particles that is more finely distributed than that found in the T6 temper [50]. The process involves heating the alloy at the normal T6 temperature, but then interrupting that treatment with a low-temperature dwell period at 25-65 °C for anything from several hours to a few weeks, before resuming the standard T6 temperature for the rest of the original aging period. Thus, this process is termed T6I6, where the I indicates that the process was interrupted by a dwell period. This differs only slightly from the T6I4 process, where the resumption of the artificial aging process is eliminated. General schematics of both the T6I6 and the T6I4 processes are shown in Figure 2.12.

In both processes the GP(I) zones that are formed during under-aging treatment, which are usually dissolved due to Oswald ripening during continued aging to a T6 temper, are instead utilized in the formation of $\eta\prime$ at lower secondary aging temperatures. Therefore, even when artificial aging is not resumed, the final microstructure consists of finer and more densely populated $\eta\prime$ precipitates than the typical T6 temper [25]. After the dwell period, the fracture toughness increases by as much as 40% in 7050 with only a minimal decrease in strength. After resuming artificial aging, the effect on the fracture toughness is not as pronounced (only 9%), but the strength of the alloy is increased over the T6 temper [50, 51, 52, 53]. These results are summarized for 7050 aluminum in Table 2.1.

While RRA, T77, and the new interrupted T6I4 and T6I6 treatments represent some of the most noteworthy heat-treatment developments over the last several decades,

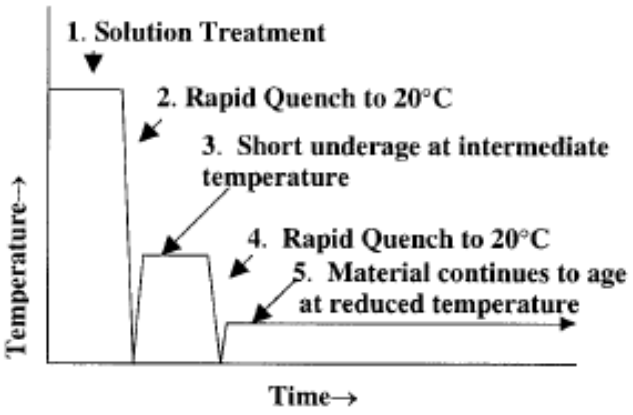

(a) T614

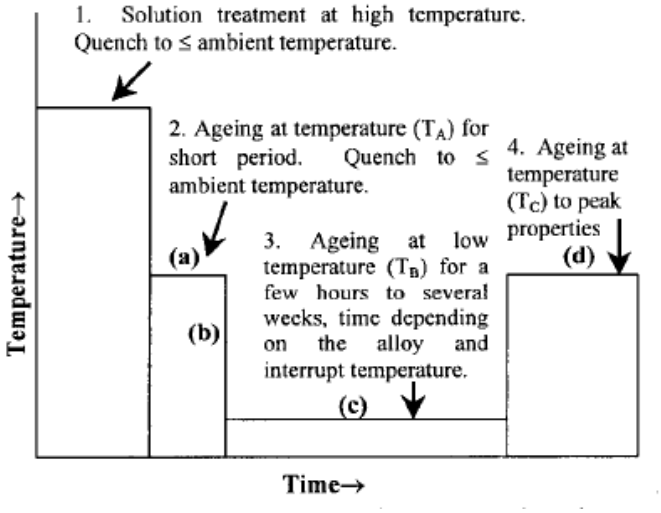

(b) T6I6

Figure 2.12: General schematics representing the interrupted aging treatments.

Table 2.1: Mechanical properties of the interrupted aging treatments in 7050 aluminum, as reported by Lumley et al.

	0.2% Proof Stress (MPa)	Tensile Strength (MPa)	Elongation(%)	Plane-Strain Fracture Toughness ($MPa\sqrt{m}$)
T6	546	621	14	38
T6I4	527	626	16	52
T6I6	574	639	14	41

it is important to recognize that the exploration of new heat-treatment processes to further optimize the mechanical properties of the final alloy is still ongoing.

2.4 Summary

This chapter discussed the heat treatment steps often applied to wrought high-strength aluminum alloys in this system, including the solution heat treatment the quenching and the aging heat treatment. Although most wrought aluminum alloy products are stretched after the quenching step and prior to the aging process, the affect of this stretching step is not discussed here. However, these processes are some of the most commonly examined and manipulated in both academia and industry in an attempt to control the mechanical properties of the alloy, and information regarding 'pre-stretching' can be found elsewhere. Due to the focus on these 'post-processing' steps, it is unsurprising that the process-structure and structure-property relationships involving these processing steps are some of the most well known and developed relationships within the material. The deep knowledge base regarding these relationships that has been developed over time, their importance in the performance of the alloy, as well as their complexity which has been shown here, all mean that it is particularly important that the processing history of these steps be well documented and these relationships mapped in a standard way.

2.5 References

[1] J. R. Davis, editor. *Aluminum and Aluminum Alloys*. ASM International, 1993.

[2] J. Beddoes. Design of solution heat treatments for aerospace alloys. *Canadian Metallurgical Quarterly*, 3:215–221, 50.

[3] Justin Lamb. *Decomposition and its effects on Mechanical Properties in Al-Zn-Mg-Cu Alloys*. PhD thesis, Georgia Instiute of Technology, 2015.

[4] N. M. Han, X. M. Zhang, S. D. Liu, D. G. He, and R. Zhang. Effect of solution treatment on the strength and fracture toughness of aluminum alloy 7050. *Journal of Alloys and Compounds*, 509:4138–4145, 2011.

[5] David A. Porter, Kenneth E. Easterling, and Mohamed Y. Sherif. *Phase Transformation in Metals and Alloys*. CRC Press, 3rd edition edition, 2009.

[6] J. D. Embury and R. B. Nicholson. The nucleation of precipitates: The system Al-Zn-Mg. *Acta Metallurgica*, 13:403–417, 1965.

[7] K. Asano, M. Abe, and A. Fujiwara. Nucleation of precipitates in al-zn-mg alloys. *Materials Science and Engineering*, 22:61–70, 1976.

[8] S. K. Maloney, K. Hono, I. J. Polmear, and S. P. Ringer. The effects of a trace addition of silver upon elevated temperature ageing of an Al-Zn-Mg alloy. *Micron*, 32:741–747, 2001.

[9] P. Kenesei, G. Horvath, S. Bernstorff, T. Ungar, and J. Lendvair. Early stages of nucleation and growth of guinier-preston zones in Al-Zn-Mg and Al-Zn-Mg-Cu alloys. *Zeitschrift fur Metallkunde*, 97:315–320, 2006.

[10] Gang Sha and Alfred Cerezo. Early-stage precipitation in Al-Zn-Mg-Cu alloy (7050). *Acta Materialia*, 52:4503–4516, 2004.

[11] J. C. Werenskiold, A. Deschamps, and Y. Brechet. Characterization and modeling of precipitation kinetics in an al-zn-mg alloy. *Materials Science & Engineering, A: Structural Materials: Properties, Microstructure and Processing*, 293:267–274, 2000.

[12] C. Wolverton. Solute-vacancy binding in aluminum. *Acta Materialia*, 55:5867–5872, 2007.

[13] Z. W. Huang, M. H. Loretto, R. E. Smallman, and J. White. The mechanism of nucleation and precipitation in 7075-0.7Li alloy. *Acta Metallurgica*, 42:549–559, 1994.

[14] S. P. Ringer and K. Hono. Microstructural evolution and age hardening in aluminum alloys: Atom probe field-ion microscopy and transmission electron microscopy studies. *Materials Characterization*, 44:101–131, 2000.

[15] R. G. Song, W. Dietzel, B. L. Zhang, W. J. Liu, M. K. Tseng, and A. Atrens. Stress corrosion cracking and hydrogen embrittlement of an Al-Zn-Mg-Cu alloy. *Acta Materialia*, 52:4727–2743, 2004.

[16] T. Ogura, S. Hirosawa, and T. Sato. Quantitative characterization of precipitate free zones in Al-Zn-Mg(-Ag) alloys by microchemical analysis and nanoidentation measurement. *Science and Technology of Advanced Materials*, 5:491–496, 2004.

[17] T. H. Sanders and E. A. Starke. Relationship of microstructure to monotonic and cyclic straining of 2 age hardening aluminum alloys. *Metallurgical Transactions A*, 7:1407–1418, 1976.

[18] R. K. Gupta, A. Deschamps, M. K. Cavanaugh, S. P. Lynch, and N. Birbilis. Relating the early evolution of microstructure with the electrochemical response

and mechanical performance of a Cu-rich and Cu-lean 7xxx aluminum alloy. *Journal of The Electrochemical Society*, 159:492–502, 2012.

[19] D. Dumont, A. Deschamps, and Y. Brechet. On the relationship between microstructure, strength and toughness in aa7050 aluminum alloy. *Materials Science & Engineering, A: Structural Materials: Properties, Microstructure and Processing*, 356:326–336, 2003.

[20] A. Deschamps, G. Texier, S. Ringeval, and L. Delfaut-Durut. Influence of cooling rate on the precipitation microstructure in a medium strength al-zn-mg alloy. *Materials Science & Engineering, A: Structural Materials: Properties, Microstructure and Processing*, 501:133–139, 2009.

[21] X. Zhang, W. Liu, S. Liu, and M. Zhou. Effect of proprocess parameters on quench sensitivity of an aa7050 sheet. *Materials Science & Engineering, A: Structural Materials: Properties, Microstructure and Processing*, 528:795–802, 2011.

[22] Alcoa. Alloy 7050 plate and sheet, 2016.

[23] John W. Cahn. A historical perspective on the utilization of phase diagrams for precipitation hardening. *Bulletin of Alloy Phase Diagrams*, 4:349–351, 1983.

[24] S. K. Maloney, K. Hono, I. J. Polmear, and S. P. Ringer. The chemistry of precipitates in an aged al-2.1zn-1.7mg at *Chemistry of Precipitates*, 41:1031–1038, 1999.

[25] J. Buha, R. N. Lumley, and A. G. Crosky. Secondary ageing in an aluminum alloy 7050. *Materials Science & Engineering, A: Structural Materials: Properties, Microstructure and Processing*, 492:1–10, 2008.

[26] An-Chich Chou. On the precipitation of eta' phase in an Al-Zn-Mg alloy. *Scripta Metallurgica*, 12:421–423, 1978.

[27] J. Chen, L. Zhen, S. Yang, W. Shao, and S. Davis. Investigation of precipitation behavior and related hardening in AA7075 aluminum alloy. *Materials Science & Engineering, A: Structural Materials: Properties, Microstructure and Processing*, 500:34–42, 2009.

[28] K. Stiller, P. J. Warren, V. Hansen, J. Angente, and J. Gjonnes. Investigation of precipitation in an Al-Zn-Mg alloy after two-step ageing treatment at 100 and 150 degrees c. *Materials Science & Engineering, A: Structural Materials: Properties, Microstructure and Processing*, 270:55–63, 1999.

[29] John A. Wert. Identification of precipitates in 7075 Al after high-temperature aging. *Scripta Metallurgica*, 15:445–447, 1981.

[30] J. K. Park and A. J. Ardell. Microchemical analysis of precipitate free zones in 7075-Al in the T6, T7, and RRA tempers. *Acta Metallurgica*, 39:591–598, 1991.

[31] T. Marlaud, A. Deschamps, F. Bley, W. Lefebre, and B. Baroux. Influence of alloy composition and heat treatment on precipitate composition in al-zn-mg-cu alloys. *Acta Materialia*, 58:248–260, 2010.

[32] R. Goswami, S. Lunch, N. J. H. Holroyd, S. P. Knight, and R. L. Holtz. Evolution of grain boundary precipitates in Al 7075 upon aging and correlation with stress corrosion cracking behavior. *Metallurgical and Materials Transactions A: Physical Metallurgy and Materials Science*, 44A:1268–1278, 2013.

[33] L. Huang, K. Chen, and S. Li. Influence of grain-boundary pre-precipitation and corrosion characteristics of inter-granular phase on corrosion behavior of an Al-Zn-Mg-Cu alloy. *Materials Science & Engineering, B: Solid-State Materials for Advanced Technology*, 177:862–868, 2012.

[34] S. P. Knight, N. Birbilis, B. C. Muddle, A. R. Trueman, and S. P. Lynch. Correlations between intergranular stress corrosion cracking, grain-boundary microchemistry, and grain-boundary electrochemistry for Al-Zn-Mg-Cu alloys. *Corrosion Science*, 52:4073–4080, 2010.

[35] T. Ramgopal, P. I. Gouma, and G. S. Frankel. Role of grain-boundary precipitates and solute-depleted zone on the intergranular corrosion of aluminum alloys 7150. *Corrosion*, 58:687–697, 2002.

[36] J. R. Davis, editor. *Corrosion of Aluminum and Aluminum Alloys*. ASM Internation, 1999.

[37] H. Y. Hunsicker. Development of Al-Zn-Mg-Cu alloys for aircraft. *Philosophical Transactions of the Royal Society of London*, 282:359–376, 1976.

[38] ASTM International. B918: Standard practice for heat treatment of wrought aluminum alloys, March 2009.

[39] Alcoa. Alloy 7150 plate and sheet, 2016.

[40] N. M. Han, X. M. Zhang, S. D. Liu, B. Ke, and X. Xin. Effects of pre-stretching and ageing on the strength and fracture toughness aluminum alloy 7050. *Materials Science & Engineering, A: Structural Materials: Properties, Microstructure and Processing*, 528:3714–3721, 2011.

[41] N. Kamp, I. Sinclair, and M. J. Starink. Toughness-strength relations in the overaged 7449 Al-based alloy. *Metallurgical and Materials Transactions A: Physical Metallurgy and Materials Science*, 33A:1125–1136, 2002.

[42] N. U. Deshpande, A. M. Gokhale, D. K. Denzer, and John Liu. Relationship

between fracture toughness, fracture path, and microstructure of 7050 aluminum alloy: Part i. quantitative characterization. *Metallurgical and Materials Transactions A: Physical Metallurgy and Materials Science*, 29A:1191–1201, 1998.

[43] Gerard M. Ludtka and David E. Laughlin. The influence of microstructure and strength on the fracture mode and toughness of 7xxx series aluminum alloys. *Metallurgical Transactions A*, 13A:411–425, 1982.

[44] A. Karaaslan, I. Kaya, and H. Atapek. Effect of aging temperature and of retrogression treatment time on the microstructure and mechanical properties of alloysAA7075. *Metal Science and Heat Treatment*, 49:443–447, 2007.

[45] Z. Li, B. Xiong, Y. Zhang, B. Zhu, F. Wang, and H. Liu. Ageing behavior of an Al-Zn-Mg-Cu alloy pre-stretched thick plate. *Journal of University of Science and Technology Beijing*, 14:246–250, 2007.

[46] J. F. Li, N. Birbilis, C. X. Li, Z. Q. Jia, B. Cai, and Z. Q. Zheng. Influence of retrogression temperature and time on the mechanical properties and exfoliation corrosion behavior of aluminum alloy AA7150. *Materials Characterization*, 60: 1334–1341, 2009.

[47] F. Viana, A. M. P. Pinto, H. M. C. Santos, and A. B. Lopes. Retrogression and re-ageing of 7075 aluminum alloy: Microstructural characterization. *Journal of Materials Processing Technology*, 92-93:54–59, 1999.

[48] A. Ning, Z. Liu, B. Peng, and S. Zeng. Redistribution and re-precipitation of solute atom during retrogression and reaging of Al-Zn-Mg-Cu alloys. *Trans. Nonferrous Met. Soc. China*, 17:1005–1011, 2007.

[49] A. F. Oliveira, M. C. de Barros, K. R. Cardoso, and D. N. Travessa. The effect of RRA on the strength and SCC resistance on AA7050 and AA7150 aluminum alloys. *Materials Science & Engineering, A: Structural Materials: Properties, Microstructure and Processing*, 379:321–326, 2004.

[50] R. N. Lumley, I. J. Polmear, and A. J. Morton. Control of secondary precipitation to improve the performance of aluminum alloys. *Materials Science Forum*, 396-402:893–898, 2002.

[51] R. N. Lumley, I. J. Polmear, and A. J. Morton. Development of properties during secondary ageing of aluminum alloys. *Materials Science Forum*, 426-432: 303–308, 2003.

[52] R. N. Lumley, I. J. Polmear, and A. J. Morton. Interrupted aging and secondary precipitation in aluminum alloys. *Materials Science and Technology*, 19:1483–1492, 2003.

[53] R. N. Lumley, I. J. Polmear, and A. J. Morton. Development of mechanical properties during secondary aging in aluminum alloys. *Materials Science and Technology*, 21:1025–1033, 2005.

CHAPTER 3

MECHANICAL PROPERTIES OF INTEREST

There are a wide variety of mechanical properties that might be of interest in high-strength Al-Zn-Mg-Cu alloys. However this work will focus on those that are traditionally of interest in aircraft applications: namely the strength, fracture toughness, and stress corrosion cracking properties. While other properties, such as fatigue, are often considered important or of interest in many situations, the tensile strength, fracture toughness, and corrosion resistance are the three most common parameters that are examined for optimization.

3.1 Tensile Strength

The strength properties of interest in 7xxx series alloys are usually the yield strength and the ultimate strength in tension, and the work hardening ability of the material. These properties are usually measured experimentally through standard ASTM E8 tensile test procedures. Although these alloys are known for being heat-treatable and precipitation-hardened, there are actually multiple strengthening mechanisms that are present, including the strength due to the presence of grain boundaries, the effect of texture, solution strengthening from the solutes that remain in the matrix, and the strengthening effect due to dislocation-dislocation interactions beyond the interactions that dislocations have with the strengthening precipitates. Many attempts at modeling the predictive strength of 7xxx series alloys have been made, with the most successful models taking in to account all of the major mechanisms and then employing varying levels of superpositioning to predict the combined effect [1, 2, 3, 4]. Similarly, while efforts to optimize the strength of these alloys have traditionally

focused on the optimization of the precipitate size, understanding the effect that processing parameters and microstructure characteristics have on the other contributing mechanisms is crucial.

3.1.1 The Presence of Grain Boundaries and Texture

The strength contribution due to the presence of grain or sub-grain boundaries is probably the most often overlooked of these microstructure effects, even though the strengthening contribution can be quite large, particularly in partially recrystallized materials [1, 2, 5, 6, 7]. It has been shown that increasing the amount of recrystallization in the alloy decreases the overall strength, largely due to an eradication of sub-grain cell structures [6, 7]. It is well known that as the grain size of a material decreases, this causes an increase in the flow stress. For grains that are larger than 20 μm this relationship has been shown to agree well with that reported by Hall and Petch [5]. However, for cell sizes in the range of 2-5 μm, such as those found in unrecrystallized grains, the effect becomes even more pronounced as the flow stress becomes inversely proportional to the cell size (rather than the square of the cell size as previously expected). This relationship has been observed to hold regardless of the degree of mis-orientation of the sub-grain boundaries, meaning that it is independent of texture [5]. Not only does the grain or sub-grain size affect the yield strength, but it also affects the post-yield behavior of the alloy. In fine-grained structures, the material is relatively clear of dislocations before deformation begins, and at higher strains the dislocations become accumulated at the grain boundaries, where they are more likely to rearrange and annihilate. When the grain size becomes large, the distance the dislocation must travel to a grain boundary becomes orders of magnitude larger than the free slip distance, meaning the dislocations become accumulated in the bulk and are less able to dynamically recover. Therefore, coarse-grain materials exhibit higher levels of work hardening, which can be attributed to a decreased ability

to dynamically recover when dislocations become accumulated [5, 6]. It is important to remember that the average grain size of recrystallized regions, the average cell size in non-recrystallized regions, and the relative amount of recrystallization in the alloy all play a crucial role in determining the strength properties of interest in the material.

Although the effect that grain boundaries have on the yield strength has been shown to be relatively independent of the mis-orientation angle of said boundaries, it is important to understand the texture of the alloy does play a role in the post-yield behavior. This is because the post-yield behavior of the alloy is directly related to the accumulation of dislocation loops, as previously mentioned. The accumulation of these dislocations leads to hardening and the accumulation of stress, which subsequently results in either (1) matrix plastic relaxation or (2) failure if the matrix is unable to relax these strain incompatibilities. In some cases, this relaxation occurs by lattice rotation [2, 8]. In most predictive models, this effect is accounted for through the use of an M factor, or a Taylor factor [2, 3].

3.1.2 Precipitation Hardening and Dislocation Interactions

Similarly, the precipitation-hardening effect is also caused by an increased ability to trap and accumulate dislocations in the material. Here, the formation of coherent solute clusters causes a great deal of strain due to the volume or lattice mismatch that occurs in the matrix. This cluster stabilizes dislocations, since their presence reduces the strain. When precipitates become large and increasingly incoherent, they lose the ability to stabilize these dislocations. At large sizes they become instead physical barriers to dislocation movement, since the only way for a dislocation to circumvent the particles is by bowing into a roughly semi-circular shape between them. When this bypassing is done without the aid of cross-slip, it is referred to as Orowan looping [1, 8, 9, 10, 11, 12]. Since small coherent particles are cut by the moving dislocations

their strength contribution is proportional to their average size and volume fraction. Once they become large enough that dislocation bypassing takes place, their strength contribution becomes inversely proportional to their radius, though it still increases as the square of the volume fraction increases [11, 12]. It can be expected then, that the maximum strengthening effect would be reached when this critical size for the shearing-bypass transition is reached, as depicted in Figure 3.1[11].

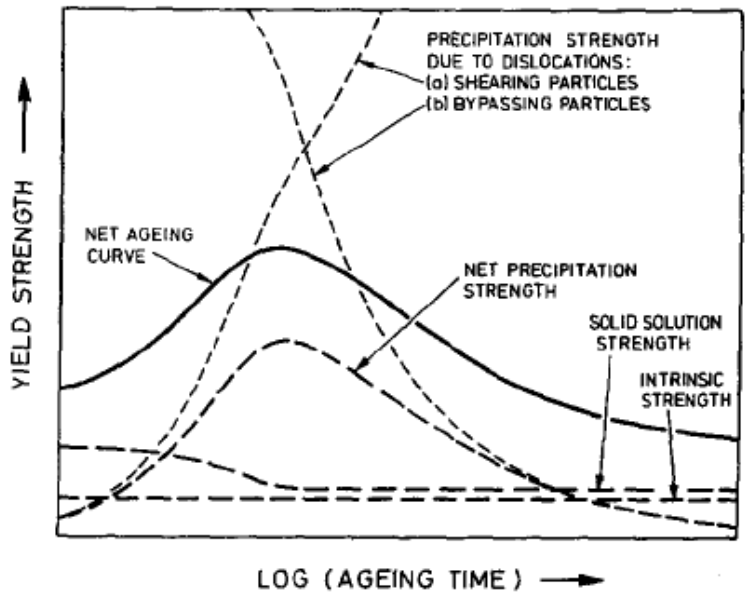

Figure 3.1: A schematic showing the relative contributions to the yield strength as a function of aging.

This transition was originally suspected to occur when coherent GP zones transitioned to semi-coherent $\eta\prime$ particles, since coherent particles are more effective at stabilizing dislocations [8, 9]. However, it has been well observed in 7050 and other alloys in this series that the peak-strength condition is characterized primarily by the presence of small (approximately 3nm), well dispersed $\eta\prime$ precipitates [13, 14, 15, 16, 17]. This is supported by evidence that the plate-like $\eta\prime$ precipitates are either partially or fully coherent with a low degree of lattice misfit across the {111} habit plane, and that dislocations do pass through these partially coherent particles after being initially held up at the surface [9, 13]. Since $\eta\prime$ precipitates do provide more of a strengthening

affect than GP zones in these alloys, it is possible that the stabilizing effect of Cu on GP zones and enabling of $\eta\prime$ might be the reason that the presence of Cu has been shown to increase the strength [13, 16].

Since the accumulation of dislocations hardens the material only after yield, pre-straining the material to increase the dislocation density prior to aging has been attempted to improve the yield-strength [14]. While this may increase the yield strength initially, it cannot increase the ultimate strength; since the presence of additional dislocations does not affect the ability of the material to dynamically recover or work harden. Cold-rolling the material prior to aging also increases the dislocation density prior to yielding, but through a slightly different means [15]. Just as it does during the post-homogenization process, the material dynamically recovers and accommodates the strain energy through the formation of equiaxed sub-grain cell structures. As discussed, this decrease in the average sub-grain cell size is more effective at increasing both the yield strength and the ultimate strength of the material. The increasing dislocation density with cold rolling and the subsequent effect on the strength properties as compared to pre-straining the material are all shown in Figures 3.2-3.4[14, 15].

3.1.3 Solution Strengthening

After precipitation has occurred, there are still small amounts of solute that are left in solid solution in the matrix. The presence of these solutes contributes to the final strengthening mechanism, solid solution strengthening. Although this can be a meaningful contribution to the overall strength of the alloy, it is much smaller than some of the others discussed [18]. The amount of strength the remaining solute would be able to impart to the alloy if it was incorporated in to additional precipitates is

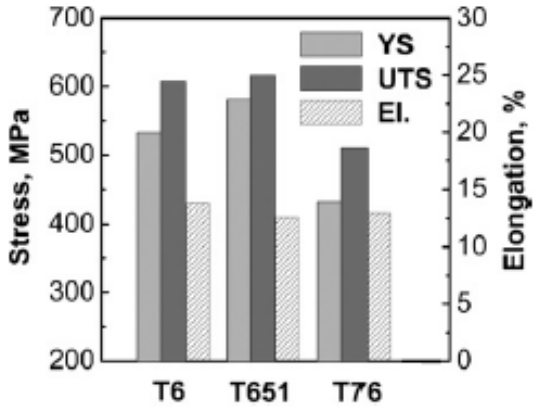

Figure 3.2: Tensile properties of 7050 with various ASTM standard heat treatments, as reported by Wang et al. A treatment ending in -51 indicates a material that was pre-stretched prior to the aging heat treatment, as per ASTM B918.

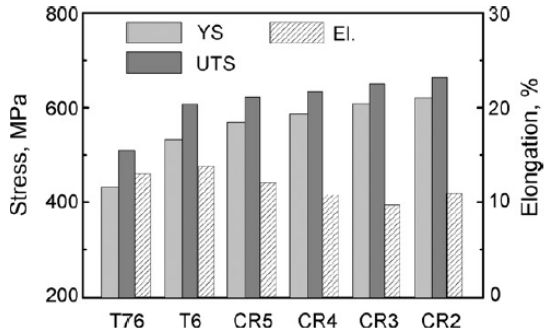

Figure 3.3: The tensile properties of 7050 when increasing amounts of cold rolling are applied, as reported by Wang et al. CR2, CR3, CR4, and CR5 indicate samples that were rolled to 2mm, 3mm, 4mm, and 5mm, respectively.

actually much higher than the contribution from remaining in solid solution. Indeed, the increased strength of the T6I6 treatment over the more traditional T6 treatment is attributed to its ability to increase the total volume fraction of the strengthening precipitates [19].

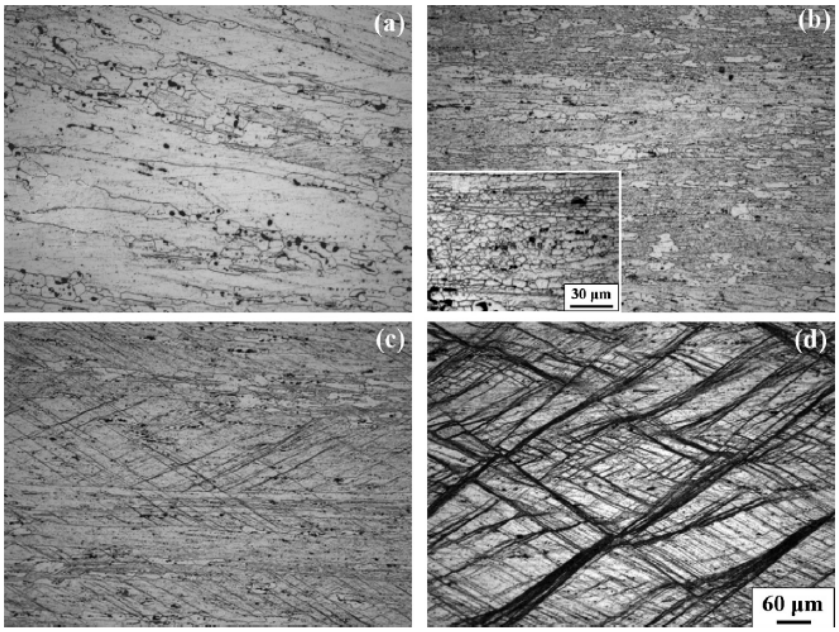

Figure 3.4: Optical microstructures of various samples from Figure 3.3 along the cold rolling direction. (a)T6, (b)CR5, (c) CR4, (d)CR2.

3.2 Fracture Toughness

Fracture toughness is a major design parameter in some high-strength aluminum alloys such as 7050, 7175, 7475, 7150, and others. It is most often measured through standard plane-strain pre-cracked fracture toughness tests, though it is also occasionally estimated by Kahn tear tests. Since the mechanisms that control fracture are thought to be similar to those that control the ductility, improvements in fracture toughness are sometimes estimated through relative changes in ductility.

As the strength decreases with continued over-aging it has generally been observed that the fracture toughness increases in 7xxx series alloys with a linear relationship, as shown in Figure 3.5 [20].

The fracture process is generally agreed to occur in three distinct phases in these alloys, including (1) void nucleation, (2) void growth, which is also considered to be

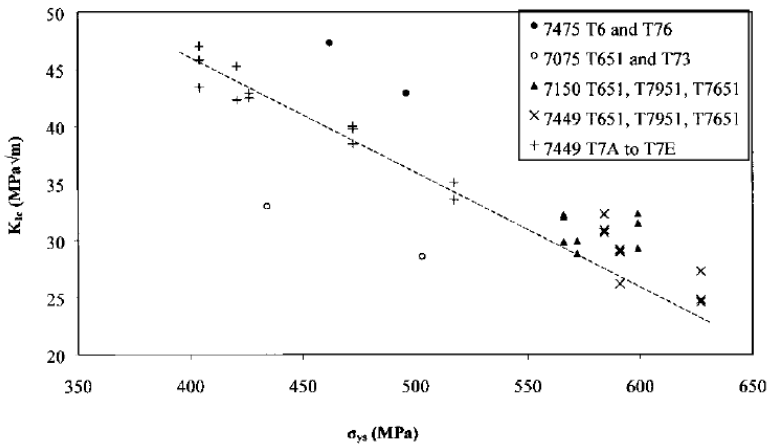

Figure 3.5: Toughness versus yield strength of various Al-Zn-Mg-Cu alloys.

ductile intergranular fracture since it usually occurs through the growth of voids nucleated near grain boundary regions, and (3) void coalescence, which either occurs by the coalescence of voids and the formation of a void sheet, or through the necking and subsequent failure of the remaining transgranular ligaments [17, 21, 22, 23, 24, 25]. Because of this transition from intergranular to transgranular fracture at different points of the process, it has been reported that the overall fracture toughness is controlled by this transition. Furthermore, the thought is that increasing the area fraction of transgranular fracture in the material will increase the overall toughness, since $K_{IC,transgranular} > K_{ICintergranular}$ [22, 23]. While in many cases this is true, it is misleading, since low-solute alloys in this series have been shown to exhibit primarily transgranular fracture, but still possess a much lower toughness than their high-solute counterparts [26]. A clearer perspective can be gained from considering that an increase in the overall toughness of the material will be gained by prolonging the void growth phase, or through delaying void coalescence [24, 25]. Examining the different fracture mechanisms in this way helps to explain some of the observations that have been made in the field.

3.2.1 Void Nucleation

During the first phase, void nucleation occurs through the cracking of coarse constituent particles (1-10 μm). These largest particles crack first, since the stress necessary to initiate particle cracking is inversely proportional to the square of the diameter, or $\sigma \propto D^{-1/2}$ [1, 24, 25]. The stress required for void nucleation can be even lower when these particles occur in clusters, as they often do, since these stringers can accumulate and trap dislocations very effectively [25]. This relationship between the volume fraction and size of coarse particles and the resulting fracture toughness is what first led to the development of high-purity alloys such as 7050, which showed a marked increase in toughness over 7075 [1, 27]. However, these constituent particles are not the only place that voids nucleation within the material. As the stress increases, voids are often formed at the dispersoids particles, usually about 0.1-1 μm in size [1, 21, 24, 27, 28, 29]. Therefore, it has also been proposed that decreasing the size and increasing the coherency of the dispersoids particles may help to increase the stress required for void nucleation, perhaps through the addition of Sc [24, 29, 30, 31, 32].

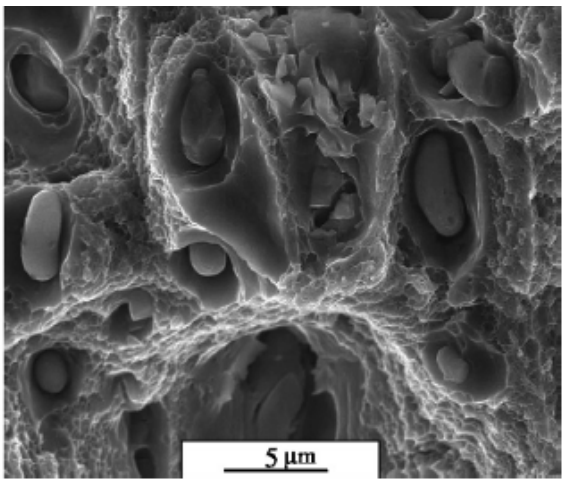

Figure 3.6: A fracture surface showing that the voids nucleated at constituent particles, which can be seen in the dimples of the surface.

3.2.2 Void Growth

Once nucleated, these voids grow through plastic deformation. As the strain increases, the growth of larger voids can happen concurrently with the nucleation and growth of smaller voids, such as the ones formed at dispersoids. Although the growth rate of voids that are the same size has been shown to be independent of the void spacing, this is not necessarily true when voids exist across multiple orders of magnitude. In this case, when small voids are located near the large voids, the growth rate of the small voids is significantly accelerated due to strain concentration effects [25]. This is important, since although constituent particles are often found in large recrystallized areas, their presence will still accelerate the growth rate of small voids formed on the grain boundary regions nearby [25, 29]. Decreasing the strain hardening ability or strain rate sensitivity can also increase the void growth rate [25]. Therefore, small grains can have an adverse effect on the toughness or ductility of the material [5, 6]. The amount of aging the material has undergone has also been shown to change the strain hardening capability of the material. When the material is under-aged, and the precipitates in the material are not fully formed, the strain hardening ability of the material is very high. However after peak or over-aging, this ability is significantly decreased. Therefore, it has been observed that an under-aged alloy will possess greater toughness than an over-aged alloy of the same strength [27].

If the grain interior is very strong compared the precipitate free zone (PFZ) area near the grain boundary, then void growth is halted, and any additional energy is dispersed in the material through void coalescence along the grain boundaries. This mechanism is responsible for the observed dependence of K_{IC} on the difference in

strength between the grain interior and the PFZ. This also explain the severe increase in the amount of intergranular fracture and the overall decrease in the fracture toughness with increase solute content in Al-Zn-Mg alloys [28]. The increasing solute content increases the volume fraction of strengthening particles in the grain interior, significantly increasing the strength and halting void growth. Therefore, the fracture surface goes from being largely transgranular, to occurring mainly through intergranular fracture and void coalescenece along the grain boundaries [25, 26, 28]. The linear tradeoff between yield strength and toughness described in Figure 3.5 can be explained through this mechanism. As aging progresses, the strength of the grain interior drops due to coarsening of the precipitates and the void growth stage increases, resulting in an increase in the fracture toughness of the alloy.

3.2.3 Void Coalescence

Once void growth is halted, the voids will begin to coalesce, and the material will fail. This process can occur either intergranularly through the formation of large void sheets, or transgranularly through the necking and failure of the remaining ligaments. The void distribution, while not observed to affect the growth rate, plays a dominant role in the onset of void coalescence [25]. It has been well observed that the area fraction of grain boundaries plays an important role in determining the overall fracture toughness of an alloy [22, 23, 28]. This is due to the acceleration of the void coalescence stage with an increasing areal fraction of the grain boundary, or a decreasing void distribution [25, 28].

There is also evidence that supports the theory that the η particles at the grain boundary facilitate this void coalescence, rather than playing a part in the direct nucleation and growth of voids. Since increasing the size and spacing of the η particles through over-aging or retrogression and re-aging serve to increase the overall

toughness of the material, rather than decrease it. In over-aged particles, the increase could be accounted for merely by the loss of strength in the grain interior due to the coarsening of strengthening precipitates. But after both retrogression and re-aging treatments and the interrupted treatments, the interior of the grain still possesses a high strength, but the fracture toughness is also greatly increased, perhaps due to a delay in the void coalescence [17, 20, 33, 34, 35, 36**?**].

3.3 Corrosion

Corrosion in aluminum alloys occurs locally in two ways: pitting and crevice corrosion, which is the result of a localized aggressive environment at a microstructure heterogeneity (such as an inclusion or a scratch) that breaks down the otherwise corrosion-resistant oxide that forms on the surface, and intergranular or exfoliation corrosion, which involves the formation of microgalvanic cells, usually at grain boundary regions with grain boundary precipitates often acting as an anode to a cathodic matrix in the surrounding region. Either of these mechanisms can manifest in one of three ways: (1) on their own in the form of localized or surface pitting corrosion, (2) in combination with some kind of contact force to cause mechanically-assisted degradation such as erosion, cavitation, or fretting corrosion, or (3) in the presence of a static tensile load (applied or residual) to cause environmentally assisted cracking through corrosion fatigue or stress corrosion cracking [37]. In high-strength aluminum alloys that are frequently utilized in aircraft components, stress corrosion cracking (SCC) susceptibility is a major concern. The two main mechanisms that govern SCC in these materials are anodic dissolution of precipitates along the grain boundary regions and hydrogen embrittlement [7, 18, 37, 38, 39, 40, 41].

3.3.1 SCC Testing

The tendency for a material to fail by stress corrosion cracking, or its stress corrosion cracking susceptibility, has been measured in a variety of ways. Since SCC

requires both a corrosive environment and a sustained tensile load, testing the SCC susceptibility of a material typically involves other familiar mechanical properties tests performed under a corrosive environment. Popular examples found in the literature include both smooth specimens, such as slow strain-rate or bent-beam tests, and notched or pre-cracked specimens, such as typical plane-strain fracture toughness testing to determine K_{ISCC}, the threshold stress intensity, or v_{pl}, the plateau crack velocity [7, 42, 43, 44, 45]. Because intergranular corrosion is typically responsible for SCC in 7xxx-series alloys of this type, some authors seek to compare SCC susceptibility across different alloys or microstructures by comparing their response to exposure corrosion or intergranular corrosion tests [46, 47]. However the most common type of test that is conducted in SCC susceptibility studies in these materials is potentiodynamic polarization testing. This method involves changing the potential across the electrolyte and measuring the resulting change in the current of the system, in which the material is acting as one electrode. By examining various changes in the current-potential curve, various types of information about the corrosion characteristics of the alloy can be determined [38, 43, 44, 46, 48, 49, 50].

However, it has been well observed that the presence of water vapor in the environment is required for hydrogen embrittlement effects to occur. It is unsurprising then, that the temperature and relative humidity of the environment will affect the overall corrosion characteristics of the material [37, 38, 40, 51]. Very similarly, the pH, type of electrolyte, and other aspects of the corrosive environment can also alter the corrosion behavior of the material being tested [37, 38]. It is therefore extremely difficult to compare results across different studies reported in the literature due to a difference in the environments used for testing.

3.3.2 Microstructure Effects on SCC Susceptibility

As discussed, SCC is environmentally assisted fracture, which requires both a corrosive environment and the application of an applied stress. Where typical fracture occurs in three steps consisting of void nucleation, growth, and coalescence, SCC consists of two distinct mechanisms: (1) pitting, which causes a stress concentration and allows for the formation of a crack, and (2) crack growth, which is often measured by the SCC plateau velocity. Pitting can increase the likelihood that a sharp crack in the surface of the material will be present. Once the stress concentration in this area reaches the threshold stress intensity, K_{ISCC}, the crack will begin to propagate. Since SCC is effectively accelerated intergranular fracture in the presence of a corrosive environment, it is unsurprising that many of the microstructure parameters that accelerate or affect the fracture toughness and ductility, also effect the SCC resistance.

Just as increasing the extent of recrystallization in the material will decrease the overall fracture toughness; increasing amounts of recrystallization will also increase the susceptibility of the material to SCC [7, 22, 38, 52]. This effect is the result of multiple mechanisms taking place within the microstructure. The first is that the breakdown potential, or the corrosion potential of the material, is inversely correlated with grain size, meaning that more coarse-grained materials promote intergranular corrosion [38, 52]. The second is that unrecrystallized sub-grain boundaries, and the Al_3Zr dispersoids that are often present at them, are very effective at trapping hydrogen, and therefore their presence can decrease the amount of hydrogen present in the grain boundary regions where SCC is most likely to occur [7, 18, 41]. Both of these mechanisms contribute to an increase in the SCC cracking plateau velocity with an increase in the extent of recrystallization.

Some constituent particles, such as Al_7Cu_2Fe, are cathodic with respect to the surrounding the matrix material and can dissolve the material around them through the formation of microgalvanic cells [50]. This decohesion between the particle and the matrix causes pitting, and therefore constituent particles play a role in initiating SCC through the formation of pits that is roughly equivalent to the role they play in void nucleation in the fracture and ductility processes.

It was also previously discussed that, although grain boundary particles do not play a role in void nucleation and growth, they are important in the facilitation of void coalescence. Therefore, increasing the size of these particles does not have a detrimental effect on the fracture toughness, and increasing the discrete spacing between them actually has a positive effect. Here, similarly increasing both the size and the spacing of these grain boundary precipitates increases both their ability to effectively trap hydrogen, and increases the amount of time it takes for them to anodically dissolve. This is part of the reason that increasing the size and discrete spacing can increase the SCC resistance as observed in T7, RRA, and T6I4 and T6I6 treatments [19, 46, 53, 54, 55, 56, 57].

However, changing the chemistry of the microgalvanic cell that is formed between the grain boundary precipitate and the surround PFZ can be more influential on the SCC resistance than changes in size and spacing. It is well known that increasing the amount of Cu in the grain boundary precipitate enobles the precipitate, or makes it less electrochemically active [7, 18, 39, 43, 48, 49, 58, 59]. The general thinking to date has been that because Cu has such a low corrosion potential, by incorporating Cu in to the grain boundary precipitate, the corrosion potential of the precipitate will also become lower or less electrochemically active. Much like other improvements in metallurgy, while the system responded as expected, it was not for the expected

reasons. Recently Birbilis and Buchheit did more thorough work on the corrosion potentials of various intermetallic phases in 7075 and showed that their tendency for dissolving and promoting intergranular corrosion was related, not to their corrosion potential (E_{corr}), but to the current density they were capable of sustaining at the corrosion potential of the overall material [49]. The corrosion potential and average current rates at both the corrosion potential of the intermetallic and the corrosion rate of 7075, are shown in Figure 3.7.

Stoichiometry	Phase	Corrosion potential (m V_{SCE})	Average free corrosion rate at corrosion potential (A/cm^2)	Average current at corrosion potential of AA7075-T651 (A/cm^2)
Mg (99.9)	-	−1586	5.5×10^{-6}	1.5×10^{-5}
Mg_2Si	β	−1538	7.7×10^{-6}	1.9×10^{-4}
$MgZn_2$	M, η	−1029	8.4×10^{-5}	1.0×10^{-3}
Mg_2Al_3	β	−1013	4.8×10^{-6}	1.9×10^{-5}
$Al_{32}Zn_{49}$	T′	−1004	1.4×10^{-5}	2.9×10^{-4}
Zn (99.99)	-	−1000	1.2×10^{-6}	8.1×10^{-5}
AA 7075-T651	-	−965	1.07×10^{-6}	-
Mg (AlCu)	-	−943	2.3×10^{-5}	-1.2×10^{-5}
Al_2CuMg	S	−883	2.0×10^{-6}	-2.1×10^{-6}
Al (99.9999)	-	−823	3.9×10^{-6}	-4.7×10^{-5}
$Al_{12}Mn_3Si$	-	−810	1.7×10^{-6}	-7.6×10^{-5}
7X75 Matrix	-	−799	3.2×10^{-6}	-8.1×10^{-5}
Al_6Mn	-	−779	6.3×10^{-6}	-1.2×10^{-4}
Al_3Zr	β	−776	2.5×10^{-6}	-8.1×10^{-5}
Al-2%Cu	α	−672	1.3×10^{-6}	-2.1×10^{-4}
Al_2Cu	θ	−665	7.3×10^{-6}	-4.7×10^{-4}
Al_3Ti	β	−603	5.6×10^{-7}	-2.7×10^{-4}
Al-4%Cu	α	−602	2.3×10^{-6}	-2.9×10^{-4}
$Al_{20}Cu_2Mn_3$	-	−565	3.4×10^{-7}	-1.9×10^{-5}
Al_7Cu_2Fe	-	−551	6.3×10^{-6}	-3.1×10^{-4}
Al_3Fe	β	−539	2.1×10^{-6}	-9.9×10^{-5}
Cu (99.9)	-	−232	1.8×10^{-6}	-1.8×10^{-3}

Figure 3.7: Electrochemical behavior of various intermetallics present in AA7075, as reported by Birbilis et al.[49]

It is the gradual transformation of the grain boundary precipitate from $MgZn_2$, which has a high average current and therefore a high driving force for dissolution, to a solid solution with increasing amounts of Mg(AlCu), which has a much smaller average current and a much lower driving force, that is really responsible for the increased resistance to SCC with increasing Cu in the grain boundary precipitates. It is also important to note that the presence of free Cu in the matrix can sustain a very high current density, even though it has a very noble corrosion potential. This may help explain some work which shows that while Cu in 1-2% amounts increases the SCC resistance, too much Cu can decrease it again [18]. Therefore, it is the way in which

Cu is incorporated in the material that plays a critical role in determining the corrosion. If Cu is left in solid solution rather than being thermodynamically driven in to the grain boundary precipitates, it will segregate towards the grain boundary and can electrochemically activate the material [49, 60].

Therefore, the addition of Cu to the alloy can affect the corrosion characteristics of the material in two different ways. The addition of Cu to the parent alloy has been shown to change the SCC plateau velocity by as many as 4 orders of magnitude [43, 59]. However, changing the Cu content locally within the grain boundary precipitate does not affect this velocity for a fixed alloy composition. Rather, increasing the Cu within the grain boundary decreases the metastable pitting rate (MPR), which helps to increase the overall SCC resistance [43].

In addition to changing the microchemistry of the precipitate, it is also possible to change the microchemistry of the other half of the microgalvanic cell, the precipitate free zone (PFZ). This is often overlooked compared to the precipitate chemistry, but just as important when it comes to changing the driving force. Its been observed that SCC susceptibility increases with an increasing amount of Mg segregation [61]. Changing the width of the PFZ can keep the level of Mg, as well as Zn and Cu more consistent closer to the grain boundary, which is important since Cu and Mg both tend to segregate towards grain boundaries, while Zn tends to segregate away [60, 61, 62]. For this reason, decreasing the width of the PFZ has historically been associated with an increased SCC resistance.

3.3.3 Potentiodynamic Polarization Curves

A lot of work has been done, particularly in the last decade, aimed at finding meaningful measurements derived from the potential-current curve that can be correlated with the corrosion potential. One study showed that a peak-aged material shows two breakdown potentials in the potential-current scan, but that an over-aged material only shows one [39]. It is thought that an increase between the two breakdown potentials represents an increase in the driving force for dissolution. Knight et al. and Goswami et al. both showed that the OCP of a freshly fractured surface correlates well with SCC plateau velocity, but as previously discussed Birbilis and Buchheit showed that E_{corr} is a misleading measurement when it comes to understanding the driving force for dissolution of various intermetallics [49, 58, 59]. Similarly, Gupta et al. did a thorough study in 7150 and 7079 which examined the effectiveness of different measurements derived from the polarization curve. They showed that E_{pit} is enobled 50mV with the addition of Cu, but that it is not a satisfactory parameter for evaluating pitting susceptibility, since it doesnt change with aging. As a result, both E_{pit} and $E_{pit} - \mathrm{OCP}$ are not good measures of the corrosion potential. They did find, however, that the metastable pitting rate (MPR) changed with a change in the precipitate size, even showing a critical size above which there was a marked change in the MPR [43]. Therefore it is likely that potentiodynamic polarization curves are extremely useful in revealing information about the pitting resistance and the SCC plateau crack growth velocity, but that this information is determined by separate measurements in the potential-current curve.

3.4 Summary

There are a wide variety of mechanical properties that might be of interest in high-strength Al-Zn-Mg-Cu alloys. Here the various microstructure parameters that control the tensile strength properties, the fracture toughness, and some of the corrosion behavior where all discussed. Other mechanical properties or performance characteristics such as fatigue properties or weldability could be also be discussed. However this work focused on properties that are more readily measured and may give indications as to the performance characteristics of the related properties. Understanding these linkages is critically important to the development of a visual process-structure-properties-performance map, which is the subject of Chapter 4.

3.5 References

[1] J. R. Davis, editor. *Aluminum and Aluminum Alloys*. ASM International, 1993.

[2] M. J. Starink and S. C. Wang. A model for the yield strength of overaged Al-Zn-Mg-Cu alloys. *Acta Materialia*, 51:5131–5150, 2003.

[3] A. Deschamps and Y. Brechet. Influence of predeformation and ageing of an Al-Zn-Mg alloy - ii. modeling of precipitation kinetics and yield stress. *Acta Materialia*, 47:293–305, 1999.

[4] N. Anjabin and A. Karimi Taheri. Physically based material model for evolution of stress-strain behavior of heat treatable aluminum alloys during solution heat treatment. *Materials and Design*, 31:433–437, 2010.

[5] R. Mahmudi. Grain boundary strengthening in a fine grained aluminum alloy. *Scripta Metallurgica*, 32:781–786, 1995.

[6] S. Zhang, W. Hu, R. Berghammer, and G. Gottstein. Microstructure evolution and deformation behavior of ultrafine-grained Al-Zn-Mg alloys with fine eta' precipitates. *Acta Materialia*, 58:6695–6705, 2010.

[7] X. Chen, Z. Liu, P. Xia, A. Ning, and S. Zeng. Transition of crack propagation from a transgranular to an intergranular path in an overaged Al-Zn-Mg-Cu alloy during cyclic loading. *Metallurgica Materiala International*, 19:197–203, 2013.

[8] W. M. Lee and M. A. Zikry. Modeling the interfacial plastic strain incompatibilities associated with dispersed particles in high strength aluminum alloys. *Acta Materialia*, 60:1669–1679, 2012.

[9] R. B. Nicholson, G. Thomas, and J. Nutting. The interaction of dislocations and precipitates. *Acta Metallurgica*, 8:172–176, 1959.

[10] David A. Porter, Kenneth E. Easterling, and Mohamed Y. Sherif. *Phase Transformation in Metals and Alloys*. CRC Press, 3rd edition edition, 2009.

[11] H. R. Shercliff and M. F. Ashby. A process model for age hardening of aluminum alloys - I. the model. *Acta Metallurgica Materelia*, 38:1789–1802, 1990.

[12] J. Chen, L. Zhen, S. Yang, W. Shao, and S. Dai. Investigation of precipitation behavior and related hardening in aa 7055 aluminum alloy. *Materials Science & Engineering, A: Structural Materials: Properties, Microstructure and Processing*, 500:34–42, 2009.

[13] S. P. Ringer and K. Hono. Microstructural evolution and age hardening in aluminum alloys: Atom probe field-ion microscopy and transmission electron microscopy studies. *Materials Characterization*, 44:101–131, 2000.

[14] D. Wang and Z. Y. Ma. Effect of pre-strain on microstructure and stress corrosion cracking of over-aged 7050 aluminum alloy. *Journal of Alloys and Compounds*, 469:445–450, 2009.

[15] D. Wang, Z. Y. Ma, and Z. M. Gao. Effects of severe cold rolling on tensile properties and stress corrosion cracking of 7050 aluminum alloy. *Materials Chemistry and Physics*, 117:228–233, 2009.

[16] J. Buha, R. N. Lumley, and A. G. Crosky. Secondary ageing in an aluminum alloy 7050. *Materials Science & Engineering, A: Structural Materials: Properties, Microstructure and Processing*, 492:1–10, 2008.

[17] N. M. Han, X. M. Zhang, S. D. Liu, B. Ke, and X. Xin. Effects of pre-stretching and ageing on the strength and fracture toughness of aluminum alloy 7050. *Materials Science & Engineering, A: Structural Materials: Properties, Microstructure and Processing*, 528:3714–3721, 2011.

[18] M. Dixit, R. S. Mishira, and K. K. Sankaran. Structure-property correlations in Al 7050 and Al 7055 high-strength aluminum alloys. *Materials Science and Engineering A*, 478:163–172, 2008.

[19] Jin-feng Li, Zhuo-Wei Peng, Chao-xing Li, Zhi-quang Jia, Wen-jing Chen, and Zi-qiao Zheng. Mechanical properties, corrosion behaviors and microstructures of 7075 aluminum alloy with various aging treatments. *Transactions of Nonferrous*

Metals Society of China, 18:755–762, 2008.

[20] N. Kamp, I. Sinclair, and M. J. Starink. Toughness-strength relations in the overaged 7449 Al-based alloy. *Metallurgical and Materials Transactions A: Physical Metallurgy and Materials Science*, 33A:1125–1136, 2002.

[21] Z. Cvijovic, M. Vratnica, and M. Rakin. Micromechanical modelling of fracture toughness in overaged 7000 alloy forgings. *Materials Science & Engineering, A: Structural Materials: Properties, Microstructure and Processing*, 434:339–346, 2006.

[22] N. U. Deshpande, A. M. Gokhale, D. K. Denzer, and John Liu. Relationship between fracture toughness, fracture path, and microstructure of 7050 aluminum alloy: Part I. quantitative characterization. *Metallurgical and Materials Transactions A: Physical Metallurgy and Materials Science*, 29A:1191–1201, 1998.

[23] A. M. Gokhale, N. U. Deshpande, D. K. Denzer, and John Liu. Relationship between fracture toughness, fracture path, and microstructure of 7050 aluminum alloy: Part II. multiple micromechanisms-based fracture toughness model. *Metallurgical Transactions A*, 29A:1203–1210, 1998.

[24] R. H. Van Stone and J. A. Perida. Discussion of "metallurgical factors affecting fracture toughness of aluminum alloys". *Metallurgical Transactions A*, 6A:668–670, 1975.

[25] T. Pardoen, F. Scheyvaerts, A. Simar, C. Tekoglu, and P. Onck. Multiscale modeling of ductile fracture in metallic alloys. *Comptes Rendus Physique*, 11: 326–345, 2010.

[26] T. H. Sanders and E. A. Starke. Relationship of microstructure to monotonic and cyclic straining of 2 age hardening aluminum alloys. *Metallurgical Transactions A*, 7:1407–1418, 1976.

[27] D. Dumont, A. Deschamps, and Y. Brechet. On the relationship between microstructure, strength and toughness in AA7050 aluminum alloy. *Materials Science & Engineering, A: Structural Materials: Properties, Microstructure and Processing*, 356:326–336, 2003.

[28] Gerard M. Ludtka and David E. Laughlin. The influence of microstructure and strength of the fractoughness and toughness of 7xxx series aluminum alloys. *Metallurgical Transactions A*, 13A:411–425, 1982.

[29] X. Zhang, W. Liu, S. Liu, and M. Zhou. Effect of processing parameters on quench sensitivity of an AA7050 sheet. *Materials Science & Engineering, A: Structural Materials: Properties, Microstructure and Processing*, 528:795–802, 2011.

[30] M. Bobby Kannan and V. S. Raja. Enhancing stress corrosion cracking resistance in Al-Zn-Mg-Cu-Zr alloy through inhibiting recrystallization. *Engineering Fracture Mechanics*, 77:249–256, 2010.

[31] L. M. Wu, W. H. Wang, Y. F. Hsu, and S. Trong. Effects of microstructure on the mechanical properties and stress corrosion cracking of an Al-Zn-Sc-Zr alloy by various temper treatments. *Materials Transactions*, 48:600–609, 2007.

[32] Y. W. Riddle and T. H. Sanders. A study of coarsening, recrystallization, and morphology of microstructure in Al-Sc-(Zr)-(Mg) alloys. *Metallurgical and Materials Transactions A: Physical Metallurgy and Materials Science*, 35A:341–350, 2004.

[33] R. N. Lumley, I. J. Polmear, and A. J. Morton. Control of secondary precipitation to improve the performance of aluminum alloys. *Materials Science Forum*, 396-402:893–898, 2002.

[34] R. N. Lumley, I. J. Polmear, and A. J. Morton. Development of properties during secondary ageing of aluminum alloys. *Materials Science Forum*, 426-432: 303–308, 2003.

[35] R. N. Lumley, I. J. Polmear, and A. J. Morton. Interrupted aging and secondary precipitation in aluminum alloys. *Materials Science and Technology*, 19:1483–1492, 2003.

[36] R. N. Lumley, I. J. Polmear, and A. J. Morton. Development of mechanical properties during secondary aging in aluminum alloys. *Materials Science and Technology*, 21:1025–1033, 2005.

[37] J. R. Davis, editor. *Corrosion of Aluminum and Aluminum Alloys*. ASM Internation, 1999.

[38] Amjad Saleh El-Amoush. Intergranular corrosion behavior of the 7075-T6 aluminum alloy under different annealing conditions. *Materials Chemistry and Physics*, 126:607–613, 2011.

[39] T. Ramgopal, P. I. Gouma, and G. S. Frankel. Role of grain-boundary precipitates and solute-depleted zone on the intergranular corrosion of aluminum alloys 7150. *Corrosion*, 58:687–697, 2002.

[40] H. Vogt and M. O. Speidel. Stress corrosion cracking of two aluminum alloys: A comparison between experimental observations and data based on modeling. *Corrosion Science*, 40:251–270, 1998.

[41] J. D. Robson and P. B. Prangnell. Dispersiod precipitation and process modelling

in zirconium containing commercial aluminum alloys. *Acta Materialia*, 49:599–613, 2001.

[42] G. SIlva, B. Rivolta, R. Gerosa, and U. Derudi. Study of new heat treatment parameters for increasing mechanical strength and stress corrosion cracking resistance of 7075 aluminum alloy. *La Metallurgia Italiana*, 3:21–24, 2012.

[43] R. K. Gupta, A. Deschamps, M. K. Cavanaugh, S. P. Lynch, and N. Birbilis. Relating the early evolution of microstructure with the electrochemical response and mechanical performance of a Cu-rich and Cu-lean 7xxx aluminum alloy. *Journal of The Electrochemical Society*, 159:492–502, 2012.

[44] M. Puiggali, A. Zielinkski, J. M. Olive, E. Renauld, D. Desjardins, and M. Cid. Effect of microstructure on stress corrosion cracking of an Al-Zn-Mg-Cu alloy. *Corrosion Science*, 40:805–819, 1998.

[45] R. K. Singh Raman, R. Rihan, and R. N. Ibrahim. Validation of a novel approach to determination of threshold for stress corrosion cracking. *Materials Science & Engineering, A: Structural Materials: Properties, Microstructure and Processing*, 452-453:652–656, 2007.

[46] Z. Li, B. Xiong, Y. Zhang, B. Zhu, F. Wang, and H. Liu. Investigation on strength, toughness and microstructure of an Al-Zn-Mg-Cu alloy. *Journal of Materials Processing Technology*, 209:2021–2027, 2009.

[47] J. Wloka, T. Hack, and S. Virtanen. Influence of temper and surface condition on the exfoliation behaviour of high strength Al-Zn-Mg-Cu alloys. *Corrosion Science*, 49:1437–1449, 2007.

[48] N. Birbilis, M. K. Cavanaugh, R. G. Buchheit, D. G. Harlow, and R. P. Wei. Understanding damage accumulation upon aa7075-T651 used in airframes from a microstructural point of view. *Materials Science and Technology*, 1:57–68, 2005.

[49] N. Birbilis and R. G. Buchheit. Electrochemical characteristics of intermetallic phases in aluminum alloys. *Journal of the Electrochemical Society*, 152:B140–B151, 2005.

[50] N. Birbilis, M. K. Cavanaugh, and R. G. Buchheit. Electrochemical behavior and localized corrosion associated with Al7Cu2Fe particles in aluminum alloy 7075-T651. *Corrosion Science*, 48:4202–4215, 2006.

[51] James T. Burns and Richard P. Gangloff. Effect of low temperature on fatigue crack formation and microstructure-scale growth from corrosion damage in Al-Zn-Mg-Cu. *Metallurgical and Materials Transactions A: Physical Metallurgy and Materials Science*, 44A:2083–2105, 2013.

[52] X. Fan, D. Jing, L. Zhong, T. Wang, and S. Ren. Influence of microstructure on the crack propagation and corrosion resistance of Al-Zn-Mg-Cu alloy 7150. *Materials Characterization*, 58:24–28, 2007.

[53] J. Beddoes. Design of solution heat treatments for aerospace alloys. *Canadian Metallurgical Quarterly*, 3:215–221, 50.

[54] J. K. Park and A. J. Ardell. Microchemical analysis of precipitate free zones in 7075-al in the T6, T7, and RRA tempers. *Acta Metallurgica*, 39:591–598, 1991.

[55] A. Karaaslan, I. Kaya, and H. Atapek. Effect of aging temperature and of retrogression treatment time on the microstructure and mechanical properties of alloy AA7075. *Metal Science and Heat Treatment*, 49:443–447, 2007.

[56] F. Viana, A. M. P. Pinto, H. M. C. Santos, and A. B. Lopes. Retrogression and re-ageing of 7075 aluminum alloy: Microstructural characterization. *Journal of Materials Processing Technology*, 92-93:54–59, 1999.

[57] A. F. Oliveira, M. C. de Barros, K. R. Cardoso, and D. N. Travessa. The effect of RRA on the strength and SCC resistance on AA7050 and AA7150 aluminum alloys. *Materials Science & Engineering, A: Structural Materials: Properties, Microstructure and Processing*, 379:321–326, 2004.

[58] R. Goswami, S. Lunch, N. J. H. Holroyd, S. P. Knight, and R. L. Holtz. Evolution of grain boundary precipitates in al 7075 upon aging and correlation with stress corrosion cracking behavior. *Metallurgical and Materials Transactions A: Physical Metallurgy and Materials Science*, 44A:1268–1278, 2013.

[59] S. P. Knight, N. Birbilis, B. C. Muddle, A. R. Trueman, and S. P. Lynch. Correlations between intergranular stress corrosion cracking, grain-boundary microchemistry, and grain-boundary electrochemistry for Al-Zn-Mg-Cu alloys. *Corrosion Science*, 52:4073–4080, 2010.

[60] G. Sha, L. Yao, X. Liao, S. P. Ringer, Z. C. Duan, and T. G. Langdon. Segregation of solute elements at grain boundaries in an ultrafine grained Al-Zn-Mg-Cu alloy. *Ultramicroscopy*, 111:500–505, 2011.

[61] R. G. Song, W. Dietzel, B. L. Zhang, W. J. Liu, M. K. Tseng, and A. Atrens. Stress corrosion cracking and hydrogen embrittlement of an Al-Zn-Mg-Cu alloy. *Acta Materialia*, 52:4727–2743, 2004.

[62] T. Marlaud, A. Deschamps, F. Bley, W. Lefebre, and B. Baroux. Influence of alloy composition and heat treatment on precipitate composition in Al-Zn-Mg-Cu alloys. *Acta Materialia*, 58:248–260, 2010.

CHAPTER 4

THE PROCESS-STRUCTURE-PROPERTIES-PERFORMANCE MAP

In 2011, the White House announced the Materials Genome Initiative (MGI), which is based on the idea that advanced materials systems are foundational and transformative technologies. One of the major goals of the MGI is to encourage researchers to integrate experimental test methods, computational tools, and known knowledge databases to find ways to decrease the time and cost the currently goes in to discovering, developing, and optimizing a material system for deployment in a commercial system[1].

One of the potential applications for this kind of integration is in the development and property optimization stage of material development. These stages are often cost and time consuming, largely because of the strong reliance in materials research and development on scientific intuition and trial and error experimentation. Much of the design and testing of new materials systems is currently performed through time-consuming and repetitive experiment and characterization loops. However, once enough experimental work has been done to develop the material system, including understanding the chemical and physical mechanisms that drive the process-structure-property-performance relationships, then computational tools can be used to more quickly and efficiently work towards optimization.

While the potential for computational tools to assist with property optimization is

not a new concept, it is surprising that more accurate computational models are not used in many materials systems which could benefit from them. On closer examination, there are still two key issues that are limiting the development and integration of these tools. The first, is that there is currently no standard method to communication critical information about the material system from those who develop the system, to those who are interested in modeling it, and beyond. Oftentimes these materials systems are developed by people with a deep knowledge of the system in question, but the computational models are developed by people with a deep knowledge of computational modeling, and who are usually new to the material system they are working in. Therefore, it is critical that a standard exists to communication information about the mechanisms driving the system. The second key issue is that there is often a lack of understanding about what information must be obtained to accurately describe the material system in its entirety. Having a standard method of communicating the physical and chemical mechanisms which drive the system could be useful in resolving this issue as well. This work focuses on developing process-structure-property-performance (PSPP) maps as this missing standard communication method. Here we detail the steps that should be taken to generate a map for any system, and then briefly discuss how those steps were applied to high-strength age-hardened Al-Zn-Mg-Cu alloys. These alloys are typically utilized in aircraft applications and are extremely complicated and commercially viable materials which are repeatedly subject to re-optimization, and are thus a good example of the value of these PSPP maps and how they can be used.

4.1 Generating a PSPP Map

Process-Structure-Property-Performance maps as they are described here are meant to be a standard method of communication for the physical and chemical mechanisms that are involved in the system, as well as the data or information required to fully

characterize it. Here, we lay out some general guidelines for how to make these maps for any materials system.

When developing a PSPP map for a material, it is important to consider how developed the materials system is. Although the method detailed here is flexible enough to account for both more established systems as well as newer materials that are still in development, the overall process or result may be altered depending on how much is currently known about the mechanisms that drive the system being mapped. Just as the development of a materials system is an inherently iterative process, the mapping of the system will also be iterative, with new maps being developed as new information becomes available. Since these maps are meant to serve as an allegorical tool and help researchers and modelers navigate these often complex and interconnected materials systems, it is unsurprising that they share many of the same characteristics observed in geographical maps. Although the underlying relationships that govern a material system to do not change depending on the application, it is possible that maps with various levels of specificity may exist for different applications or defined materials spaces. Much like geographical maps, PSPP maps are visual standards, but can be customized depending on the features of interest and the level of detail or total size required.

Given the various levels of specificity that are available, an important aspect to consider when building a PSPP map for a material system is the scope, or total size, of the materials design space that is desired. As a general guideline, maps should be large enough to capture all of the features, processing options, or properties of interest, but specific enough to be useful to the application or project they are built for. Ultimately, the scope and level of detail that is captured in the Structure column will set the space.

Even though the Structure column is pivotal to defining the space included in the map, it is not considered the best place to begin the mapping process. Rather, users who are interested in developing a new map should start with the Process and Properties columns as a first step, as shown in Figure 4.1. Under the Properties column, the user should begin by listing the various properties of interest. If the user has a particular set of Performance metrics, sometimes called a performance profile, these may be useful in determining what properties need to be included in the map. It is recommended that the properties initially be listed and boxed individually as much as possible. After the first iteration of the map has been detailed, properties that share similar driving mechanisms can be grouped for convenience if desired.

Under the Process column, it is recommended that the user begin by listing all of the available or currently known processing steps involved in the production of the material defined by the system. Each processing step should be boxed, and within each box the variable parameters involved in that step can be listed and grouped together (e.g. a box containing the Annealing step might include variable parameters such as annealing time and annealing temperature). When the processing route being detailed contains two possible steps that are mutually exclusive, they must either be redefined so that they can be included together in one box, or one must be discarded and the system being mapped will be constrained (e.g. a metal alloy which may be either extruded or hot-rolled can have either a boxed step labeled Extrusion, a boxed step labeled Hot-Rolling, or these two processing steps could be simultaneously combined in a more general boxed step labeled Plastic Deformation). The Process column should generally consist of a set of linear steps that constitute the entire processing route. However, other parameters, such as the parent composition of the material,

can also be included. Ultimately, the Process column should contain all directly controllable parameters involved in the making of the material being characterized.

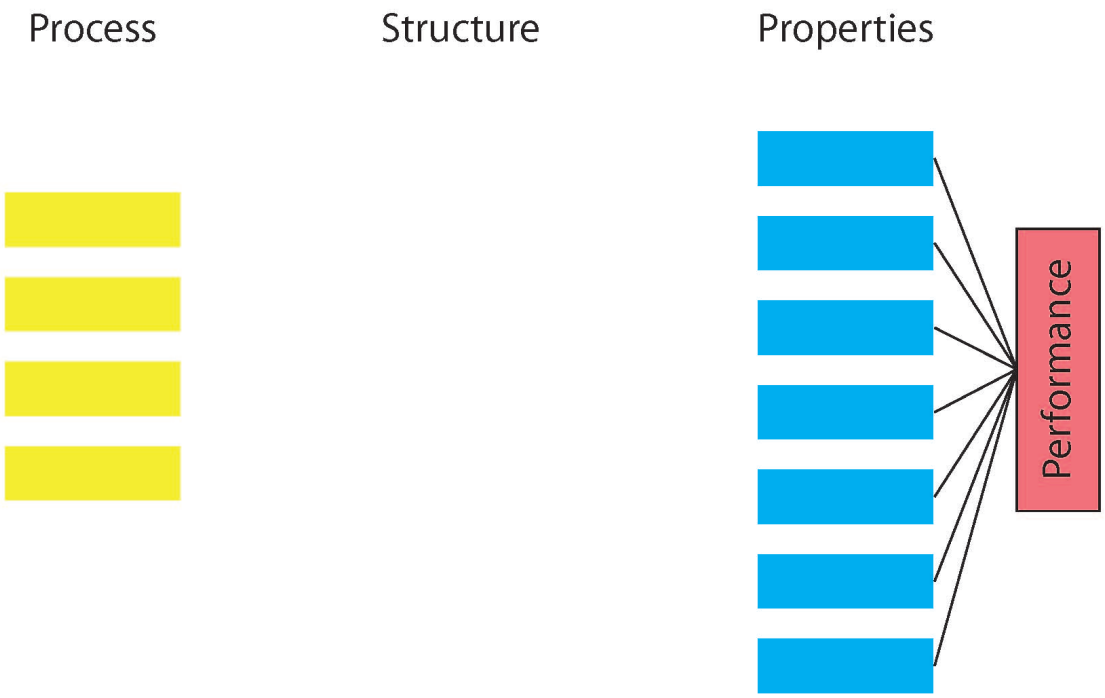

Figure 4.1: The user should begin the mapping process by generating all the necessary boxes contained in the Process and Properties columns.

Once the Process and Properties columns have been detailed, the various structural features of the material, which are indirectly controlled through the processing, can be generated. To do this, the user should begin by examining the elements listed in the Process column and, using what is already known about the material, generate a list of structural features that are influenced by the different processing parameters, as illustrated in Figure 4.2. The structural features can be boxed either individually or in relevant groupings depending on the level of detail that is desired. Recall that the scope and detail of the Structure column will ultimately define the design space encompassed. Similar to the Properties column, if the user is unsure of which structural elements would be well suited to grouping, it is best to leave them boxed individually

until the first iteration of the map has been detailed. Afterwards, structural features that are of similar length scales and have similar effects on the properties may be considered for grouping.

Once the structural elements have been boxed, it is important to map the relationships between the two columns, as demonstrated in Figure 4.2. If a relationship between an element in a processing box and an element in a structural box is known, indicate this relationship by connecting the boxes with a solid line. If a relationship is expected, but not confirmed, use a dashed line. The presence of a dashed line is useful to indicate that a relationship between these boxes is expected, but that further work must be done by the materials science community in order to confirm the presence or absence of this relationship. It is important that the lack of a line connecting two boxes indicates that the two elements in question have been confirmed to not share a relationship. Therefore, if the effect of a processing step on the various structure elements is not fully or adequately known, indicate this by dashing the processing box in question. Even if the processing step in question does have some confirmed or expected relationships, this can still be a useful way to indicate to the community that this step may have effects on the structure that are not fully understood. As a point of clarification, while the presence of a solid line should indicate that there is an influence of a processing box on an associated structure box, it is not an indication that the exact relationship is known. Even in situations where the two parameters are known to be, for example, linearly or inversely related, this information should not necessarily be indicated as a part of this map.

Once the relationships between the Process column and the Structure column have been mapped, similar steps can be taken to map the Structure column to the Properties column. Here, the user should generate a second list of structural features that

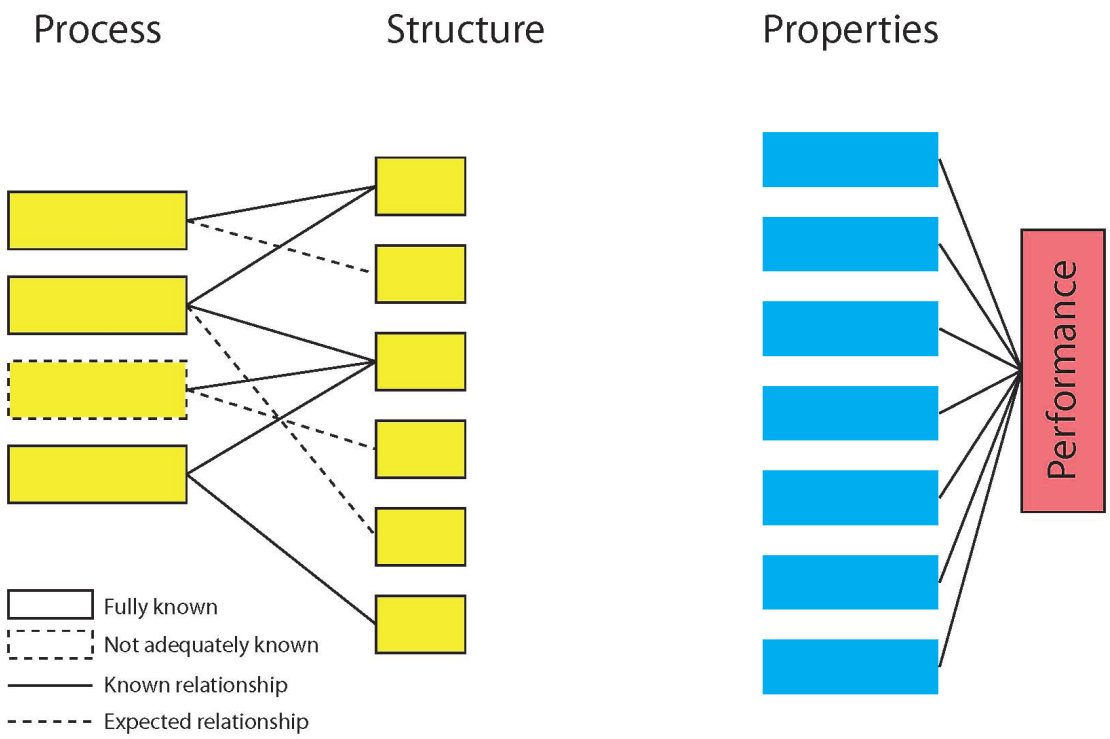

Figure 4.2: The known and expected relationships between the processing parameters and the structural features should be indicated by a series of solid or dashed lines and boxes.

drive or affect the properties that are listed under the Properties column, as shown in Figure 4.3. Once again, if the features that drive a property are unknown or not fully explored, this should be indicated by dashing the box containing that property, as shown in Figure 3.

At this point, it is possible that one or more property boxes may be unconnected to the rest of the map because it is unknown what those relationships with the various structural elements may be. However, if a property box is floating and is contained by a solid box, this is an indication that either (1) the user has not included all of the necessary structural elements required to characterize the material, or (2) that the property in question is not a true property. For example, yield strength, electrical conductivity, and density are all material properties, which are dictated only by the

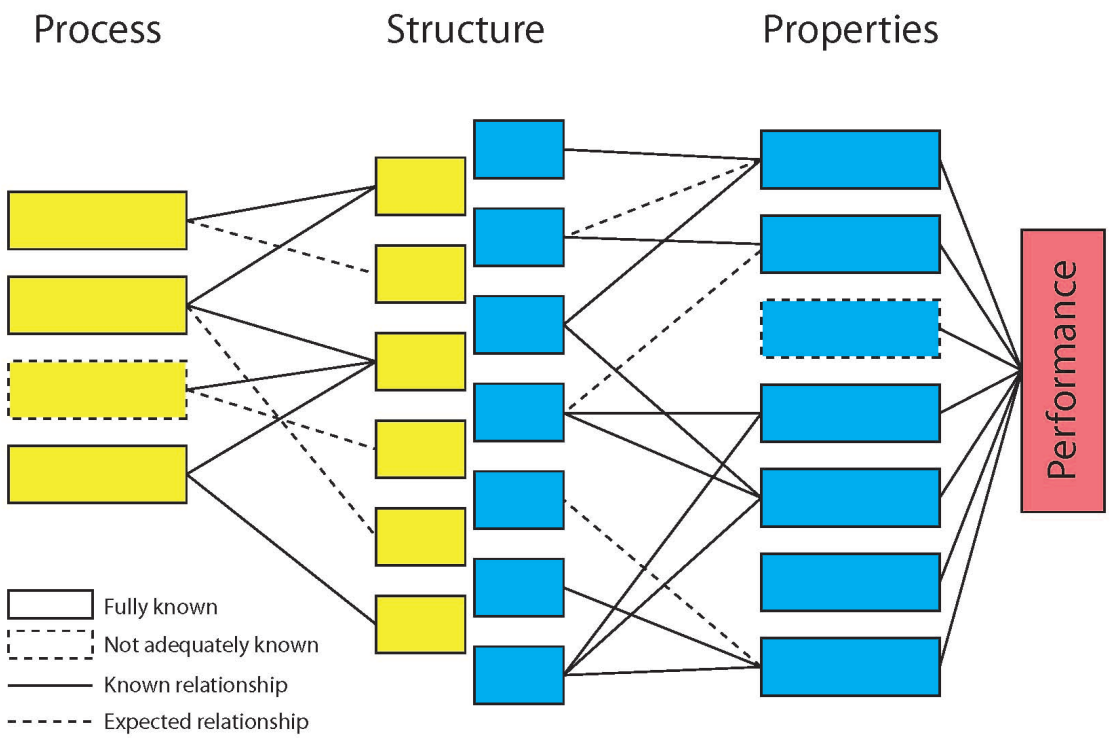

Figure 4.3: The known or expected relationships between the properties and the structural features that drive them should be indicated with alternatively solid or dashed lines. If the features that drive a property are unknown, this should be indicated with a dashed box around the property in question.

structure of the material. Cost, however, which is driven by many factors not captured in the map, is not a true material property and should not be included in this column.

Once these two sets of relationships have been mapped, and any misidentified properties have been resolved, the user can proceed with merging the two independently generated Structure lists, as illustrated in Figure 4.4. Here, if a box appears in one list, but not the other, then dash one half of the box to indicate that the relationship between this feature and the opposite column is potentially unknown. It is also possible that, since the structure is indirectly controlled through one or more elements listed under the Process column, while one set of processing parameters may have been identified to affect the feature, others are still thought to be missing. Since this

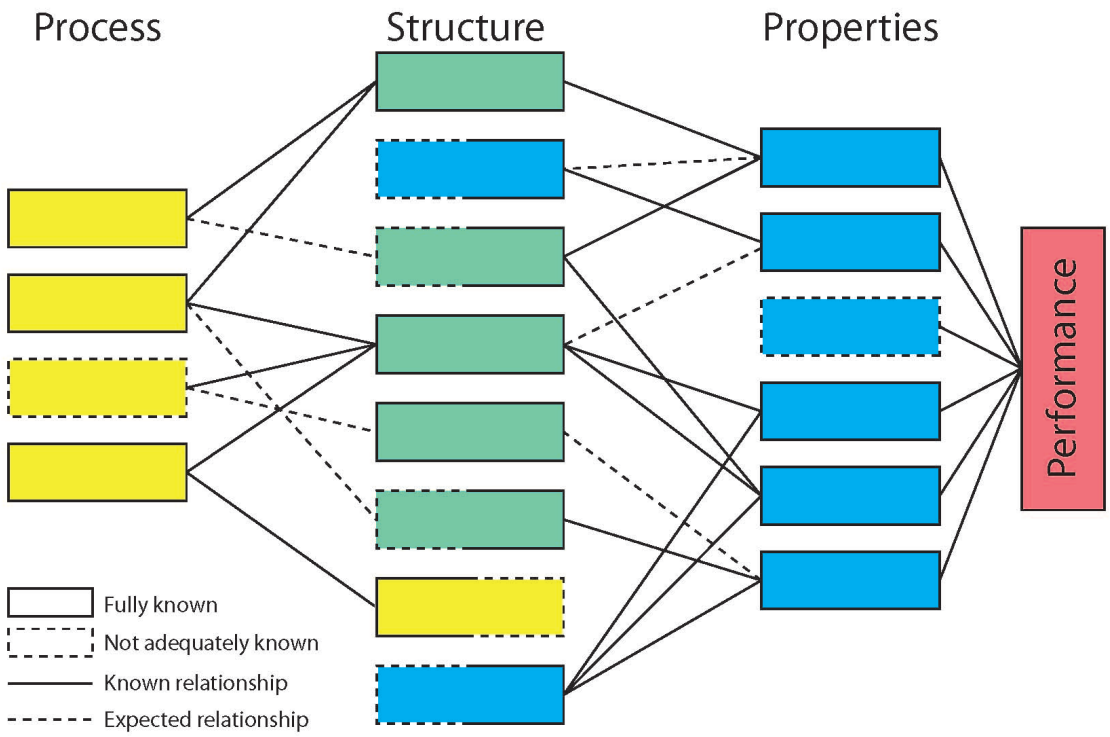

Figure 4.4: The two structure lists that were generated, should be merged. If the relationship between a structural feature and either the Process or Properties column is not fully known, this should be indicated by half of a dashed box, as shown here.

is an indication that more work needs to be done by the community in this area, this would again be indicated by a half dashed box.

For boxes that appeared in only one of the two Structure lists, as shown in Figure 4.5, these half-dashed boxes should be solidified if and only if it is established that no relationship is missing between the feature in question and the opposite column. If a solidly boxed element in the Structure column is not connected to anything in the Property column, then it is likely an indication that the structural feature in question, while indirectly controllable by the processing steps, is extraneous to the material system as it has been currently defined. Unless it is likely to be linked to a property of interest at some point in the future, it is suggested that it be removed from the map.

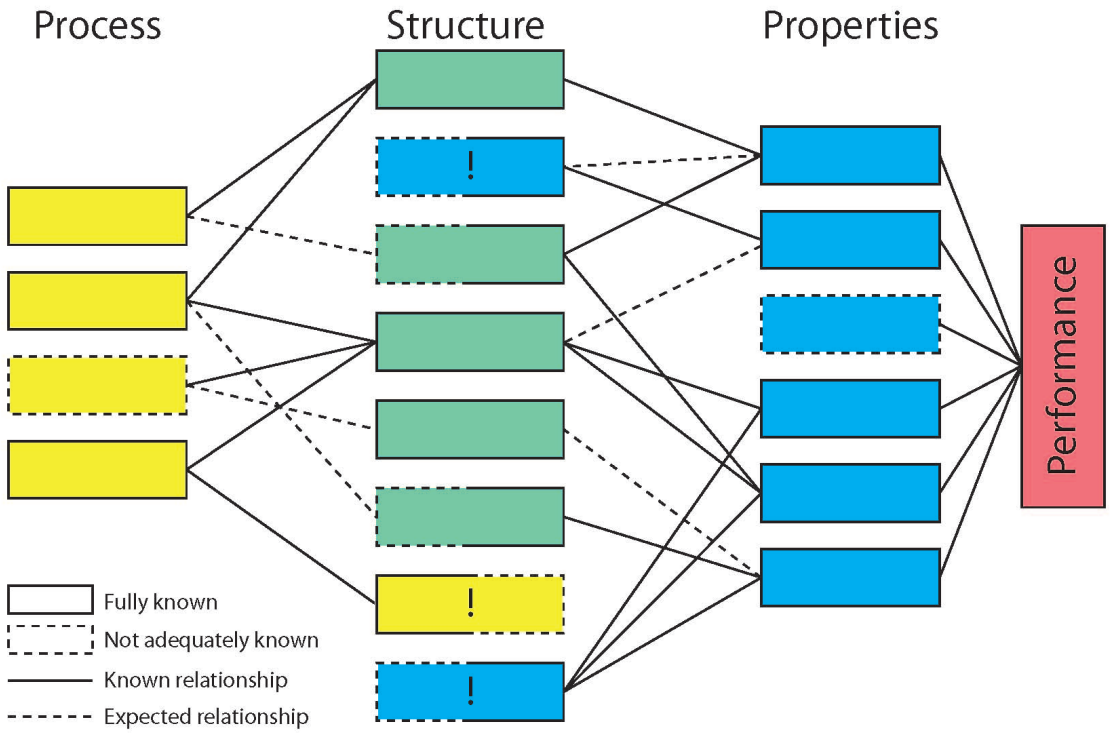

Figure 4.5: If and only if it is established that no relationship is missing between the feature in question and the opposite column, should a half dashed Structure box be replaced with a fully solid one.

If a solidly boxed element in the Structure column is not linked to the Process column, as shown in Figure 4.6, then this is an indication that the processing step or steps that control this feature are not included in the existing processing list and it is therefore incomplete. If the processing step that controls the feature in question cannot be added to the map, perhaps because it is not known, then it is still possible to use the map to characterize the material system. But to do so, it will be critical to measure the structural feature in question, since it cannot be indirectly measured by controlling the processing steps that drive it. This information should be communicated on the map by double boxing the structural feature in question, as demonstrated in Figure 4.7.

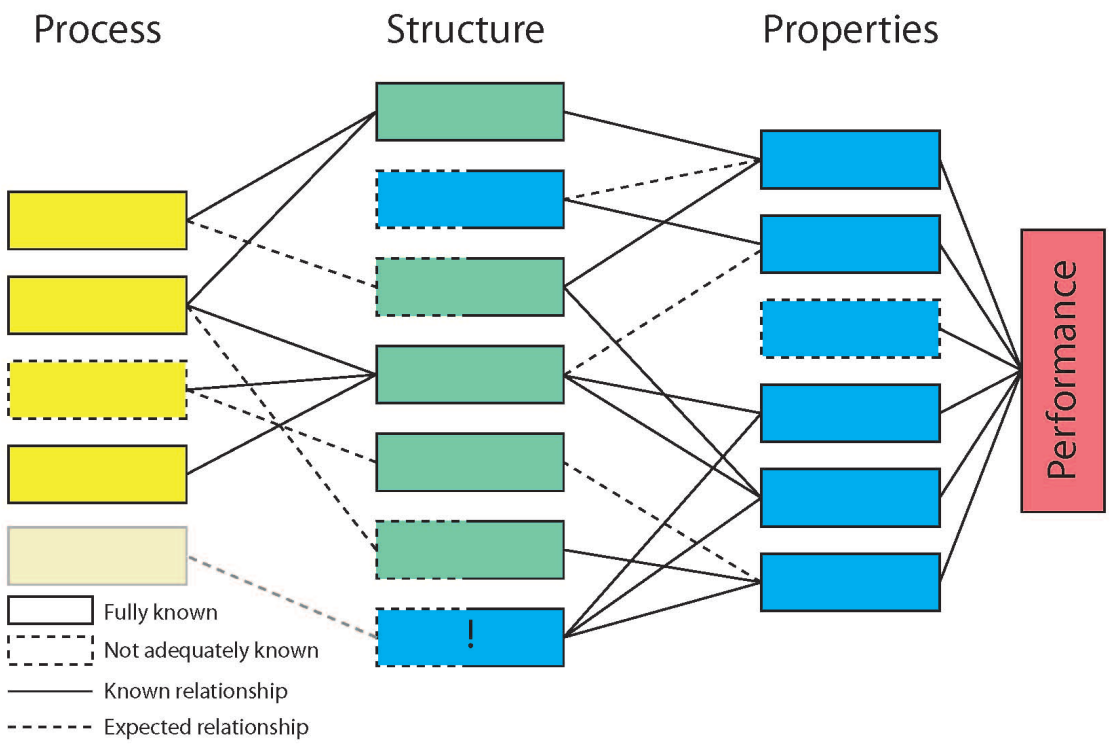

Figure 4.6: If a solidly boxed structural feature is not connected to an element in the Process column, then it is an indication that the directly controllable processing steps listed are incomplete.

Once all of the known and unexplored relationships are indicated on the map by following the above steps, the first iteration of the map should be complete. At this point, if the user is unsatisfied with the size of the materials design space that has been defined, or with the level of detail included in the map, they can iterate through the steps detailed above: adding, combining, or dividing boxes as necessary until the desired level of specificity is obtained. Additionally, once the map has been detailed, targeted exploration can be used to solidify those unconfirmed relationships as indicated by dashed lines and boxes.

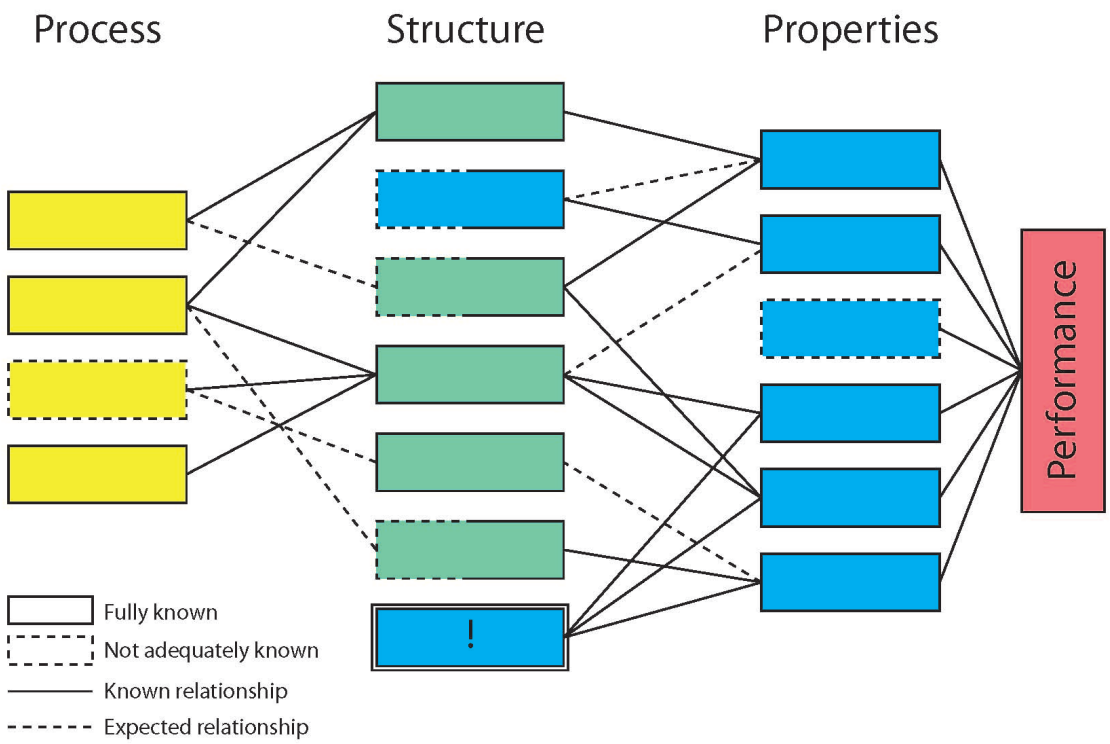

Figure 4.7: If the directly controllable processing step that drives the floating structural feature in question cannot be included, perhaps because it is unknown, then this information must be included by double boxing the structural feature.

4.2 Generating a PSPP Map for the Al-Zn-Mg-Cu System

Now that some general guidelines for how to make these maps for any materials system have been detailed, these steps can be used to create a PSPP map for high-strength age-hardened Al-Zn-Mg-Cu alloys used in aircraft components. This class of Al-Zn-Mg-Cu alloys, which includes AA7075, AA7050, AA7055, AA7079, AA7449, and many others, has been used in aircraft applications for over 75 years and is well established in the industry. Because these alloys are constantly being developed to provide a wide range of performance profiles for specific applications, they are continually developed. However, the extremely complex relationships that exist between the many processing routes, the complicated microstructural features that extend over multiple length scales, and the variety of properties of interest, make property

optimization through computational modeling techniques challenging. In fact, many of these relationships cannot currently be predicted computationally with any real accuracy in this system, even after 75+ years of development[2]. Some initial successes, however, have been made in this space such as relationships which predict yield strength as a function of a variety of microstructural features[2, 3, 4, 5]. The next step in this materials system is to enable the modeling of multiple elements within this space, possibly through machine learning methods such as artificial neural networks or other multivariable regression methods. To do this successfully, a PSPP map for this alloy system must first be developed. Here the authors have used Al-Zn-Mg-Cu alloys as an example to illustrate the steps used to create the map.

4.2.1 Processing Steps and Properties of Interest

One advantage of this material class is that it has been well studied. As a result, the processing steps and their variable parameters, as well as the effect of changing those parameters on the microstructure are well established. Industrially in these systems, the material is first solidified through direct chill casting methods before being homogenized[6]. While this class of aircraft aluminum alloys is not commonly forged, they are regularly extruded or hot-rolled into stock pieces such as plates, sheets, and bars depending on the application[6]. Since material can only be extruded or hot-rolled, but not both, these steps are contained in one box titled Plastic Deformation. After they are formed into stock pieces, they are typically solution heat treated, quenched, and aged. Occasionally, they can be pre-strained or cold-rolled for stress-relief or to increase the dislocation density prior to aging[7]. These steps and their key parameters are shown in Figure 4.8.

Although many properties are typically of interest in this material system, the most commonly optimized and developed properties are the yield and ultimate strength,

the work hardenability, the ductility, fracture toughness, and the stress corrosion cracking susceptibility. Other properties such as exfoliation corrosion resistance, fatigue strength, or density could also be included, and the performance profile is left general.

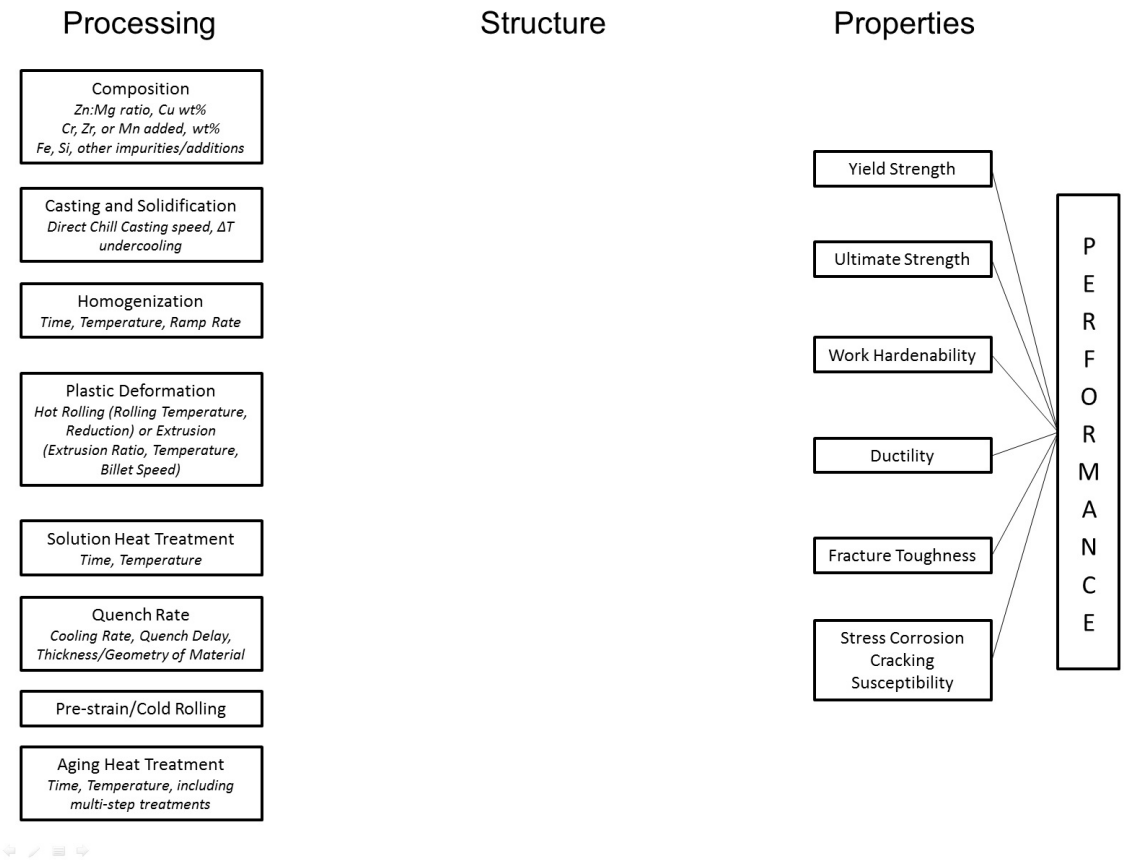

Figure 4.8: The processing steps involved in making high-strength Al-Zn-Mg-Cu alloys, and some of the most common properties of interest in developing materials for aircraft.

4.2.2 Process-Structure Relationships

Now it is necessary to identify the influence each of the processing steps listed in Figure 4.8 has on the structure of the material. These structural elements are then grouped and listed in Figure 4.9. Since the material is formed through direct chill

(DC) casting, both the casting speed and the degree of undercooling are important and can affect the solidification kinetics[6, 7, 8]. Similar to gravity cast systems, semi-continuous casting methods such as DC casting form regions of columnar dendritic growth near the walls of the container, with more equiaxed structures appearing in the middle of the cast. The as-cast material is highly cored with intermetallics in the interdendritic regions[8]. Changing the parameters during this step can affect the solidification kinetics of the casting process, which can lead to changes in the grain size and the size, spacing, and volume fraction of the resulting constituent particles.

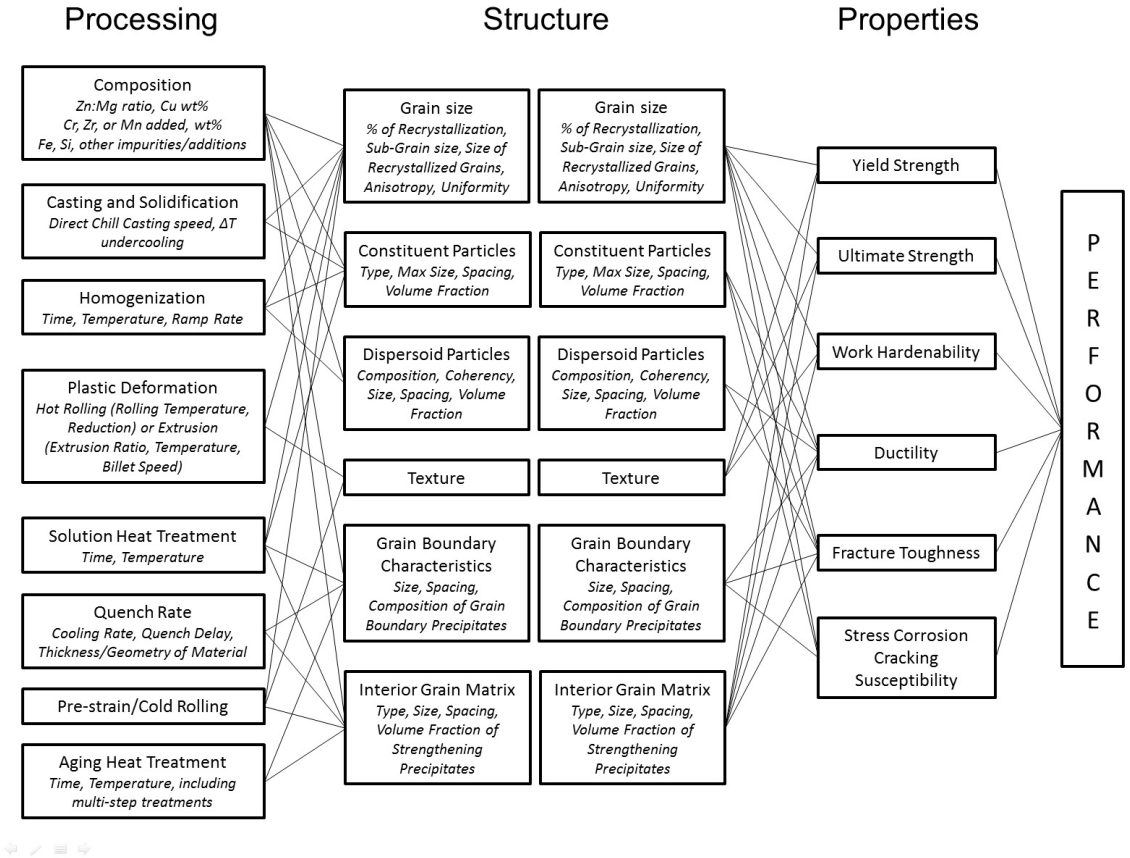

Figure 4.9: The known or expected relationships between the processing steps and the structural features the influence, as well as the properties and the structural features that drive them are shown here. Since this material system is well developed, no dashed lines or boxes are required.

Other directly controllable parameters used during this step include additions of Al-Ti-B refiners to change the grain size[6, 7, 9]. However, care must be taken since small excess amounts of boron can lead to constituent particles, which have detrimental effects on many properties including fracture toughness, machinability, and appearance[9]. Cr, Zr, and less often Mn are also added as dispersoid forming elements when the material is formed. The dispersoid particles that are formed using these elements are added to inhibit the recrystallization of the material, but sometimes these additions can form large primary particles during casting instead leading to more constituent particles throughout the material[6, 7, 9].

Once the material is cast it is typically homogenized, by heating the material to an elevated temperature for an extended period of time[6, 7, 10]. The homogenization serves multiple purposes. In addition to redistributing the Zn, Mg, and Cu required to form well dispersed strengthening and grain boundary precipitates, it also serves to redistribute and optimize the precipitation of the Cr- or Zr-containing dispersoid elements which are intended to inhibit recrystallization[6, 7, 9, 10]. The elevated temperature is also used to try and melt as many of the coarse constituent particles as possible. However, care must be taken in setting the homogenization temperature, since many of these constituent particles have relatively low melting temperatures[7, 10]. As a result, the time, temperature, and the heating ramp rate, can all affect the dispersion of constituent and dispersoid particles, as well as indirectly affecting the extent of recrystallization through the formation and optimization of the dispersoid particles.

The controllable parameters during the plastic deformation step are obviously different depending on whether the material is hot-rolled or extruded. Regardless, this step is known to have significant effects on the final microstructure, including the

texture, the grain characteristics, and the uniformity of the grain characteristics throughout the component[6, 7]. Even though this material does not dynamically recrystallize, but rather statically recrystallizes during the solution heat treatment, this step does affect the extent of recrystallization[7, 11, 12, 13]. As the material experiences deformation, the energy that is added is redistributed inhomogeneously and is often concentrated around coarse constituent particles that remain after homogenization. The more energy that is stored locally in the material, the less thermal energy required during solution heat treatment to begin the recrystallization process. Therefore, the size, spacing, and volume fraction of the constituent particles will also affect the extent of recrystallization, although indirectly, by serving as locations for this added energy to localize. This effect is known as Particle Stimulated Nucleation and therefore any processing step that affects the constituent particles, could also have unforeseen consequences on the extent of recrystallization[7].

After the material has been shaped into a stock piece, it is solution heat treated and then quenched. This step primarily serves to increase the number of vacancies in the system and also increase the amount of primary alloying elements Zn, Mg, and Cu in solution[6, 14, 15]. Therefore, both of these steps will increase the aging kinetics of the system and have significant impacts on the type, size, spacing, composition, and total volume fraction of precipitates that form both in the interior of the grain and at the grain boundaries. Additionally, since the solution heat treatment is usually conducted at temperatures similar to those used in the homogenization step, it can also melt some of the remaining constituent particles, and as previously discussed the added thermal energy triggers static recrystallization in the material[6, 7, 14, 15].

Prior to aging, the material is occasionally stretched or cold-rolled[7, 16]. While further deformation obviously affects the texture of the material, it also can affect

the interior of the grain by significantly increasing the dislocation density in these regions. This, in turn, affects the size, spacing, and type of strengthening precipitates that are formed in these regions, since the dislocations serve as heterogeneous nucleation sites[8, 16]. During aging, the material can be heated to any one of a range of low to moderately high temperatures for any length of time to encourage the precipitates of strengthening particles in the grain interior and the growth of equilibrium particles at the grain boundary. While aging heat treatments can consist of only one heating step, it is far more common to combine multiple steps together in a single aging process.

4.2.3 Structure-Property Relationships

When generating the list of properties that are of interest, we listed each of them individually, as shown in Figure 4.8. However, sometimes information about the structural features that drive the properties will not be as detailed. For example, in this and many other materials, distinctions between the features that drive the yield strength versus those that drive only the ultimate strength of the material are not always made. And depending on the application and level of detail that is desired in the map, this designation is not always necessary. The main purpose of initially splitting these properties is: (1) to encourage the user to find out if distinctions between the driving mechanisms for each of these properties are known, and (2) to prevent the user from accidentally grouping properties together that are inappropriate. For example, since information about the ductility is also collected as a part of a standard tensile test, users might be tempted to group this property together with the yield strength, the ultimate strength, and the hardening behavior. However, the mechanisms that drive ductility in this system are much more similar to those that drive the fracture toughness. Had the ductility been grouped with the strength and hardening properties, it would have been impossible to distinguish which mechanisms

drove which properties. In this material, as in many materials, distinctions between the mechanisms driving the yield strength and the ultimate strength are uncommon. However, as they are very closely related in this material, they are both taken to have the same mechanisms unless shown otherwise.

Although high-strength Al-Zn-Mg-Cu alloys are known for being heat-treatable and precipitation-hardened, there are actually multiple mechanisms responsible for their strength properties[2, 3, 4, 5, 6, 17]. The most overlooked of these is perhaps the strengthening effect due to the presence of grain boundaries. While the Hall-Petch relationship does hold in these materials for grain sizes at about above approximately 20μm, this effect becomes even more pronounced for smaller grains[17]. Since these materials are often partially recrystallized, the presence of small sub-grain cell structures typically in the range of 2-5 μm means that the grain size, the extent of recrystallization, and the sub-grain cell size will all significantly impact the yield and ultimate strength of the alloy[4, 5, 17, 18**?**]. Additionally, the grain size and the shift from large recrystallized grains to unrecrystallized regions of smaller cell structures will also greatly impact the hardening behavior of the material. When dislocations accumulate in fine-grained material, the dislocations are more able to rearrange and annihilate, since they are near grain boundaries. When these dislocations accumulate in larger grains, the distance the dislocation must travel to reach a grain boundary becomes larger than the free slip distance, and so the dislocations become accumulated in the bulk and the material is less able to dynamically recover[17].

In addition to the size and the extent of recrystallization, the texture and the misorientation of the grains and the sub-grain cell structures also affects the yield strength, ultimate strength, and the hardening behavior. As the material is strained, one method of accommodating this excess energy is through the rotation of grains or the

polygonzation of the sub-grain cell structures. Therefore, the texture, as expected, will also affect these properties[17, 18].

Similar to the effect of grain size, the precipitation-hardening effect is also caused by an increased ability to trap and accumulate dislocations in the material. Here, the formation of coherent solute clusters stabilizes dislocations, since their presence reduces the strain caused by the volume or lattice mismatch that occurs in the matrix. Since small particles are cut by the moving dislocations, their strength contribution is proportional to their average size and volume fraction. When precipitates become large and increasingly incoherent, they become instead physical barriers to dislocation movement, since the only way for a dislocation to circumvent the particles is by bowing into a roughly semi-circular shape between them[6, 8]. When this bypassing is done without the aid of cross-slip, it is referred to as Orowan looping, and the strength contribution becomes inversely proportional to the size of the particles[2, 6, 7, 19, 20]. It is expected then, that the maximum strengthening effect would be reached when this critical size of the shearing-bypass transition is reached. Indeed the optimization of strengthening precipitate size has been the focus of much of the property optimization work in these material systems to date.

After precipitation hardening has occurred, there are still small amounts of solute that are left in solid solution in the matrix in the interior of the grain boundary. The presence of these solutes contributes to solid solution strengthening. Although this can be a meaningful contribution to the overall strength of the alloy, it is much smaller than some of the others discussed[4]. The amount of strength the remaining solute would be able to impart to the alloy if it was incorporated into additional precipitates is actually much higher than the contribution from remaining in solid solution. Indeed, new processing methods have recently been developed which increase

the total volume fraction of the precipitates in the grain interior, and thereby increase the total strength of the alloy[21].

Fracture toughness is a major design parameter in this class of aluminum alloys, especially as component thicknesses increase. Typically, strength and fracture toughness are considered to be trade-off properties in these materials[6, 22]. This view largely stems from the original processing methods that were developed for increasing fracture toughness in aluminum alloys. In these one-step aging treatments, the material has been observed to slowly lose strength as the material is over-aged, while the corrosion properties and the fracture toughness are both observed to increase with the increased aging. However, rather than being an inherent trade-off, this change in the properties is driven by a change in the size and spacing of both the strengthening precipitates in the interior of the grain and the equilibrium precipitates at the grain boundary. Here, the slightly elevated temperature these over-aging treatments utilize cause both types of precipitates to continue to grow. More recently, much work has been done to develop processing methods that allow for the optimization of the size and spacing of these two separate precipitate types which has in turn led to better strength and fracture toughness or corrosion properties[21, 22, 23, 24, 25, 26, 27]. Once again, this demonstrates that it is critically important to understand and be able to distinguish between the structural and physical mechanisms that drive different properties of interest.

The fracture process is generally agreed to occur in three distinct phases in these alloys, including (1) void nucleation, (2) void growth, which is also considered to be ductile intergranular fracture since it usually occurs through the growth of voids nucleated near grain boundary regions, and (3) void coalescence, which either occurs by the coalescence of voids and the formation of a void sheet, or through the necking

and subsequent failure of the remaining transgranular ligaments[13, 14, 28]. Because of this transition from intergranular to transgranular fracture at different points of the process, it has been reported that the overall fracture toughness is controlled by this transition. However, a clearer perspective can be gained from considering that an increase in the overall toughness of the material will be gained by prolonging the void growth phase, or through delaying void coalescence[28].

Void nucleation typically occurs through the cracking of coarse constituent particles, which are usually between 1-10μm in size. Since these particles are often quite large and typically appear in clusters, the stress required to break them is quite low, and in many cases they will crack during the multiple thermal and mechanical processing steps required to make the component. Therefore decreasing the size and volume fraction of these constituent particles can significant impact the fracture toughness of the material. However, as the stress increases, voids are also formed at the smaller dispersoid particles, which are typically 0.1-1.0-μm. Thus, it is possible that decreasing the size and increasing the coherency of these particles may also help to increase toughness.

Once nucleated, these voids grow through plastic deformation. As the strain increases, the growth of larger voids can happen concurrently with the nucleation and growth of smaller voids, such as those that form at dispersoids. Although the growth rate of voids that are the same size is independent of void spacing, when small voids are located near larger voids, the growth rate of the smaller voids is significantly accelerated due to strain concentration effects. Decreasing the strain hardening ability can also increase the void growth rate[28]. If the grain interior is very strong compared to the precipitate free zone (PFZ) area near the grain boundary, then void growth is halted, and any additional energy is dispersed in the material through void coalescence along

the grain boundaries. This mechanism is responsible for the observed dependence of K_{IC} on the difference in strength between the grain interior and the PFZ. This also explains the severe increase in the amount of intergranular fracture and the overall decrease in the toughness with increasing solute content in Al-Zn-Mg alloys. The increasing solute content increases the strength of the material through the formation of fine particles in the grain interior, thus halting void growth[23]. Therefore the fracture surface goes from being largely transgranular to occurring mainly through intergranular fraction and void coalescence along grain boundaries[23, 28, 29]. This also helps explain the tradeoff between strength and toughness that is observed with over-aging discussed previously.

Once void growth is halted, the voids will begin to coalesce, and the material will fail. This process can occur either intergranularly through the formation of large void sheets, or transgranularly through the necking and failure of the remaining ligaments. The void distribution, while not observed to affect the growth rate, plays a dominant role in the onset of void coalescence[28]. It has been well observed that the area fraction of grain boundaries plays an important role in determining the overall fracture toughness of an alloy[13, 23]. This is due to the acceleration of the void coalescence stage with an increasing areal fraction of the grain boundary, or a decreasing void distribution[23, 28]. There is also evidence that supports the theory that the equilibrium particles at the grain boundary facilitate this void coalescence, rather than playing a part in the direct nucleation and growth of voids, since increasing the size and spacing of the grain boundary particles serves to increase the overall toughness of the material, rather than decrease it. In the over-aged materials discussed earlier, the increase could be accounted for merely by the loss of strength in the grain interior due to the coarsening of strengthening precipitates. But other, more recently developed, processes have shown that this increase is observed even when the interior of

the grain is unchanged and the material still possesses a high strength [14, 22, 26, 27].

Stress corrosion cracking (SCC) is environmentally assisted fracture, which requires both a corrosive environment and the application of an applied stress to occur. Where typical fracture occurs in three steps consisting of void nucleation, growth, and coalescence, SCC consists of two distinct mechanisms: (1) pitting, which causes a stress concentration and allows for the formation of a crack, and (2) crack growth, which is often measured by the SCC plateau velocity. Pitting can increase the likelihood that a sharp crack in the surface of the material will be present. Once the stress concentration in this area reaches the threshold stress intensity, K_{ISCC}, the crack will begin to propagate. Since SCC is effectively accelerated intergranular fracture in the presence of a corrosive environment, it is unsurprising that many of the microstructure parameters that accelerate or affect the fracture toughness and ductility, also affect the SCC resistance[30].

Just as increasing the extent of recrystallization in the material will decrease the overall toughness; increasing amounts of recrystallization will also increase the susceptibility of the material to SCC[13, 31]. One mechanism responsible for this is that unrecrystallized sub-grain boundaries, and the dispersoids that are often present at them, are very effective at trapping hydrogen, and therefore their presence can decrease the amount of hydrogen present in the grain boundary regions where SCC is most likely to occur[4, 10]. Therefore an increase in the extent of recrystallization, which is usually an indication of lower dispersoid presence, will usually be observed with an increase in the SCC plateau crack velocity.

Some constituent particles are cathodic with respect to the surrounding the matrix material and can dissolve the material around them through the formation of

microgalvanic cells[32]. This decohesion between the particle and the matrix causes pitting, and therefore constituent particles play a role in initiating SCC through the formation of pits that is roughly equivalent to the role they play in void nucleation in the fracture and ductility processes. It was also previously discussed that, although grain boundary particles do not play a role in void nucleation and growth, they are important in the facilitation of void coalescence. Therefore, increasing the size of these particles does not have a detrimental effect on the fracture toughness, and increasing the discrete spacing between them actually has a positive effect. Here, similarly increasing both the size and the spacing of these grain boundary precipitates increases both their ability to effectively trap hydrogen, and increases the amount of time it takes for them to anodically dissolve.[15, 21, 23, 24].

However, changing the chemistry of the microgalvanic cell that is formed between the grain boundary precipitate and the surround PFZ can be more influential on the SCC resistance than changes in size and spacing. It is well known in this material system, that increasing the amount of Cu in the grain boundary precipitates enobles the precipitate, or makes it less electrochemically active[33, 34, 35]. Therefore, changing the parent composition of the alloy, or changing the aging process to increase the amount of Cu locally incorporated into grain boundary precipitates will greatly affect the corrosion properties of the material[34, 35].

4.2.4 Merge Structure Lists and Adjust for Detail

Once all of the relationships between the three columns have been mapped, the two structures lists have been merged together. Here, the advanced state of this material system is again an advantage, since the two structure columns match and there are no unknown or unexplored relationships that need to be identified. However, this does not mean that the map that has been generated here is static. As discussed in the

known structure-property relationships, much work continues to be done to better understand the chemical and physical mechanisms that drive these properties.

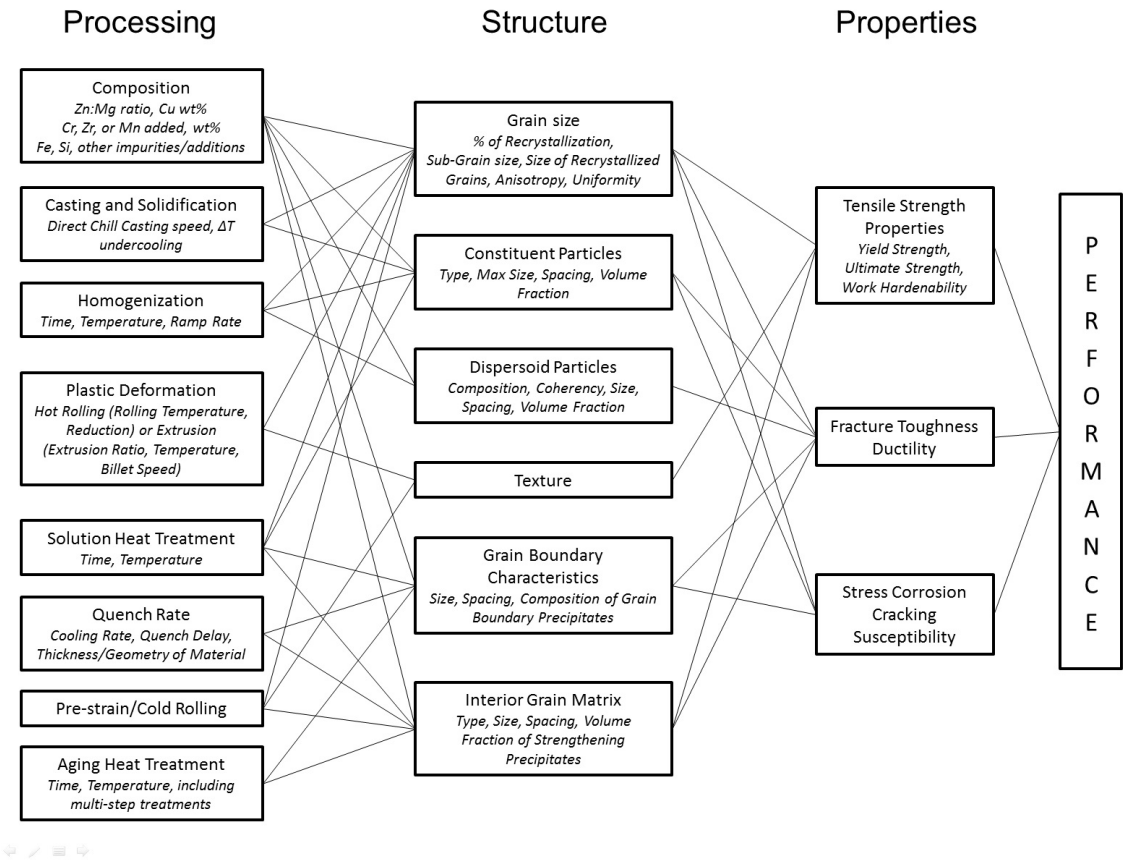

Figure 4.10: Here, the two structure lists that were generated are merged, and some of the properties have been grouped.

We can also adjust the level of detail by grouping some of the properties we are interested in based on the mechanisms that drive them. Here, we can easily group together yield and ultimate strength, as well as work hardenability. Similarly, we can group fracture toughness and ductility together if desired. Once the PSPP map for a materials system has been developed, it can be used to communicate important information about the physical and chemical mechanisms that drive the system, and about what information must be captured to adequately characterize the material in its entirety.

4.3 Using the PSPP Map

One of the most important things in modeling process-structure-property-performance relationships is making sure that all of the factors that influence the element being predicted are being accounted for. Some of the only successful predictive modeling work in this material system has been in predicting the yield and ultimate strength as a function of various aspects of the microstructure. In each of these cases, this success was due to the ability to individually calculate the different strengthening contributions such as precipitate strengthening, solution strengthening, the strengthening effect due to the presence of grain boundaries, and the strengthening effect due to dislocation-dislocation interactions, and to sum them together using various super-positioning methods.

The PSPP map, therefore, can be quite useful in making it clear which of these mechanisms needs to be accounted for in such an attempt. But clearly laying out all of the mechanisms that are involved, these individual mechanisms can be more easily decoupled and predicted individually. The map is also useful in understanding which mechanisms may be missing and therefore constraining the usefulness of the model that has been built. This is also true in the case of predicting the yield or ultimate strength as a function of the various mechanisms that were previously mentioned. Using the map as demonstrated in Figure 4.11, it is easy to see that unless the texture of the material is accounted for, the relationship that was developed may not successfully extend and the predictive model is constrained. In these strengthening equations, the texture is often accounted for with a Taylor factor, which makes rough approximations about the textures that can be accounted for. In this case understanding that the texture of the material does affect the strength can help users of these predictive modeling tools fully understand any assumptions being made about the material, and adjust their expectations accordingly.

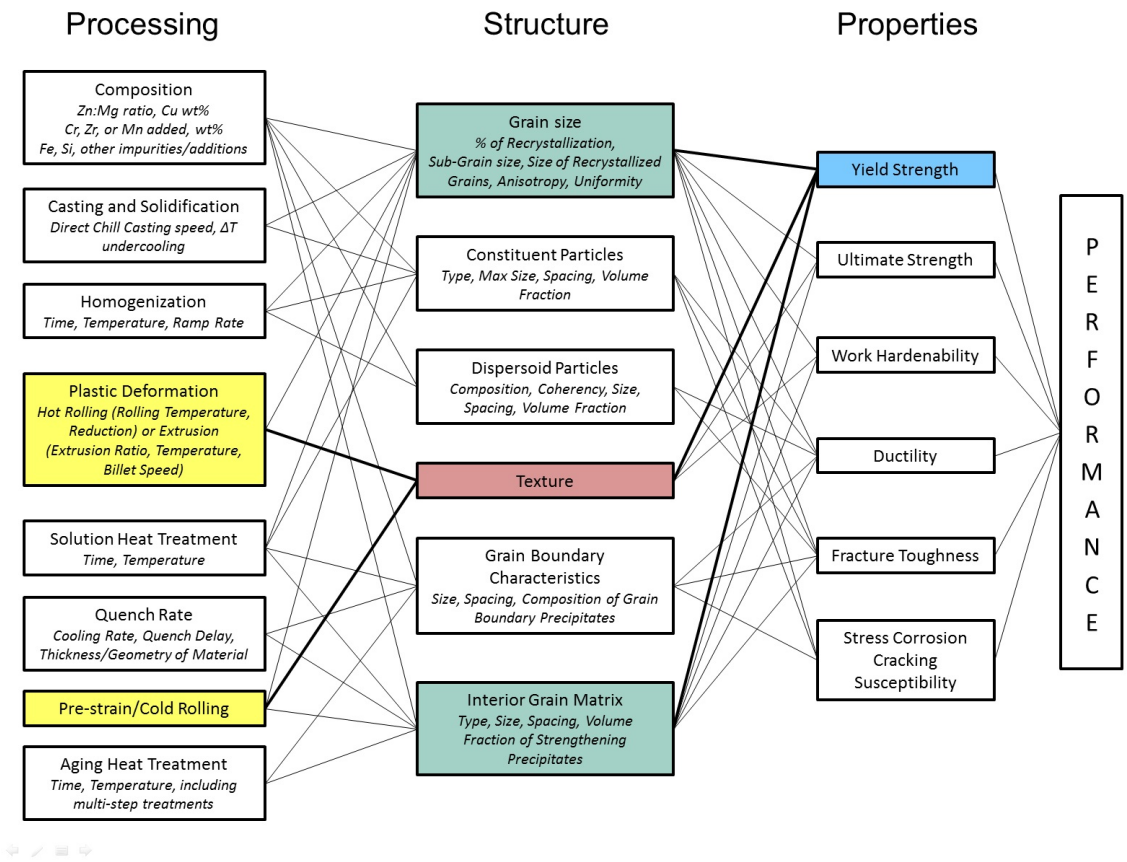

Figure 4.11: If the yield strength is not modeled directly as a function of the texture of the material, then the model must either account for it indirectly through the processing steps that affect the texture, or the modeling tool will be accurate only for other materials with that texture profile.

Another important ability of these PSPP maps is to clearly identify what information must be captured to fully characterize or describe the material. This is especially important in materials systems where some or all of the processing steps are executed by a commercial company. In Al-Zn-Mg-Cu alloys, the casting, homogenization, and formation of a material in to a stock piece is not commonly conducted as a part of academic studies, both in part due to the complexity of these steps as well as the cost of infrastructure required to obtain reasonably defect-free pieces. Since these materials are made quite commonly industrially, it is far more common to order material that has already been partially or completely processed and simply re-solution heat treat,

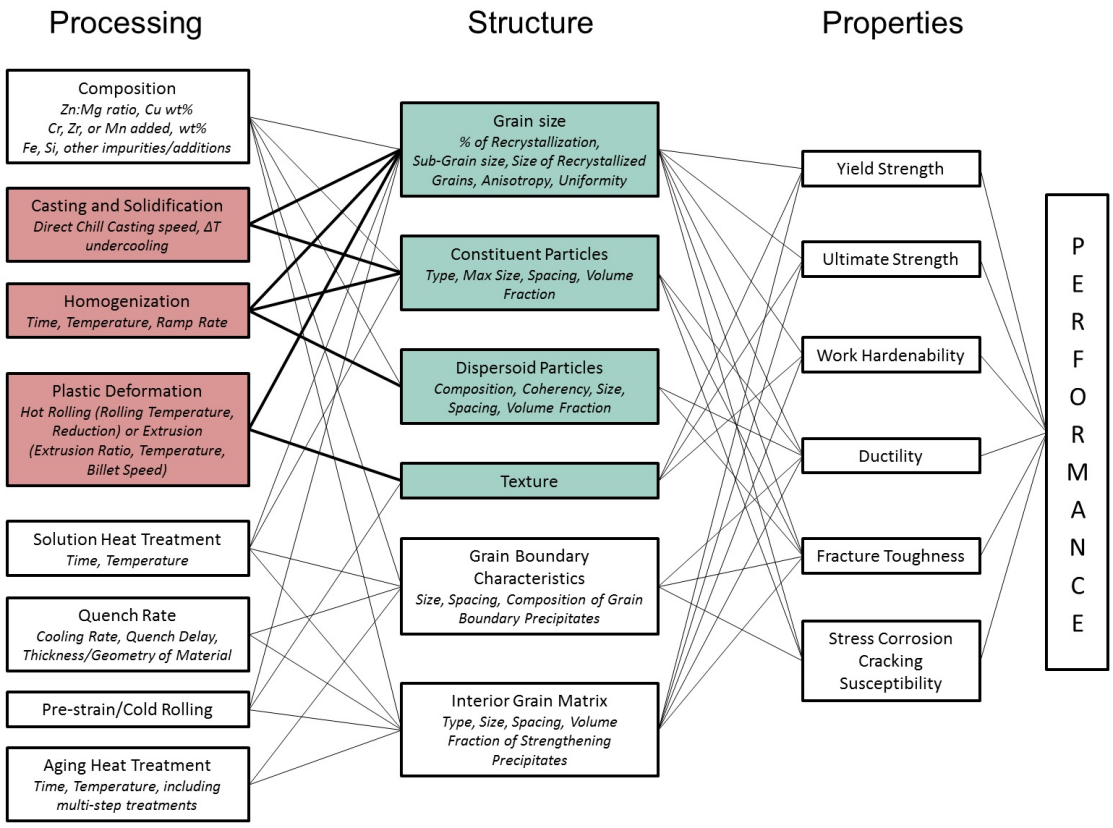

Figure 4.12: If processing information is unknown, then it is still possible to completely define the material by characterizing the structural features those steps influence.

quench, and age the material for study. Additionally, the casting and homogenization steps in particular are often highly proprietary, and therefore this processing information is rarely if ever reported to the end user. By using the PSPP map for this system as shown in Figure 4.12 however, it is possible for a user to still fully characterize or describe the material in question, even if these processing details are unknown. Here, we can see that even if the casting, solidification, homogenization, and plastic deformation processes are unreported, the material can still be adequately described by fully characterizing the grain size information, the constituent and dispersoid particle profiles, and the texture. This application of the PSPP map is especially useful when gathering literature databases in a material system, since computational models are

only as accurate as the data that is used to develop them. If the data sets that are used to develop and train a computational tool are incomplete, or limited, then the model will be similarly limited at best, or at worst inaccurate.

4.4 References

[1] The National Science and Technology Council. Materials genome initiative for global competitiveness, June 2011. URL `www.whitehouse.gov/site/default/files/microsites/ostp/materials_genome_initiative-final.pdf`.

[2] H. R. Shercliff and M. F. Ashby. A process model for age hardening of aluminum alloys - I. the model. *Acta Metallurgica Materelia*, 38:1789–1802, 1990.

[3] A. Deschamps and Y. Brechet. Influence of predeformation and ageing of an Al-Zn-Mg alloy - ii. modeling of precipitation kinetics and yield stress. *Acta Materialia*, 47:293–305, 1999.

[4] M. Dixit, R. S. Mishira, and K. K. Sankaran. Structure-property correlations in Al 7050 and Al 7055 high-strength aluminum alloys. *Materials Science and Engineering A*, 478:163–172, 2008.

[5] M. J. Starink and S. C. Wang. A model for the yield strength of overaged Al-Zn-Mg-Cu alloys. *Acta Materialia*, 51:5131–5150, 2003.

[6] J. R. Davis, editor. *Aluminum and Aluminum Alloys*. ASM International, 1993.

[7] Justin Lamb. *Decomposition and its effects on Mechanical Properties in Al-Zn-Mg-Cu Alloys*. PhD thesis, Georgia Instiute of Technology, 2015.

[8] David A. Porter, Kenneth E. Easterling, and Mohamed Y. Sherif. *Phase Transformation in Metals and Alloys*. CRC Press, 3rd edition edition, 2009.

[9] J. B. Hess. Physical metallurgy of recycling wrought aluminum alloys. *Metallurgical Transactions A*, 14A:323–327, 1983.

[10] J. D. Robson and P. B. Prangnell. Dispersiod precipitation and process modelling in zirconium containing commercial aluminum alloys. *Acta Materialia*, 49:599–613, 2001.

[11] X. Zhang, W. Liu, S. Liu, and M. Zhou. Effect of proprocess parameters on quench sensitivity of an AA7050 sheet. *Materials Science & Engineering, A: Structural Materials: Properties, Microstructure and Processing*, 528:795–802, 2011.

[12] H. Zhang, N. Jin, and J. Chen. Effect of processing parameters on quench sensitivity of an AA7050 sheet. *Transactions of Nonferrous Metals Society of China*, 21:437–442, 2011.

[13] N. U. Deshpande, A. M. Gokhale, D. K. Denzer, and John Liu. Relationship between fracture toughness, fracture path, and microstructure of 7050 aluminum alloy: Part i. quantitative characterization. *Metallurgical and Materials Transactions A: Physical Metallurgy and Materials Science*, 29A:1191–1201, 1998.

[14] N. M. Han, X. M. Zhang, S. D. Liu, D. G. He, and R. Zhang. Effect of solution treatment on the strength and fracture toughness of aluminum alloy 7050. *Journal of Alloys and Compounds*, 509:4138–4145, 2011.

[15] J. Beddoes. Design of solution heat treatments for aerospace alloys. *Canadian Metallurgical Quarterly*, 3:215–221, 50.

[16] N. M. Han, X. M. Zhang, S. D. Liu, B. Ke, and X. Xin. Effects of pre-stretching and ageing on the strength and fracture toughness aluminum alloy 7050. *Materials Science & Engineering, A: Structural Materials: Properties, Microstructure and Processing*, 528:3714–3721, 2011.

[17] R. Mahmudi. Grain boundary strengthening in a fine grained aluminum alloy. *Scripta Metallurgica*, 32:781–786, 1995.

[18] S. Zhang, W. Hu, R. Berghammer, and G. Gottstein. Microstructure evolution and deformation behavior of ultrafine-grained Al-Zn-Mg alloys with fine eta' precipitates. *Acta Materialia*, 58:6695–6705, 2010.

[19] R. B. Nicholson, G. Thomas, and J. Nutting. The interaction of dislocations and precipitates. *Acta Metallurgica*, 8:172–176, 1959.

[20] W. M. Lee and M. A. Zikry. Modeling the interfacial plastic strain incompatibilities associated with dispersed particles in high strength aluminum alloys. *Acta Materialia*, 60:1669–1679, 2012.

[21] Jin-feng Li, Zhuo-Wei Peng, Chao-xing Li, Zhi-quang Jia, Wen-jing Chen, and Zi-qiao Zheng. Mechanical properties, corrosion behaviors and microstructures of 7075 aluminum alloy with various aging treatments. *Transactions of Nonferrous Metals Society of China*, 18:755–762, 2008.

[22] N. Kamp, I. Sinclair, and M. J. Starink. Toughness-strength relations in the overaged 7449 Al-based alloy. *Metallurgical and Materials Transactions A: Physical Metallurgy and Materials Science*, 33A:1125–1136, 2002.

[23] Gerard M. Ludtka and David E. Laughlin. The influence of microstructure and strength of the fractoughness and toughness of 7xxx series aluminum alloys.

Metallurgical Transactions A, 13A:411–425, 1982.

[24] J. F. Li, N. Birbilis, C. X. Li, Z. Q. Jia, B. Cai, and Z. Q. Zheng. Influence of retrogression temperature and time on the mechanical properties and exfoliation corrosion behavior of aluminum alloy AA7150. *Materials Characterization*, 60: 1334–1341, 2009.

[25] A. Karaaslan, I. Kaya, and H. Atapek. Effect of aging temperature and of retrogression treatment time on the microstructure and mechanical properties of alloy AA7075. *Metal Science and Heat Treatment*, 49:443–447, 2007.

[26] R. N. Lumley, I. J. Polmear, and A. J. Morton. Interrupted aging and secondary precipitation in aluminum alloys. *Materials Science and Technology*, 19:1483–1492, 2003.

[27] R. N. Lumley, I. J. Polmear, and A. J. Morton. Development of mechanical properties during secondary aging in aluminum alloys. *Materials Science and Technology*, 21:1025–1033, 2005.

[28] T. Pardoen, F. Scheyvaerts, A. Simar, C. Tekoglu, and P. Onck. Multiscale modeling of ductile fracture in metallic alloys. *Comptes Rendus Physique*, 11: 326–345, 2010.

[29] T. H. Sanders and E. A. Starke. Relationship of microstructure to monotonic and cyclic straining of 2 age hardening aluminum alloys. *Metallurgical Transactions A*, 7:1407–1418, 1976.

[30] J. R. Davis, editor. *Corrosion of Aluminum and Aluminum Alloys*. ASM Internation, 1999.

[31] Amjad Saleh El-Amoush. Intergranular corrosion behavior of the 7075-T6 aluminum alloy under different annealing conditions. *Materials Chemistry and Physics*, 126:607–613, 2011.

[32] N. Birbilis, M. K. Cavanaugh, and R. G. Buchheit. Electrochemical behavior and localized corrosion associated with Al7Cu2Fe particles in aluminum alloy 7075-T651. *Corrosion Science*, 48:4202–4215, 2006.

[33] N. Birbilis and R. G. Buchheit. Electrochemical characteristics of intermetallic phases in aluminum alloys. *Journal of the Electrochemical Society*, 152:B140–B151, 2005.

[34] G. Sha, L. Yao, X. Liao, S. P. Ringer, Z. C. Duan, and T. G. Langdon. Segregation of solute elements at grain boundaries in an ultrafine grained Al-Zn-Mg-Cu alloy. *Ultramicroscopy*, 111:500–505, 2011.

[35] R. K. Gupta, A. Deschamps, M. K. Cavanaugh, S. P. Lynch, and N. Birbilis.

Relating the early evolution of microstructure with the electrochemical response and mechanical performance of a Cu-rich and Cu-lean 7xxx aluminum alloy. *Journal of The Electrochemical Society*, 159:492–502, 2012.

PART II: GENERATING AN EXPERIMENTAL DATA SET

Introduction

Now that a standard method of communicating the process-structure-property-performance linkages within the system has been developed, we can use this map to isolate and explore these relationships. Implicitly, experimental design says that we explore such a relationship by allowing one or more variables in the system to change, hold the rest constant, and observe how the behavior of the system changes. Here, the presence of the map helps to ensure that all of the necessary variables are being accounted for in one of these two ways: either by being held constant or by being allowed to vary and being accurately measured and defined. If not all of the variables are accounted for, the system will exhibit unexplainable and unpredictable fluctuations or behavior.

Traditionally, the focus has been to decouple relationships enough to look at one-to-one relationships in this space, such as the effect of solution heat treatment on the extent of recrystallization, or the effect of the constituent particle size and volume fraction on the fracture toughness of the material. While examining these one-to-one relationships helps build our scientific intuition of the phenomenological behavior of the system, it cannot always elucidate the physical mechanisms that are responsible for the observed response.

Although the map makes no distinction between confirmed physical mechanisms and merely observed or causal phenomenological behavior, without an understanding of the physical mechanisms driving that system, we can predict the system response but we cannot tailor that response or design a material to have a targeted set of features or behavior that is outside of the observed response. Therefore, in order to really enable property optimization in this space, the physical mechanisms and not just the

phenomenological response must be captured. This means that if a physical mechanism involves interactions between multiple identified variables, it may be necessary to collect experimental data on the variation of multiple variables at once in order to examine possible interactive effects. This is good news since allowing only one microstructural feature, such as grain boundary particle size, to vary while holding all others constant is at best, impractical. Instead, multiple variables can be allowed to fluctuate simultaneously as long as they are being measured. The drawback, however, is that if all of the involved variables are not being tracked or held constant then no conclusions can be drawn about their relationship.

The materials design space in the Al-Zn-Mg-Cu system defined in Chapter 4 is quite large and has many different variables that might need to be tracked and measured. Controlling and accounting for so many variables, and the amount of experimental testing and characterization involved may be time- or cost-prohibitive for many projects. Here, we attempt to execute such a project by varying multiple processing parameters within the system, characterizing the varying features of the microstructure, and measuring the resulting mechanical properties using commonly available methods to determine the feasibility of such an undertaking. In addition to evaluating the feasibility of the various measurement and characterization methods, the raw data and the analyzed results for this work are cataloged in an associated data repository and have been made available for use in future work in this and other areas.

CHAPTER 5

MATERIAL PROCESSING

One of the major goals of this work was to examine our ability to track and measure as many of the different variables withing the Al-Zn-Mg-Cu space as possible using commonly available methods. In order to do this multiple stock pieces of AA7050, purchased from Alcoa Inc., were re-solution heat treated, quenched, and aged in order to indirectly vary as many of the microstructural features as possible. As discussed in Part I of this work, one of the concerns with commercially processed aluminum alloys is that many of the steps, including the casting and solidification, the homogenization, and the plastic deformation applied to form the stock piece, are often proprietary and not available. Since these steps do affect many of the aspects of the final microstructure, in order to examine the process-structure properties within the space it is necessary to ensure these steps are conducted in a constant way across all of the material specimens being examined. If only the structure-property relationships are to be examined then either these initial processing steps need to be held constant or the microstructural aspects they control must be thoroughly characterized to ensure that they are not causing any effects which might be unaccounted for. Here we discuss the stock material which was purchased for this project, the approach to the processing of the material to ensure that these initial steps were applied consistently, and the steps which were altered and the microstructural features we expect them to affect.

5.1 The Material

The material used in this portion of the project was 7050 aluminum, made by Alcoa Inc. Eighteen plates of 7050-T7451 were received, sized 20"x8"x3" (L-T-S). These

plates were delivered with the certified composition reported in Table 5.1, which was confirmed for each plate using a handheld X-Ray Fluorescence (XRF) machine. The lot and casting numbers of the order can be found in the attached mill certification, located in the associated data repository.

Table 5.1: Chemical composition of the as-received material compared the ASTM standards, by weight.

Alloy	Zn	Mg	Cu	Cr	Mn	Zr	Ti	Fe	Si	Al
As-Received	6.1	2.2	2.3	0.01	0.01	0.11	0.02	0.08	0.04	rem
Min	5.7	1.9	2.0	–	–	0.08	–	–	–	rem
Max	6.7	2.6	2.6	0.04	0.10	0.15	0.06	0.15	0.12	rem

5.2 Processing Routes

Due to a limit in available equipment, only the solution heat treatment time and temperature, the quenching rate, and changes in the aging time and temperature were available for change. The composition; the cooling rate and speed of the material through the DC casting system during solidification, the homogenization time, temperature, and ramp rate; the total rolling reduction and the deformation rate during plastic deformation were all fixed. Equipment to apply pre-straining or additional cold rolling to the material after quenching and prior to the aging treatment was unavailable.

Therefore, the processing parameters that were varied in this project were the solution time and temperature, the quenching medium to change the cooling rate, and the aging time and temperature. The processing routes that were explored in this project were chosen to generate a wide variety of microstructures, aimed at changing the extent of recrystallization; the size, spacing, and total volume fraction of grain

interior precipitates; the size, spacing, and local electrochemistry of the grain boundary precipitates; and size and total volume fraction of large constituent particles. It was important that the processing routes chosen generated what might be considered poor mechanical property results, rather than just advantageous ones. This allows for a more full exploration of the PSPP space and allows for more robust computational models that are generated from this data. Previous work by other authors, which was detailed in Part I, was heavily relied on to make decisions about the specific processing parameters that should be employed here.

5.2.1 Solution Heat Treatments

As discussed in Chapter 2, the solution heat treatment (SHT) step has two primary functions. The primary function is to increase the equilibrium centration of both solute and vacancies, with a secondary goal of dissolving coarse constituent particles that remain in the material [1]. As seen in the PSPP map in Chapter 4, the time and temperature of the SHT can affect the size and volume fraction of the constituent particles; the extent of recrystallization; and to some extent the size, spacing, and volume fraction of the precipitates in the interior of the grain.

Industrially, the solution heat treatment step is carried out either in a large air chamber furnace or a molten salt bath [2, 3]. This work used a large, electrically-heated, industrial air-furnace at Gulfstream Aerospace Corporation. It has been noted that the atmosphere in air chamber furnaces must be tightly controlled to prevent potential porosity problems, which 7xxx series alloys, particularly 7050, are prone to [2, 3]. This porosity is caused by the presence of moisture in the atmosphere, which acts as a source of hydrogen. The hydrogen diffuses into the material and gathers at inclusions and other discontinuities, and as the gas continues to heat it forms surface blisters

on the part. To remove this moisture, the material must be thoroughly cleaned and dried prior to beginning treatment, and a small pan of ammonium fluoroborate is typically added to the chamber furnace (MacKenzie). These precautions were all followed in the solution heat treatments executed by the team at Gulfstream, and the heat treatment logs can be found in the associated data repository.

As mentioned in the introduction, it was important that the SHT parameters were chosen to generate a wide variety of available microstructures. In 2011 Han et al. published a study that explored the effect that various SHT parameters, including multi-step treatments, had on the microstructure, strength, and fracture toughness of 7050 aluminum [4]. In this particular study, the authors also used 3 thick hot-rolled aluminum, which was solution heat treated in an air furnace and quenched in room temperature, before receiving a T76 aging treatment. The solution heat treatment steps they explored are shown in Figure 5.1.

Test number	First step	Ramp rate	Second step	Ramp rate	Third step
SST440	440 °C/2.5 h				
SST450	450 °C/2.5 h				
SST460	460 °C/2.5 h				
SST470	470 °C/2.5 h				
SST480	480 °C/2.5 h				
SST490	490 °C/2.5 h				
EST	450 °C/1.5 h	60 °C/h	480 °C/0.5 h		
HTPT	450 °C/1.5 h	60 °C/h	480 °C/0.5 h	30 °C/h	420 °C/0.5 h

Figure 5.1: The solution heat treatment steps explored by Han et al. [4].

These heat treatments did successfully vary the constituent particle volume fraction, the extent of recrystallization, and as a result the mechanical properties of the system. The results as reported are shown in Figure 5.2[4]. Most of the samples tested (75%) involved a single step SHT at temperatures between 440 °C (824 °F) and 490 °C (914 °F). This is the typical SHT that is applied in industry, since ASTM B918 recommends solution heat treating 7050 aluminum of this type at 477 °C (890 °F) for

4 hours in an air furnace [2]. These single step treatments can significantly alter the microstructure properties. For example, the volume fraction of constituent particles seems to decrease linearly with increasing temperature, especially at temperatures at and above 450 °C (842 °F). The extent of recrystallization, while it does change, doesn't change as significantly until higher temperatures. A SHT at 450 °C (842 °F) results in only 5% recrystallization, and increasing the SHT to 470 °C (878 °F) only increases the amount of recrystallization to 10%. But SHTs at 480 °C (896 °F) and 490 °C (914 °F) increase the volume fraction of recrystallization to 52% and 87%, respectively [4]. Therefore, it was decided that our work should include multiple samples that were subjected to a single step SHT at differing temperatures from approximately 450 °C (842 °F) to 490 °C (914 °F).

The authors also tested two multi-step treatments: one two-step treatment they termed an enhanced solution treatment (EST), and a three-step treatment known as a high temperature pre-precipitation treatment (abbreviated here as HTPT). As seen in Figure 5.2, the EST results in both a low fraction of constituent particles and a low amount of recrystallization, making it an attractive option to include in our work. The concept of a high pre-precipitation heat treatment has also been explored by other authors, including a 2012 study by Huang et al. who examined multiple HTPTs in 7055 aluminum [5]. The idea behind these treatments is that the third step in the SHT, which is carried out at a lower temperature from °C (788 °F) to 465 °C (869 °F), promotes the pre-precipitation of η precipitates at grain boundaries, and increases the size and separation of these particles in the final microstructure. This multi-step SHT, therefore, is thought to lead to improved fracture toughness and SCC resistance in these alloys. Higher temperatures for the pre-precipitation step, such as those examined in the Huang study, have unclear and somewhat contradicting effects

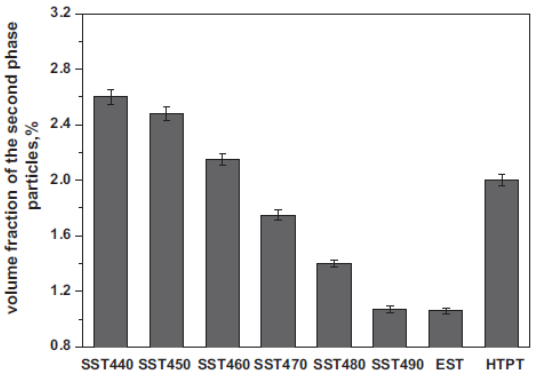

(a) The variation in the volume fraction of constituent particles that was achieved.

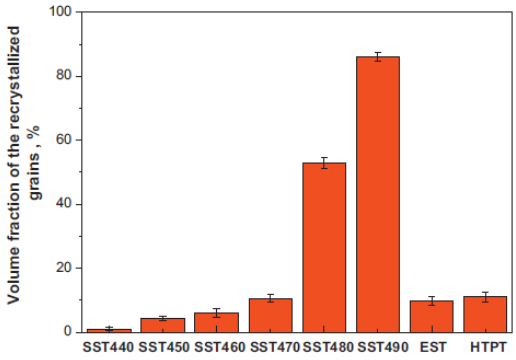

(b) The variation in the extent of recrystallization that was achieved.

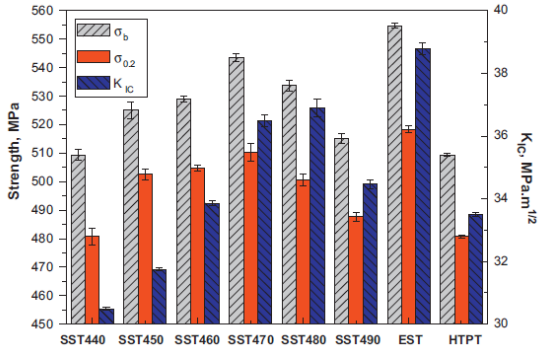

(c) The resulting variation in strength and fracture toughness that was achieved by varying these microstructural features.

captionsetupjustification=centering,margin=0.5cm

Figure 5.2: The variation that was achieved in various microstructural features and resulting mechanical properties using the solution heat treatment schedule shown in Figure 5.1 [4].

on the final mechanical properties of the system, and the microstructure characteristics are not reported. However, the lower pre-precipitation step at 420 °C (788 °F) reported by Han et al. has a similar constituent particle fraction and extent of recrystallization as the single step 470 °C (878 °F) SHT, but very different mechanical properties. This implies that the HTPT is also effective at altering the grain interior precipitate characteristics, the third and final microstructure characteristic that the solution heat treatment step is capable of affecting. Therefore, it was decided that one sample subjected to a HTPT should also be included in this study.

5.2.2 Quenching Options

While the role of the SHT process is to increase the equilibrium concentration of both solutes and vacancies, it is the function of the quenching process to trap those solutes and vacancies in the solid solution where they can aid in the precipitation kinetics. If the cooling rate of the material is not sufficiently fast, then precipitation will occur at intermediate temperatures where the equilibrium supersaturation is smaller, but the diffusion rate and the equilibrium vacancy concentration is still fairly large. This precipitation process during cooling has been known to reduce the amount of hardening that is possible in the aging step [3]. Therefore, the quench rate affects the final microstructure characteristics in both the interior of the grain and the grain boundary regions. As noted in Chapter 2, changes in the parent composition of the alloy, even with small additions of certain alloys like Ag, can significantly alter the quench sensitivity of the material. The quenching characteristics can also be strongly influenced by the thickness of the part.

Quenching of industrial parts typically occurs by immersion either in cold water baths or in baths of an aqueous polymer solution such as polyalkylene glycol (PAG)

polymers, though sometimes other methods may be permitted [2, 3]. The effect of quenching is not commonly studied in academia in high-strength aluminum parts, even though distortion issues during the quenching stage is the most defect and is likely responsible for most of the non-value added work and costs that are associated with the heat treating of these parts [3]. Aluminum is actually more prone to distortion during the quenching process than steel, since although it does not experience a coupled phase transformation, the coefficient of linear expansion is approximately twice as high for aluminum. This means that changes in the length or volume of aluminum parts can be significantly greater than in corresponding steel parts. This is important to note in automotive applications, where high-strength aerospace aluminum alloys are beginning to replace parts traditionally manufactured from steel.

In the aerospace industry, quenching in PAG polymers is preferred since they offer a greater degree of control over the cooling rate, and can therefore be used to minimize distortion issues [3]. This control comes from the inverse solubility that PAG polymers exhibit in water. When the part is immersed, the solution in contact with the metal surface polymerizes and forms a stable polymer-rich film. Depending on the concentration of the PAG, the temperature, and the agitation in the bath this film will eventually collapse in a uniform fashion, and new PAG solution will come in to contact with the surface and the cycle will repeat. This "nucleate boiling" effect is responsible for the high heat extraction rates that can be obtained in this medium [3].

In this work, the only quenching medium available was immersion in water. Therefore, this work explored changing the quenching rate by quenching in room temperature water according to the ASTM B918 standard, and by quenching in warm and hot water. While it was directed that one sample be quenched in water at approximately 57 °C (135 °F) and one be quenched in water at approximately 85 °C (185 °F), reports

from the manufacturing floor indicate that the water temperature after quenching these samples was only 110 °F and 127 °F, respectively. This can be found in the heat treatment log provided by Gulfstream, located in the associated data repository.

It is well known that the -W or as quenched condition is not stable, especially in 7xxx series alloys, and that if left at room temperature the material will begin to naturally age [2, 3]. However, it is very common to need to hold materials for some period of time after quenching, before the aging treatment can be applied. This is accomplished by refrigerating the material. Although natural aging isn't fully suppressed until -40 °C, refrigeration in industrial processes usually occurs at or near -18 °C [3]. In this work, the as quenched material was held in refrigeration at 0 °F for no more than 30 consecutive days, and was thoroughly cleaned and dried before aging.

5.2.3 Aging Heat Treatments

As discussed in Chapters 2 and 3, Al-Zn-Mg-Cu alloys such as 7050 gain their superior strength mainly through the precipitation-hardening effect, which allows them to trap and accumulate dislocations in the material. The type, size, spacing, and volume fraction of the strengthening particles found in the interior of the grain can all be altered by the aging heat treatment. Changes in the aging treatment can also affect the size, spacing, and composition of equilibrium particles found at the grain boundary, and in some cases even affect the PFZ size.

Commercially, 7050 aluminum is available in T7451 or T7651 plate (if the material is ordered as an extrusion then these tempers are designated T74511 and T76511, respectively)[6]. It is not typically offered in a T651 temper, since the peak strength temper has poor fracture toughness and stress corrosion cracking properties, which

are both common design parameters in thick-section applications where this material is utilized. If these design parameters are not important and merely a high-strength is desired, 7075 is usually used, which is commonly available in T651 temper [1, 2, 6]. The -51 addition in plate material, and the -511 addition in extruded materials, indicates that the material was cold stretched to stress-relieve the material prior to aging. In this work, equipment to cold stretch the material was not available, and so temper designation do not carry this addition even though the aging time and temperature are the same [2].

While these traditional processes are commonly available commercially, retrogression and re-aging treatments, interrupted aging treatments, and other experimental treatments are not. However, their improved results on mechanical properties have been explored in academic work. Therefore, it was decided that this work would include (1) specimens that were aged using more traditional processes, including under-aged, T6, T74, T76, and an additional over-aged treatment; (2) specimens that had experienced various retrogression and re-aging like treatments, including specimens that hadnt experienced the initial T6 treatment prior to retrogression; (3) and specimens that had experienced various stages of the interrupted T6I4 and T6I6 treatments.

5.3 The Testing Matrix

The eighteen plates of 7050-T7451 were each assigned an alpha-numeric identification number and processed at Gulfstream Aerospace Corporation according to the test matrix included here, shown in Fahrenheit. The material processing logs are included in the associated data repository.

ID#	Material	Soln-Treat (°F/hrs) +/- 10°F (Air Furnace)	Quench	Heat-Treatment (°F/hrs) +/- 10°F
A1	7050	840/4h	RT water	250/6h, 330/24h
A2	7050	895/4h	RT water	250/6h, 330/24h
A3	7050	920/4h	RT water	250/6h, 330/24h
A4	7050	840/3h, 895/1h	RT water	250/6h, 330/24h
A5	7050	840/3h, 895/1h, 790/1h	RT water	250/6h, 330/24h
B1	7050	895/4h	Water 135F	250/6h, 330/24h
B2	7050	895/4h	Water 185F*	250/6h, 330/24h
C1	7050	895/4h	RT water	250/6h
C2	7050	895/4h	RT water	250/6h, 330/6h
C3	7050	895/4h	RT water	250/6h, 330/12h
D1	7050	895/4h	RT water	250/20h, 375/0.5h, 250/24h
D2	7050	895/4h	RT water	250/24h
D3	7050	895/4h	RT water	375/0.5h, 250/24h
D4	7050	895/4h	RT water	250/20h, 375/3h, 250/24h
D5	7050	895/4h	RT water	375/3h, 250/24h
E1	7050	895/4h	RT water	250/0.5h, 150/24h, 250/12h
E2	7050	895/4h	RT water	250/0.5h, 150/24h
E3	7050	895/4h	RT water	250/0.5h

Notes:

*Or highest available temperature on the bath

- Solution-treatment times based on ASTM B918 soak times for each environment
- Properties are sensitive to time elapsed at RT between quenching and heat-treatment. All pieces should be held at lowest possible temperature in between steps.
- Material should be quenched immediately after solution treatment. Max quench delay per ASTM B918 is 15s, but realistically, as soon as possible.
- Air furnace time should begin when the temperature of the furnace reaches the specified range, rather than when the material enters the furnace.
- When going from a high to a low temperature during heat-treatment, always quench the piece in RT water. Free the piece in between next step if necessary. When going from low to high, ramp the oven and begin time when over reaches required temperature range.

5.4 Post-Processing Cutting of Test Coupons

After processing each plate was cut in to 42 test coupons, according to the schematic given in Figure 5.3 and given a specimen identification number as indicated. To the extent possible, the specimens were taken from the middle section of the plate to account for edge effects and any potential surface blistering that may have occurred during processing. The only specimens that contain the edges of the plate were the fracture toughness specimens, due to their large dimension requirements which are discussed in Chapter 8. Cutting was done at Gulfstream Aerospace Corporation using a water jet for initial large section cuts where possible, and additional cuts to separate the specimens were made with a band saw. Although tolerances were high and the surface finish allowed for cutting was rough, each test coupon was separately machined into test specimens, so any potential damage layer caused by cutting at this step was later removed.

Some test coupons that were generated were held for future mechanical properties test in other follow up projects. The different test coupons and their allocated purpose are shown in Table 5.2.

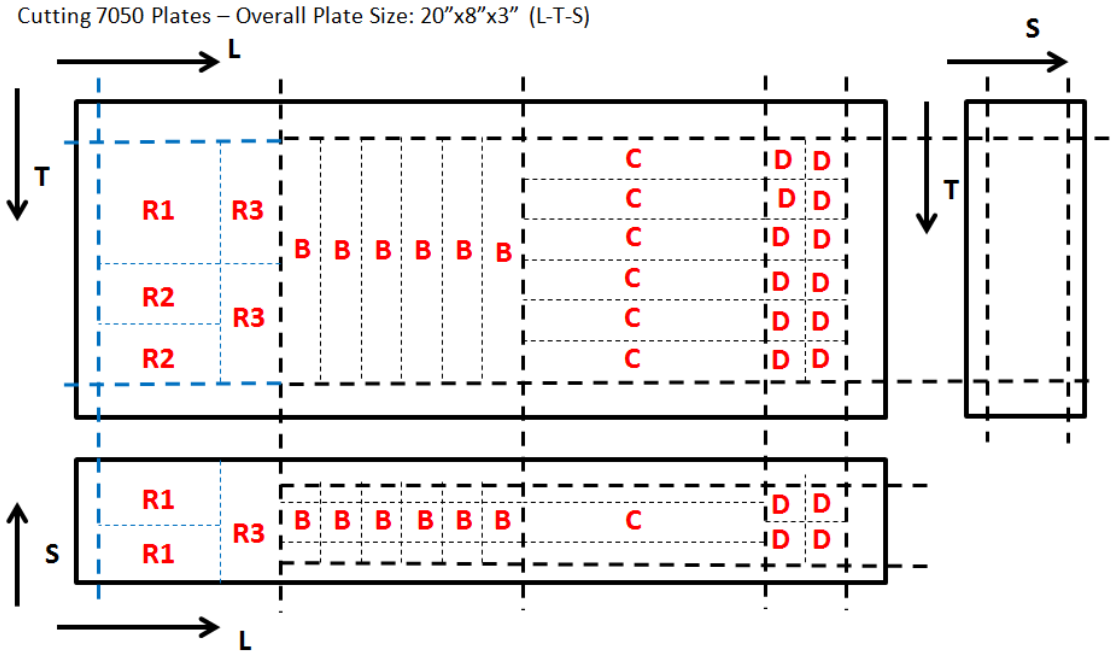

Letter	Size (L-T-S)	Quantity	ID #
R1	3”x 3” x 1.5”	2	XX-R1-Y (Y=1-2)
R2	3”x 1.5” x3”	2	XX-R2-Y (Y=1-2)
R3	1.5”x 3” x 3”	2	XX-R3-Y (Y=1-2)
B	1”x 6” x 1”	6	XX-B-Y (Y=1-6)
C	6”x 1” x 1”	6	XX-C-Y (Y=1-6)
D	1”x 1” x 1”	24	XX-D-Y (Y=1-24)
XX = Alpha-numeric of the plate (e.g. C1, A5)			
Size of R block – 4.5”x6”x3” Size of B block – 6”x6”x1” Size of C block – 6”x6”x1” Size of D block – 2”x6”x2”			
It is important to mark in pen each direction (L, T, and S) on every individual piece			

Figure 5.3: A schematic showing the location of the various test coupons within each plate.

Table 5.2: The allocated purpose of the various test coupons which were generated in this project.

Specimen ID	Purpose	Specimen ID	Purpose
XX-R1-1,2	Fracture toughness testing, maximum orientation	XX-R3-1,2	Held for future notched-specimen testing
XX-R2-1,2	Fracture toughness testing, minimum orientation		
XX-B-1,2,3	Tensile testing, transverse direction	XX-B-4,5,6	Held for future strength, fatigue or slow strain-rate testing
XX-C-1,2,3	Tensile testing, longitudinal direction	XX-C-4,5,6	Held for future strength, fatigue, or slow strain-rate testing
XX-D-1,2,3,4	Microstructure characterization	XX-D-7,..,24	Held for future microstructure characterization, indentation, or other testing
XX-D-5,6	Potentiodynamic Polarization Tests		

5.5 Summary

It was important that the processing routes that were explored for this project, which have been discussed here, be chosen to generate a wide variety of microstructures and mechanical properties. The aim of this project was not to try and pick or develop processing routes that would give improved or advantageous microstructure properties. This is a common problem with the way that studies currently designed in most academic work. Additionally, this work made every effort to ensure that the processing history of the material was consistent and uniformly applied, and that the resulting test coupons were independent of edge effects and other geometry considerations, by using single plates material from the same mill order that were each processed in a unique way before being sectioned into individual test coupons for microstructure characterization and mechanical properties testing. By accounting for both this variability in initial processing and by generating a wide variety of both good and bad processing routes, this work was able to generate materials samples which successfully varied a wide variety of microstructural features, including the extent of recrystallization, the recrystallized grain size, the subgrain cell size, the volume fraction and size of constituent particles, the size, spacing, and volume fraction strengthening precipitates in the grain interior, and the size, spacing, and composition of equilibrium particles located along the grain boundaries.

5.6 References

[1] J. R. Davis, editor. *Aluminum and Aluminum Alloys*. ASM International, 1993.

[2] ASTM International. B918: Standard practice for heat treatment of wrought aluminum alloys, March 2009.

[3] Scott MacKenzie. Heat treating aluminum for aerospace applications. In *4th International Conference on Quenching and the Control of Distortion*, 2003.

[4] N. M. Han, X. M. Zhang, S. D. Liu, D. G. He, and R. Zhang. Effect of solution

treatment on the strength and fracture toughness of aluminum alloy 7050. *Journal of Alloys and Compounds*, 509:4138–4145, 2011.

[5] L. Huang, K. Chen, and S. Li. Influence of grain-boundary pre-precipitation and corrosion characteristics of inter-granular pphase on corrosion bbehavior of an al-zn-mg-cu alloy. *Materials Science & Engineering, B: Solid-State Materials for Advanced Technology*, 177:862–868, 2012.

[6] Alcoa. Alloy 7050 plate and sheet, 2016.

CHAPTER 6

MICROSTRUCTURE CHARACTERIZATION

One aim of this work was to generate a large set of materials specimens in which many of the microstructural features were varied using the processing methods that were detailed in the previous chapter. In particular, based on the processing, the extent of recrystallization, the recrystallized grain size, the subgrain cell size, the volume fraction and size of constituent particles, the size, spacing, and volume fraction strengthening precipitates in the grain interior, and the size, spacing, and composition of equilibrium particles located along the grain boundaries, were all expected to vary across the different materials specimens. Because allowing all of these parameters to vary necessitates a large amount of materials characterization in order to measure the change in the different features across each specimen, it is important to evaluate the current and commonly available methods of characterizing these features, to determine their ability to scale to such large project sizes.

Based on current methods of characterizing some microstructural features, such as high resolution electron microscopy required to view the nanometer scale strengthening precipitates in the grain interior capturing the full microstructure characteristics of these specimens can present real challenges to the scope, time, and budget of projects. In fact, multiple issues can pose such scaling challenges, including the wide variety of length scales involved in the microstructural features of interest, the high number of images required to generate statistically robust quantitative measurements, as well as the need for different preparation procedures to observe different features in the microstructure. Therefore, it is advantageous to minimize the total number of images

required for characterization in whatever way possible, while still maintaining the full fidelity of the measurements that are collected. In this work, stereology principles were applied to minimize the number of images and specimens required to fully capture the anisotropic properties of the microstructure. This project also tried to limit the scope of the work by measuring multiple features of interest occurring at similar length scales with a single specimen preparation procedure, even when that procedure was not optimal for particular features. Even with these measures, this project still struggled at capturing and accurately measuring some of the microstructural features that were of interest.

6.1 Preparation

6.1.1 Cutting and Mounting

Microstructure characterization samples were taken from the 1"x1"x1" 'D' blocks, as detailed in Chapter 5. An abrasive cut-off saw was used to minimize the damaged layer while maximizing the efficiency of cutting. As discussed in the previous section, anisotropy was accounted for by preparing three specimen planes according to the trisector method. The LT (longitudinal-transverse) plane was taken as the 0 degree plane, since this is typically the preferred plane of imaging for most researchers who would observe the resulting work. The other two specimens were cut from blocks D-2 and D-3 at +120 and -120 degrees, respectively, from the LT plane using specially machined jigs, which held the rotated sample within the grips of the abrasive saw.

After cutting, samples were cold mounted in an epoxy and dried under vacuum to prevent the formation of bubbles and the interference of moisture. Cold-mounting was preferred in this application over hot-mounting, since hot-mounting usually requires temperatures of at least 120 °C. Even though the time at this temperature is short, usually only about 15 minute, exposure at these temperatures can artificially age the

material slightly. Cold-mounting does not expose the sample to elevated temperatures, and even though setting times can be long (up to 24 hours) it is relatively easier to prepare many samples at once. Therefore, cold-mounting was used to advantage in this application. Since the samples were conductive, no conductive filler was added to the epoxy mounting medium, though it is possible that this addition may improve the quality of high-resolution scanning electron microscopy images in the future.

6.1.2 Polishing

After mounting, samples were polished using an automated polishing wheel with a force head capable of polishing three specimens at once. The polishing procedure applied to all samples is detailed in Table 6.1. All polishing consumables were provided by Struers, and OP-S solution used in the final polishing step is a Linde-B sized silica oxide polishing suspension.

Table 6.1: Polishing procedure used in this work, with the assistance of an automated polisher and force head.

Cloth	Grit	Force (N)	Speed (rpm)	Time (min)
SiC Paper	220	15	300	Until plane
SiC Paper	320	20	300	6
SiC Paper	500	20	300	6
SiC Paper	600	20	300	6
SiC Paper	800	20	300	6
MD-Dac	9 um	20	300	6
MD-Mol	3 um	20	300	6
MD-Nap	1 um	20	300	6
MD-Chem	OP-S	20	300	6

The quality of polishing attained during these steps is critically important, since this

can impact the quality and usefulness of the images taken. Although hand-polishing procedures for the same material have been reported that contain less steps and less time, decreasing the grit size changes and increasing the time at each step is necessary to be able to automatically polish so many different samples. Automatic polishing greatly improves the repeatability and consistency of results, especially when so many samples are involved. However, the time required to polish the large number of samples required for this project can still make this a time consuming step.

After samples received the final polishing step, they were covered in a polyimide solder masking tape to protect the surface the surface from oxidation and scratching prior to being etched. Similar to the freeze hold used between heat-treating steps discussed in Chapter 5, this step improves the flexibility and ease of implementation of these preparation steps.

6.1.3 Etching

For many materials, certain aspects of the microstructure, such as grain boundaries or certain types of particles, are only observable after first applying an etchant to the polished surface. Etching is a method of corroding the surface in a carefully controlled way to increase the relief between two different aspects of the material, and results from the electrolytic action between surface areas of different potential. [1]. While standard chemical etching solutions are most commonly used, other methods such as anodizing and electrolytic and potentiostatic etching methods exist and can also be applied.

Because different etchants attack different aspects of the microstructure and offer relief and observability in different ways, etchants are often highly optimized for a particular feature or type of feature. Therefore, some etchants are designed to reveal

grain boundaries in a particular type of material, while others are specifically designed to reveal carbides. Therefore, the characterization of different microstructural features may require samples to be polished and etched differently.

In this work, two different etchants were primarily used. One etchant, a Graff-Sargent etchant consisting of 3g of CrO_3, 0.5mL of HF, 15.5mL of HNO_3, and 84 mL of deionized water, was used to reveal grain and subgrain boundaries in the material. Samples were immersed in the etchant for 60 seconds with mild agitation and then were imaged in an Olympus optical light microscope at multiple resolutions to determine the extent of recrystallization, the recrystallized grain size, and the subgrain cell size. Additionally, this etchant was also successful at revealing coarse particles along the grain boundaries, dispersoids, and coarse constituent particles in the recrystallized grains. Some representative examples of the optical images that were obtained are shown in Figure 6.1, and all optical images collected are available in the associated data repository.

The other etchant that was primarily used in this work was a highly modified Keller's reagant consisting of 0.5g of NaF, 1mL of HNO_3, 2mL of HCl, and 97mL of deionized water. Samples were first immersed in 25% aqueous HNO_3 at 70°C for one minute, washed, and then immersed it in the modified Keller's reagant for one minute, washed, and dried. This etching procedure was design to reveal the strengthening precipitates within the grain interior. Since these precipitates can be extremely small (a few nanometers), it is common to examine both these and the equilibrium grain boundary precipitates in a transmission electron microscope (TEM). However, TEM access is typically limited to only large research institution or national lab facilities and can be extremely expensive. Additionally, TEM imaging requires difficult and specialized preparation and equipment which is not commonly available and takes much time

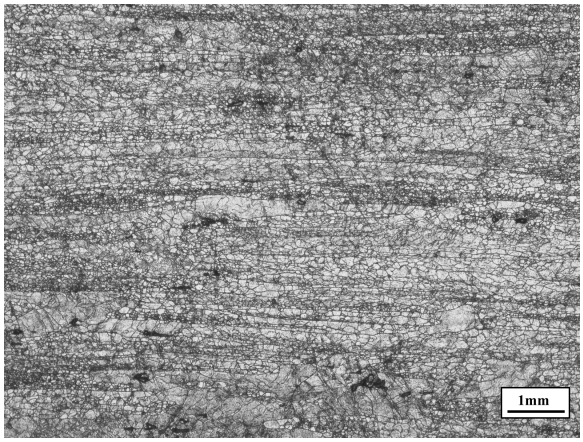

(a) C2 at 100X

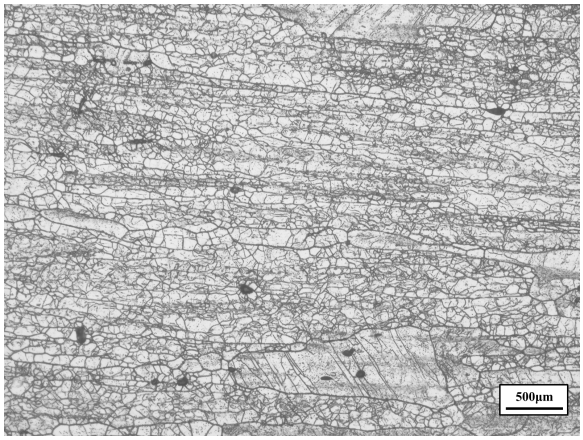

(b) D2 at 200X

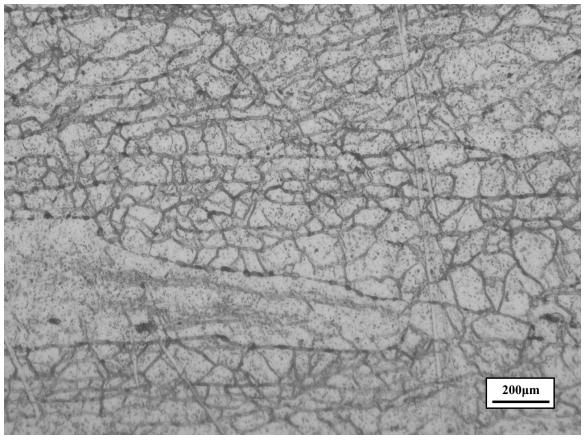

(c) A1 at 500X

captionsetupjustification=centering,margin=0.5cm

Figure 6.1: Representative optical images after immersion in Graff-Sargent etch at 100X, 200X, and 500X, respectively.

to because familiar with. Therefore, high resolution scanning electron microscope (SEM) images were taken in this work instead.

6.2 Results and Analysis

6.2.1 Grain Structure Characteristics

Measurements of the grain size are widely recognized as being critically important to the understanding of a material and its mechanical properties. Standard methods exist and are managed by ASTM International to encourage and promote methods that can provide a consistent and quantitative measurement of the grain size for different materials. The most robust measurement recommended by ASTM is detailed in ASTM E112, and involves laying strain lines of a prescribed size over the microstructure and counting the number of times a grain boundary intersection with that line to generate a mean intercept grain size. This mean intersect grain size, $\bar{L}$ or $\bar{L}_{eff}$, where

$$\bar{L}_{eff} = \frac{1}{\langle P_L \rangle} \tag{6.1}$$

and $\langle P_L \rangle$ is the average number of the grain boundary intersections with the lines. ASTM E112 recommends that these intersection measurements are made on three to five blindly selected and widely separated fields of view, to obtain a reasonable average for the specimen observed. However, if this average doesnt show the necessary precision specified in the standard, the number of measurements must be increased indefinitely. Additionally, any moderate departure from an isotropic and equiaxed grain structure necessitates additional measurements on lines have four or more orientations. And further anisotropy, such as that occurring in rolled or worked structures, requires specimen planes of at least three orientations to be examined[2]. Therefore, while the ASTM standard does serve to promote and encourage the quantitative measurement of the grain structure, it gives only vague instructions on how to do so efficiently for highly anisotropic materials such as those examined here.

The introduction of stereological principles here can therefore be of much help, by providing solid recommendations on how to segment and measure the material in such a way as to obtain the necessary precision indicated in ASTM 112 quickly and efficiently. Much work has already been done showing that intersection measurements made with cycloids, rather than straight lines, on planes oriented according to either the vertical plane sectioning principle or the trisector principle, can provide accurate measurements with as few as 25 images [3, 4, 5, 6]. This work utilized the trisector method, detailed elsewhere, with the longitudinal direction chosen as the vertical direction [3, 4, 6].

Therefore, the recrystallized grain size was estimated in this work by measuring the points of intersection between the cycloid and the recrystallized grains per cycloid line length to generate P_L. The P_L measurements for each image examined where then averaged to calculate $\langle P_L \rangle$ for the entire material, which was used to calculate the mean intercept grain size. These results are summarized in Table 6.2, below, will full results located in the associated data repository.

This material is further complicated by the presence of two different grain-sized regions. In addition to measuring the recrystallized grain size, it was also necessary to measure the percent of recrystallization and the grain size of the sub-grain cell structures. In this work, the volume fraction of recrystallized grains was measured by point counting. This method is detailed in ASTM 1181 and widely used. It generally involves laying a grid over the microstructure and counting the number of points in the grain that fall inside features of interest. If the total number of points is of the same order of magnitude or greater than the number of features of interest, then the average fraction of points that fall within those features, $< P_P >$, is equivalent to

Table 6.2: The average recrystallized grain size for the various specimens characterized in this work.

Specimen	Average (μm)	St Dev (μm)	Specimen	Average (μm)	St Dev (μm)
A1	338.37	15.61	C3	357.50	16.56
A2	362.13	17.34	D1	374.56	19.10
A3	362.29	15.28	D2	369.58	18.48
A4	361.59	17.19	D3	355.46	18.40
A5	361.04	16.75	D4	386.98	17.75
B1	445.92	25.28	D5	362.32	19.31
B2	357.20	15.49	E1	374.15	18.84
C1	395.06	19.65	E2	425.06	27.38
C2	382.52	16.21	E3	422.76	22.76

the volume fraction of the feature within the material, V_V [6, 7]. These results are summarized in Table 6.3.

Table 6.3: The extent of recrystallization measured for the various specimens characterized in this work.

Specimen	Average (%)	St Dev (%)	Specimen	Average (%)	St Dev (%)
A1	20.49	2.47	C3	20.10	2.42
A2	21.05	2.27	D1	20.10	2.36
A3	29.43	2.52	D2	17.50	2.00
A4	24.74	2.43	D3	24.81	2.68
A5	23.93	2.60	D4	19.90	2.79
B1	18.81	2.27	D5	20.38	2.34
B2	14.19	1.63	E1	31.77	3.24
C1	22.62	2.40	E2	28.93	2.81
C2	17.83	2.40	E3	36.55	4.19

The sub-grain cell size was measured using the same principle and equations applied to the recrystallized grain size. However, for these measurements cycloids were placed only within unrecrystallized regions as opposed to being systematically spaced throughout the image as done for the recrystallized grain size measurements. These results are summarized in Table 6.4.

Table 6.4: The average subgrain cell size for the various specimens characterized in this work.

Specimen	Average (μm)	St Dev (μm)	Specimen	Average (μm)	St Dev (μm)
A1	42.15	2.21	C3	39.93	1.92
A2	47.86	2.25	D1	46.88	2.25
A3	46.75	1.94	D2	45.02	1.85
A4	47.60	2.97	D3	39.46	1.63
A5	45.44	2.08	D4	48.48	2.40
B1	56.12	4.04	D5	50.21	3.20
B2	46.72	2.23	E1	50.43	2.78
C1	54.04	6.41	E2	62.93	4.32
C2	49.27	2.69	E3	63.46	4.35

Although the volume fraction of the two regions and their different grain sizes were measured, this work did not attempt to measure the texture of the material. Since all materials tested in this work were rolled plate product, and no additional working was applied to the materials during processing, the effect of texture was considered here to be constant. However, the characterization and quantification of texture is still important if the model developed from the experimental data is expected to capture the effects of different plastic deformation processes as discussed in Chapter 1.

6.2.2 Constituent Particles

Since constituent are convex particles dispersed in the matrix of the material, measurements of their size and volume fraction can theoretically be made quite easily. The volume fraction of these particles can be measured using the point counting method, since

$$V_V = \langle P_P \rangle \,. \tag{6.2}$$

Most experimental studies measure the average size of a class of particles by measuring the diameter of the cross section of the particle that is observed in the sectioned image. However, while this method does produce a quantitative measurement, it is not a measurement that is statistically accurate. First, this method, even when it involves averaging many such measurements, does not distinguish between two different possible reasons for the variation of observed diameters. The first potential reason for this variation is because the three-dimensional particles that are suspended in the material are simply different sizes, and possess different average diameters. The second potential reason is that the particles that are suspended in the material are all sectioned at different depths. Meaning the that diameter of the cross section observed is not a true three-dimensional diameter, but rather a segment that simply fits within the three-dimensional particle with an unknown orientation. Typically, both types of variation exist within the material, but their relative contributions cannot be realized because the method in question cannot distinguish between them.

A much better method of the average size of the particles is the surface area weighted caliper diameter, which is calculated using[6]

$$\langle D \rangle = \frac{6V_V}{S_V} \tag{6.3}$$

Where V_V is the volume fraction of the particles, and S_V is the average surface area per unit volume of the particles within the material. This value, S_V, can be calculated

from P_L using the cycloid intercept method described in detail above by

$$S_V = 2\langle P_L \rangle . \tag{6.4}$$

Although this is a good measure of the average size of the particle class in question, it does not give any information about the spacing of the particle class, particularly when particles occur in clusters, and constituent particles often do.

Additionally, while we can use this method to understand the average constituent particle size within the material, this may not be the most useful measurement to take. Since constituent particles are typically of interest as the source for crack initiation in the material, and since the stress required to initiate a crack is inversely related to the size of the particle, perhaps a more useful measure of the constituent particle size would be the likely maximum particle size. In addition to calculating the average values discussed above, it is also important to calculate and report the various errors associated these measurements. One of these error, the variance of the sample, is given by

$$S^2 = \frac{\sum \left[\langle \bar{P} \rangle - P_i\right]^2}{(N-1)} \tag{6.5}$$

Assuming that the microstructural feature being examined has a Gaussian distribution, then we can use this variance to calculate the standard deviation associated the with distribution function.

$$\sigma = \sqrt{\frac{S^2}{N}} \tag{6.6}$$

Using both the average and the standard deviation we can plot the density function that is associated with the microstructural feature being characterized, which is given by

$$f(x) = \frac{1}{\sigma\sqrt{2\pi}} exp\left[\frac{-1}{2}\left(\frac{x-\mu}{\sigma}\right)^2\right] \tag{6.7}$$

where μ is the average and σ is the standard deviation. We can then define a "maximum likely particle size" present in the material by taking the 95% tail value of this

distribution, which is given by

$$D_{max} = \mu + 1.96\sigma \tag{6.8}$$

The calculated values for the volume fraction of the constituent particles, their average caliper diameter, the resulting max likely particle size are presented in Table 6.5.

Table 6.5: The constituent particle size and volume fraction for the various specimens characterized in this work.

Specimen	Vol Fract (%)	St Dev (%)	Avg Size (μm)	St Dev (μm)	Max Size (μm)
A1	2.38	0.28	18.69	11.79	41.80
A2	0.93	0.17	32.04	10.33	52.29
A3	0.81	0.15	25.97	10.33	46.22
A4	1.10	0.18	37.44	11.26	59.50
A5	1.14	0.19	39.81	15.50	70.19
B1	0.67	0.15	46.89	18.72	83.58
B2	0.52	0.12	29.94	10.46	50.44
C1	0.50	0.12	33.25	11.55	55.89
C2	0.60	0.13	45.36	16.27	77.24
C3	0.64	0.13	39.19	11.30	61.34
D1	0.55	0.13	32.31	13.11	58.01
D2	0.62	0.13	34.83	11.03	56.46
D3	0.76	0.17	59.29	20.44	99.35
D4	0.40	0.11	24.67	10.36	44.98
D5	0.60	0.12	36.29	12.74	61.26
E1	1.00	0.23	58.06	24.59	106.26
E2	0.83	0.14	58.62	15.48	88.95
E3	0.45	0.11	35.97	11.92	59.33

6.2.3 Grain Interior and Grain Boundary Characteristics

As discussed in Chapter 3, the volume fraction, average size, and the spacing of precipitates, both in the bulk and along the grain boundary, are all critically important

to understanding the linkage between the microstructure and the mechanical properties. For strengthening precipitates in the bulk of the grain these measurements are fairly straightforward. The volume fraction of these particles can be easily calculated using the point counting method, and the surface area weighted caliper diameter can be calculated using similar methods. Quantitative measurements of the dispersion, however, have not yet been addressed. Recall that the dispersion of these precipitates is important because their spacing controls their ability to trap dislocations and generate a strain field, which produces a hardening effect. Therefore, the most useful measurement of the dispersion is perhaps the average mean-free path between the particles. This distance can also be easily calculated from the $< P_P >$ and $< P_L >$ measurements already used, and is given by[6]

$$\lambda_{bulk} = 4\frac{(1 - V_V)}{S_V}. \tag{6.9}$$

Measurements concerning the equilibrium precipitates along grain boundaries are nearly as straightforward. Where grain bulk particles have an average mean-free path between them that is randomly oriented in all three dimension, these equilibrium particles are constrained to grain boundaries and have a mean free path that exists only along the plane of the grain boundaries they reside in. Therefore, when taking the surface area per volume measurements for the grain boundary particles, it is important to use the grain boundaries themselves as the lines to calculate the interception points[6].

Despite the information discussed in Chapters 2 and 3, the chemical composition of the grain boundary precipitates was not a part of the microstructural characterization done here. Instead, this work attempted to capture the influence of the grain boundary chemistry on the corrosion rate through various parameters calculated from the potentiodynamic polarization curves, discussed in Chapter 9.

Unfortunately, most of the high resolution SEM images that were taken in this work were unusable for analysis of these precipitates. Since TEM imaging is far more common as a characterization tool, most published work in this area only details TEM specific preparation methods, which usually involve electropolishing for polishing and etching. Since HRSEM was attempted instead to try and reduce the cost of the work involved, specimens instead had to be prepared different with the highly modified Keller's reagant that was discussed earlier. Unfortunately, this etchant was found to be extremely difficult to apply to all of the varied samples in an optimum way, resulting in many of the specimens appearing "over-etched" and not producing usable images. It's also possible that other issues associated with the lack of experience in this etchant contributed to the poor quality of images obtained here. When the etchant was applied in a way that produced visible images, the particles of interest were often not able to be captured on an appropriate length scale, due to resolution limitations.

In the future, it is recommended that TEM images are used to directly view the precipitates within the grain interior and at the grain boundary. Unfortunately, taking 25+ images using systematic sampling methods for each specimen can quickly increase the scope of the work to unreasonable levels. Additionally, both SEM and TEM imaging methods do not allow for the characterization of the composition of precipitates either in the interior of the grain or along the grain boundary. Therefore, it is recommended that TEM imaging be combined with other methods of characterizing these particles, perhaps with indirect methods such as resistivity curves like those shown in Chapter 2.

6.3 Summary

Although characterizing the full microstructure is critical to understanding the complex underlying physical relationships between processing parameters and final mechanical properties, full quantitative characterization is a time-consuming and expensive undertaking. Due to the number of different length scales involved, the need for statistically accurate quantitative measurements, and complications such as different etching requirements for different characteristics to be observed it is necessary to do an extraordinary amount of imaging to fully capture the microstructure characteristics, and it may be best to obtain this information is a variety of different ways to completely characterize each feature of interest.

In this work, different steps were taken to try and mitigate the time and number of images required. At larger scales, preparation and imaging procedures were optimized to take high quality optical images, which could be used to calculate statistically accurate measurements of the recrystallized grain size and volume fraction, as well as the sub-grain cell size. These images were then re-used to characterize the constituent particles without changing the etchant and therefore without requiring the samples to be re-prepared and imaged a second time. At smaller length scales, the polishing procedure and the etchant were optimized for precipitate imaging. However, the variation in the size and chemical composition of grain boundary precipitates in the different samples made universally applying an optimized etching procedure nearly impossible. Additionally this work attempted to use a minimal number of high-resolution SEM images, rather than relying on more standard TEM techniques that are time-consuming and expensive, to characterize precipitate features. As a result, images and measurements of these microstructure aspects are of a significantly lower quality than those taken for the grains, and ultimately measurements from these images were unavailable. In the future, it is possible that combining multiple methods

of characterization, such as TEM imaging and indirect methods such as resistivity curves, may be the best approach.

However, there are other improvements that could be made to help ease this process mostly surrounding the automation of various processes. Automatic polishing machines can improve the quality of the preparation, and automatic stages and image capturing software can cut down the machine time. Even though such improvements are usually considered to be minor on a single specimen basis, these savings can add up significantly as large scales such as those seen here. The biggest time and cost savings opportunity is in the automation of image processing. While there is image processing software that can accomplish some of these, many of them are still beyond current capabilities, which are not reviewed here.

6.4 References

[1] George F. Vander Voort. *Metallogrpahy Principles and Practice*. McGraw-Hill, 1984.

[2] ASTM International. E112: Standard test methods for determining average grain size, October 2013.

[3] B. R. Morris, A. M. Gokhale, and G. F. Vander Voort. Grain size estimation in anisotropic materials. *Metallurgical and Materials Transactions A: Physical Metallurgy and Materials Science*, 29A:237–244, 1998.

[4] A. M. Gokhale and W. J. Drury. Efficient measurement of microstructural surface area using trisector. *Metallurgical and Materials Transactions A: Physical Metallurgy and Materials Science*, 25A:919–928, 1994.

[5] A. M. Gokhale, N. U. Deshpande, D. K. Denzer, and John Liu. Relationship between fracture toughness, fracture path, and microstructure of 7050 aluminum alloy: Part ii. multiple micromechanisms-based fracture toughness model. *Metallurgical Transactions A*, 29A:1203–1210, 1998.

[6] A. M. Gokhale. personal communication, 2012.

[7] ASTM International. E1181: Standard test methods for characterizing duplex

grain sizes, October 2015.

CHAPTER 7

TENSILE STRENGTH TESTING

Test coupons from the different plates were subjected to ASTM standard tensile testing in order to assess the tensile strength properties, including: yield strength, ultimate strength, hardening behavior, and ductility. This chapter will discuss the details of machine and test set up, the designing and machining of test specimens, the details of the test itself, and the post-processing and analysis of the data. Again, the aim of the project was to produce test specimens that possessed a wide variety of tensile strength properties, and to examine the ease and feasibility of measuring these properties using commonly available mechanical testing methods.

7.1 Specimen Preparation

Tensile test specimens were machined from the 1"x1"x6" 'B' and 'C' series test coupons. As discussed in Chapter 5, three 'B' coupons (XX-B-1 through XX-B-3) oriented in the transverse direction and three 'C' coupons (XX-C-1 through XX-C-3) oriented in the longitudinal direction were used for tensile tests. Therefore, 108 tensile tests were conducted in total. Tensile tests that were machined from these coupons were designed according to the guidelines laid out in ASTM Standard B557-10, shown in Figure 7.1, which is the standard method for tension testing of wrought aluminum alloy products.[1]

For this work, small-sized specimens which were proportional to the standard with a gauge diameter of 0.250 inches were used. Drawings for these specimens can be found in the associated data repository.

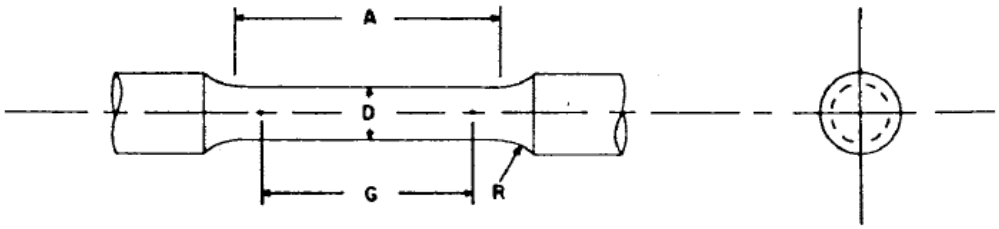

Nominal Diameter	Dimensions, in.	
	Standard Specimen	Small-Size Specimen Proportional to Standard
	0.500	0.250
G—Gage length	2.000 ± 0.005	1.000 ± 0.005
D—Diameter (Note 1)	0.500 ± 0.010	0.250 ± 0.005
R—Radius of fillet, min	3/8	3/16
A—Length of reduced section, min (Note 2)	2¼	1¼

Figure 7.1: The standard cylindrical tensile test coupon recommended by ASTM.

7.2 Machine Set Up and Testing Procedures

Samples were tested on a Materials Testing Systems (MTS) servo-hydraulic test frame outfitted with a 22kip load cell. The specimens were held by the machine through the use of cylindrical hydraulic grips fitted with 0.5" collets. In these tests, 4000psi of pressure was used to grip the specimens in place to prevent slipping. Strain was measured using a 1" gage MTS Model 632.31E-24 extensometer. As directed by ASTM B557-10, tests were displacement-controlled at a strain rate of 10^{-3} in/in until the material failed. Due to the max clip gage range, each test was paused between 9% and 10% strain and the clip gage was quickly removed to avoid any stress relaxation that may occur, before resuming the test. The remaining strain data after 9% was calculated from the crosshead displacement, as discussed in the next section.

7.3 Data Processing

Raw data collected directly from the test controller included the time, global crosshead position, the load measured, and the percent strain measured by the extensometer at each time step. Data for these tests were collected at 10Hz, which provided sufficient

resolution for analysis, and resulted in relatively small data files containing approximately 2000 data points or less. Post-processing of the raw data in to stress-strain curves and the extraction of yield strength, ultimate strength, ductility, and various work hardening parameters was all done in Matlab. Full scripts used in this analysis are included in the associated data repository.

For each test, the load measurements were converted to stress at each time point using the specified 0.250" gage diameter for simplicity. However, gathering measured values in to an excel spreadsheet to be read in by the batch processing code is an easy automation. While this level of fidelity was not deemed necessary for this test, this automation technique is demonstrated in the post-processing analysis of fracture toughness specimens, discussed in Chapter 8.

The elastic modulus was calculated for each specimen by taking the average ratio of the stress and strain data during the first 50 time steps, but only if the data in this region showed a linear correlation fit greater than 95% with a confidence under 5%. No samples were tested that were not found to meet this condition. This elastic modulus was used to calculate the 0.2% yield strength. The ultimate strength was simply the maximum stress measured during the test, and the ductility was similarly the maximum strain measured. One word of caution in the calculation of the ductility measurement, however, should be noted. At the end of the test when the material fails, one or two data points are occasionally recorded after the material has broken, but before the clip gage disengages from the material. This results in an artificially high strain, usually by about .5% during this last data point. These false data points can be identified by a significantly lower or even negative corresponding stress value. While this should not greatly alter the meaningful interpretation of the results as discussed here, it is important to be aware that this phenomenon can occur.

7.4 Results and Analysis

7.4.1 Yield Strength and Ultimate Strength

The average yield strength for the various processing routes in both the transverse and the longitudinal direction are shown in Figure 7.2. As seen in the graph, a variation in yield strength of just over 150 MPa was achieved. The slightly over-aged specimen C2 measured the highest yield strength, at 552MPa in the longitudinal direction, closely followed by some of the retrogression and re-aging samples, and the high temperature pre-precipitation processed A5 measured the lowest yield strength at only 393MPa in the longitudinal direction. Since many of the processing routes that were examined in this work were modeled after work that was reported in the literature, we can compared these results to those that were previously reported and see that the measurements found here are in good agreement.

In addition to generating a good variation in yield strength, the specimens also generated a good variation in the anisotropy. The percent change in the yield strength values with direction varied from 0.10% for the high temperature pre-precipitation processed sample, A5, to 5.61% for the interrupted treatment E1. The percent change in yield strength, ultimate strength, and ductility with direction, which serve as a measure of the relative anisotropy of the mechanical properties of interest, are shown together in Figure 7.9. Since the relative directionality of mechanical properties is important to fully characterizing the materials design space, it is important that the mechanical testing method can capture this variation.

The average ultimate strength values that were measured during tensile testing are shown in Figure 7.3, in both the longitudinal and the transverse directions. Similar to the yield strength values, significant variation in the ultimate strength was achieved

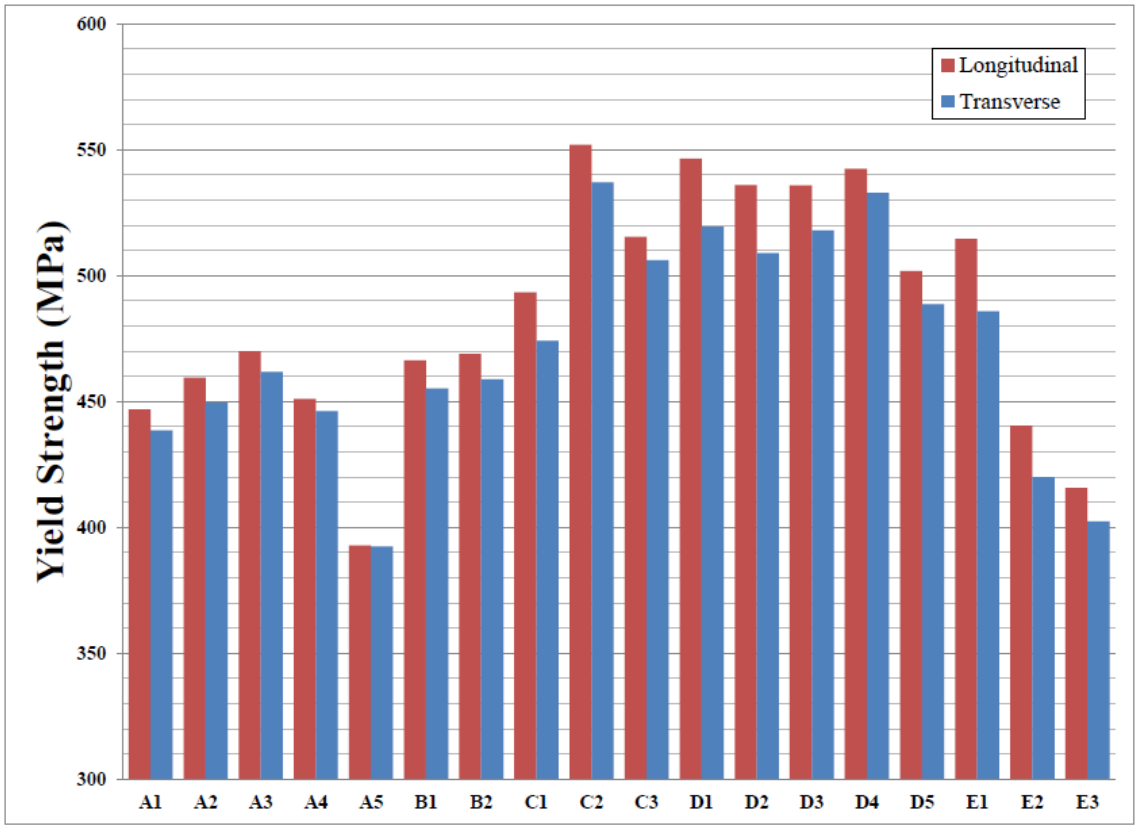

Figure 7.2: The yield strength measured in both the longitudinal and transverse directions for all specimens.

across the different specimens, and these values continue to agree with those previously reported. The highest ultimate strength, unsurprisingly, was measured in the peak-strength conditioned sample D2, at 627MPa. The lowest ultimate strength measured was 469MPa, also observed in the high temperature pre-precipitation processed A5. The variation in anisotropy observed also varied from 0.59% in A5 to 4.63% and 4.66% in the interrupted treatments E2 and E3, respectfully.

Since similar ranges for yield strength, ultimate strength, and their relative anisotropies were observed, it would be expected that the same samples that exhibited high anisotropy in yield strength also exhibited a high anisotropy in ultimate strength. However, a thorough examination of Figures 7.9 and 7.4 show that this not the case.

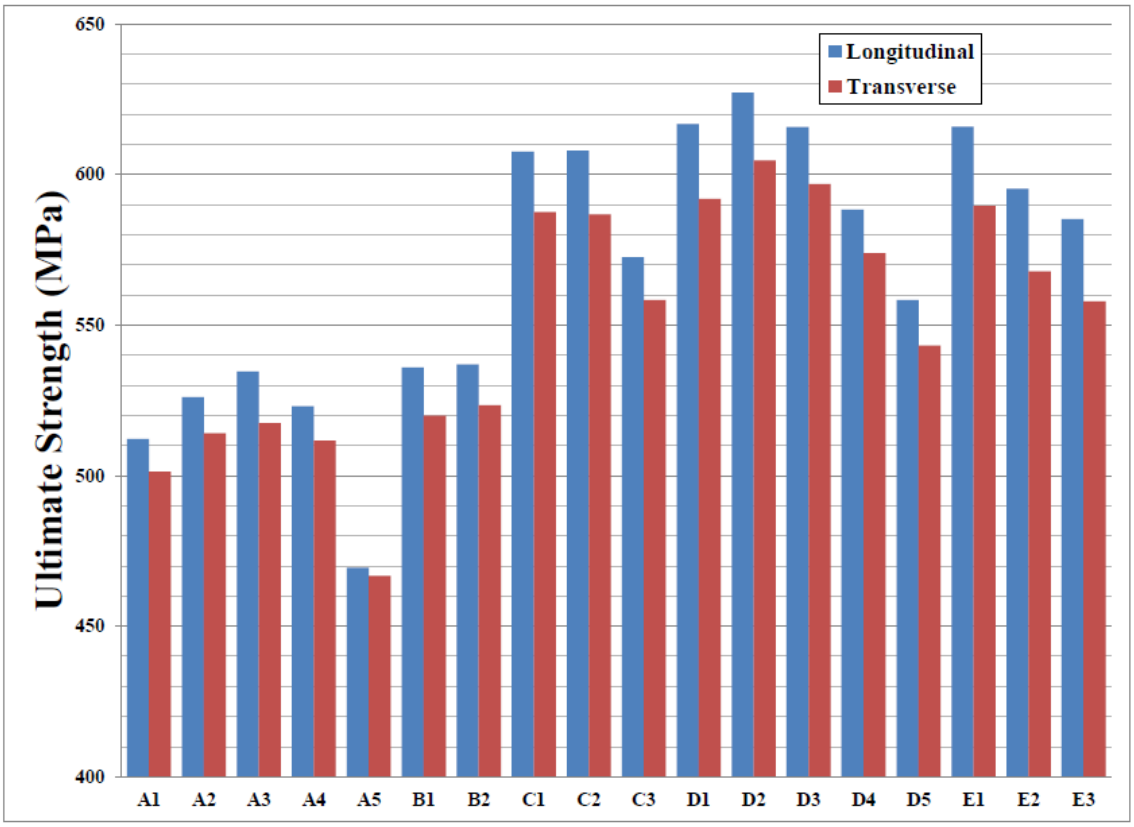

Figure 7.3: The ultimate strength measured in both the longitudinal and transverse directions for all specimens.

Some samples which showed a relatively low yield strength, such as E2 and E3, showed high ultimate strength values. And some samples, such as A3, that showed a small change in yield strength with direction, showed a significantly higher change in ultimate strength with direction.

These changes in the yield and ultimate strength properties indicate that the samples also showed a variety of work hardening behavior, including samples that showed a directional work hardening preference. This fluctuation in the work hardening behavior also shows the importance of allowing multiple microstructural features to fluctuate simultaneously in order to capture a variety of interactive effects and physical mechanisms that might be occurring within the system.

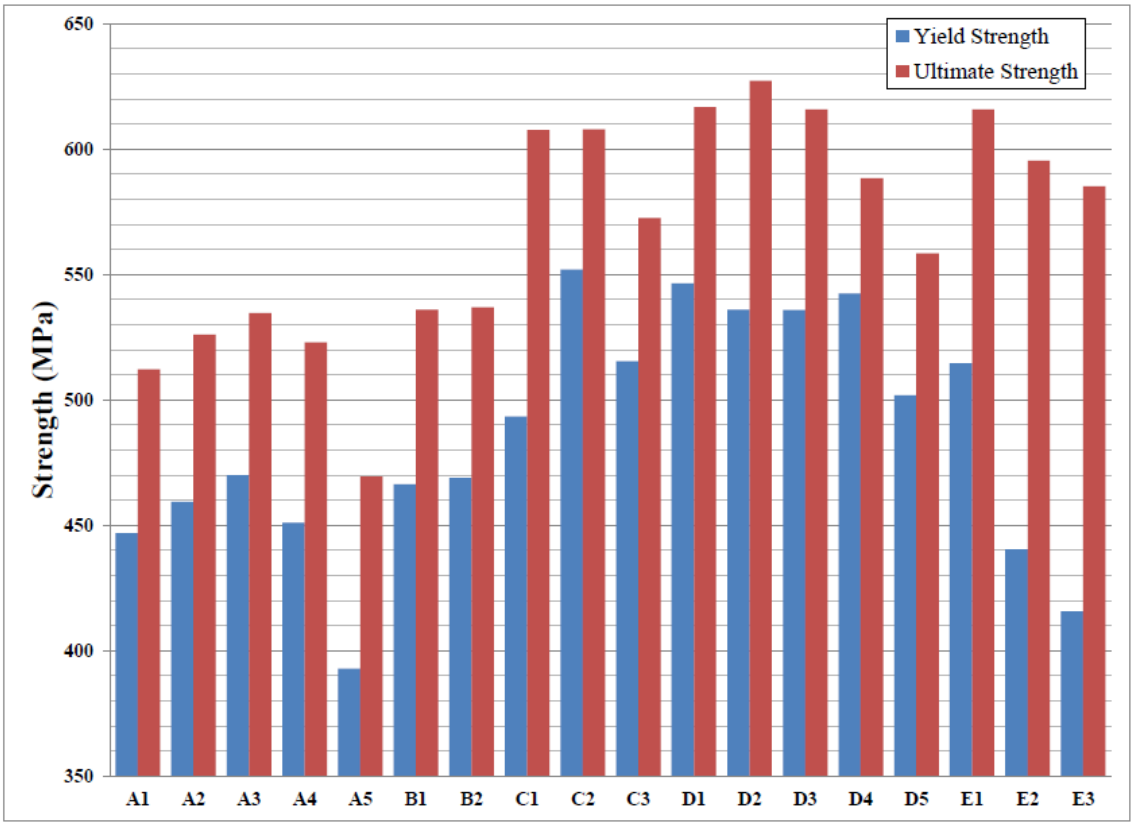

Figure 7.4: The yield and ultimate strength values measured in the longitudinal direction for all specimens.

7.4.2 Work Hardening

There are many ways, both qualitatively and quantitatively, to measure the work hardening. The first and most simple way of measuring work hardening is to measure the difference between the ultimate strength and the yield strength of the material. This difference, which can be observed clearly in Figure 7.5 below, can give an easily calculated quantitative measure that indicates the potential for the material to harden during plastic deformation. However, what is not included in this measurement is the amount of strain the material will undergo during that hardening, which is important for understanding the physical mechanisms which drive the behavior.

Figures 7.6-7.8 show some representative tensile test curves of the various samples

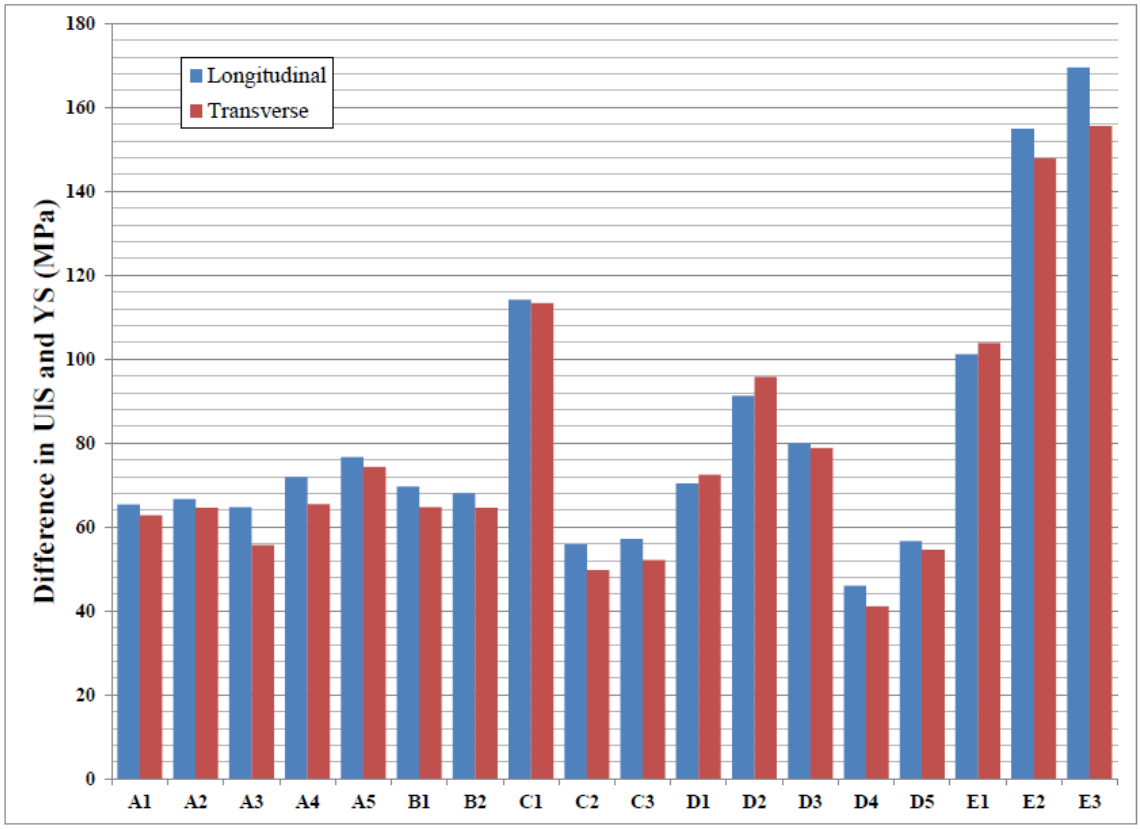

Figure 7.5: The difference between the yield strength and ultimate strength values for each specimen, one method of measuring the work hardening.

and the types of hardening behavior that were observed. All tensile test curves can be found in the associated data repository. In those samples that showed significant work hardening behavior, such as C1, D2, E1, E2, and E3, the tensile curves show this hardening occurring in a roughly linear fashion, with little to no necking occurring after the ultimate strength is reached.

Samples that show a minimum amount of work hardening, including D4, C2, and C3, all show a very flat curve following the yield strength. In fact, these materials behave very nearly like an idealized elastic-perfectly plastic material.

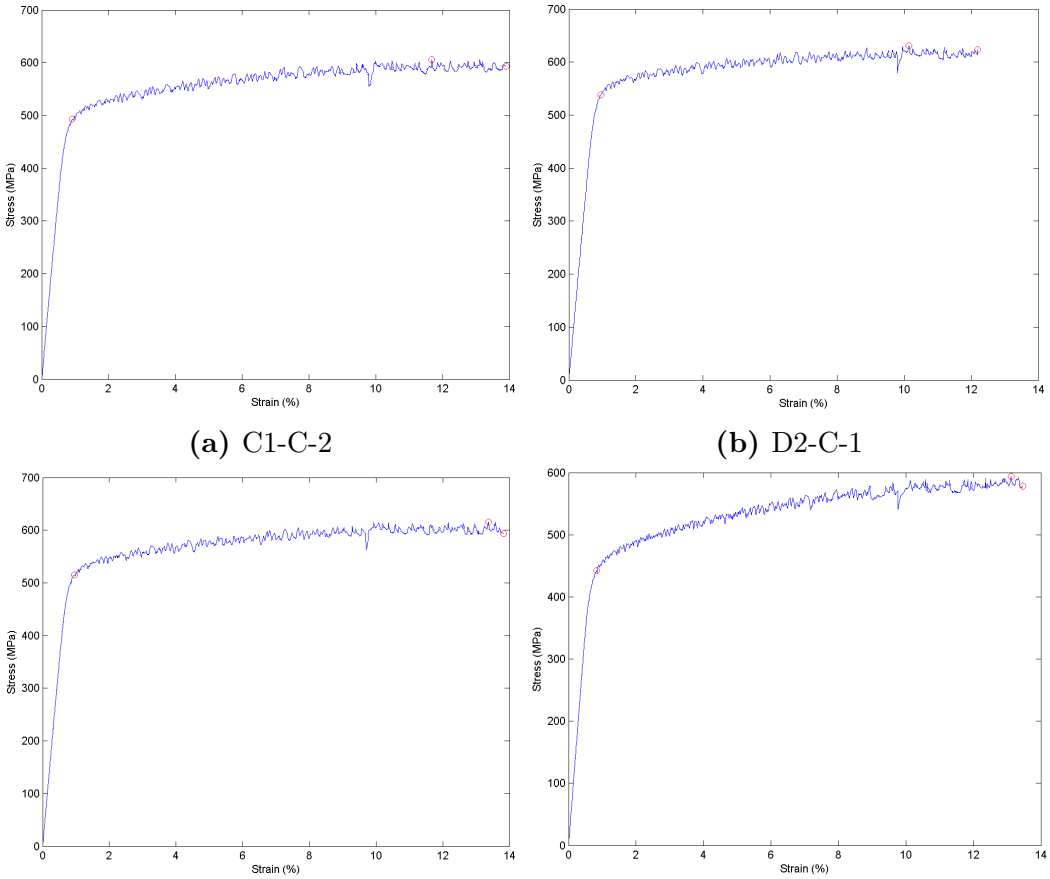

(a) C1-C-2 **(b)** D2-C-1

(c) E1-C-2 **(d)** E2-C-1

Figure 7.6: A set of representative tensile curves that show significant amounts of work hardening.

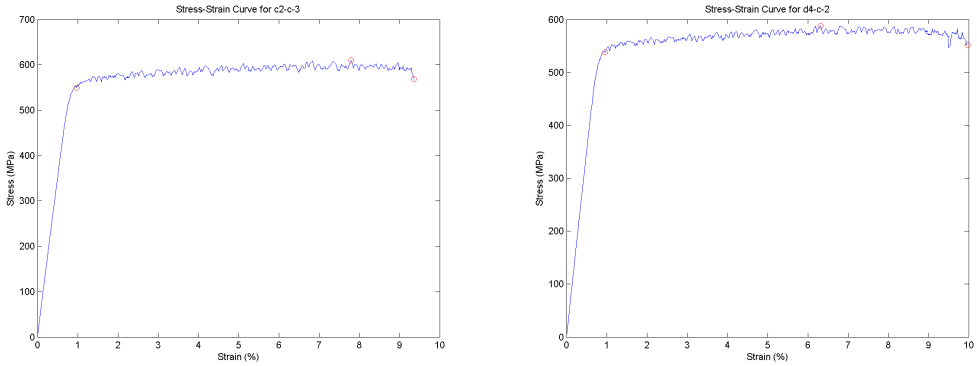

(a) C2-C-3 **(b)** D4-C-2

Figure 7.7: A set of representative tensile curves that show a minimal amounts of work hardening.

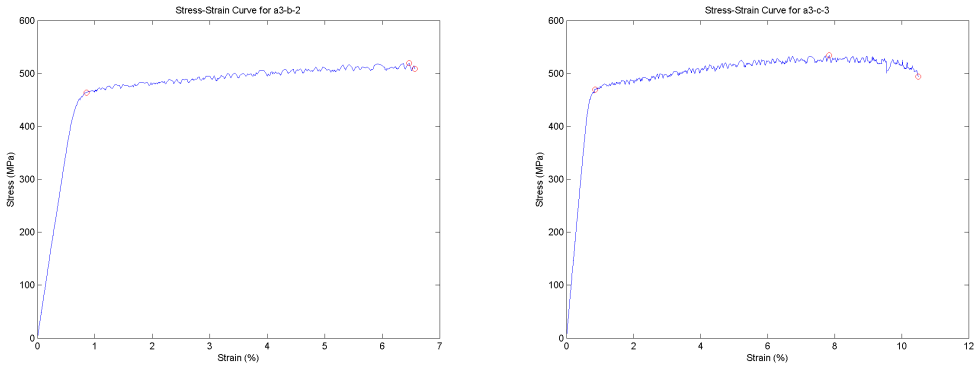

(a) A3-B-2 **(b)** A3-C-3

Figure 7.8: Tensile curves that show the strong directionality of work hardening in the A3 sample.

There are also those samples that show an increased amount of work hardening in one direction. In the case of A3, significantly more work hardening is observed in the longitudinal direction than in the transverse direction, by as much as 14%. The tensile curves for this material in both directions can help explain this difference. In the longitudinal direction the material exhibits greater overall ductility, which leads to an increased amount of work hardening before leveling off as the material approaches the ultimate strength. Only a small amount of necking is observed before the material fractures at 10.5% strain, compared to the 6.5% strain that is achieved in the transverse direction. Indeed, in Figure 7.9, the A3 sample shows the greatest relative change in ductility with direction.

Other samples that show a high amount of directionality in work hardening also have relatively high levels of anisotropy with respect to ductility, suggesting that one reason for this directionality may be a lack of ductility which promotes the failure of the material before higher potential stress values can be achieved. But not all samples that show high directionality in ductility have directional work hardening behavior, once again showing the importance of allowing multiple variables to fluctuate in the system in order to observe the interaction of different physical mechanisms.

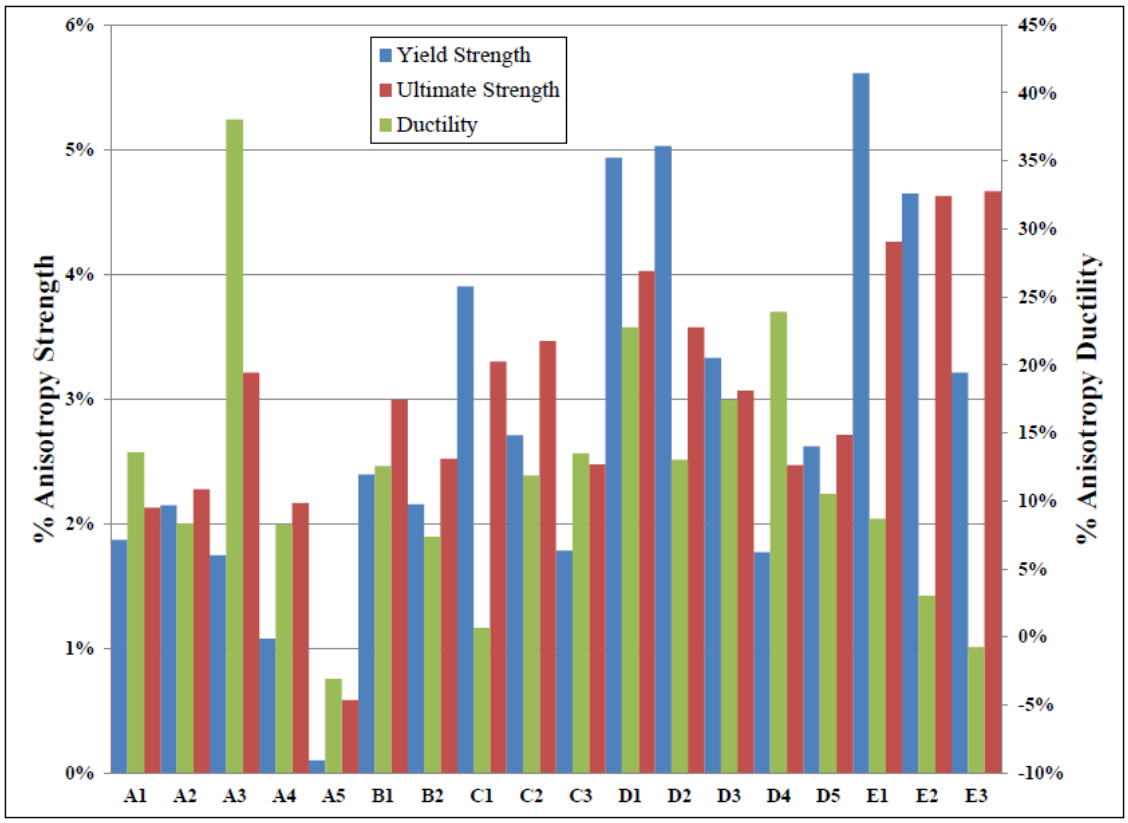

Figure 7.9: Caption text.

It is clear then that the relative amount of strain that the material undergoes while is hardens is clearly an important aspect of any measure of work hardenability. One option is to fit the data to a phenomenological hardening model, such as the Ramberg-Osgood equation

$$\varepsilon = \frac{\sigma}{E} + K\left(\frac{\sigma}{E}\right)^n \tag{7.1}$$

where K and n describe the hardening behavior of the material. However, given the qualitative observation that the samples behave like a mix between elastic-perfectly plastic materials and elastic-linearly strain hardened materials, is perhaps more appropriate to define an effective linear hardening rate in an idealized mixed-model. Figure 7.10 shows a simple schematic of the behavior described.

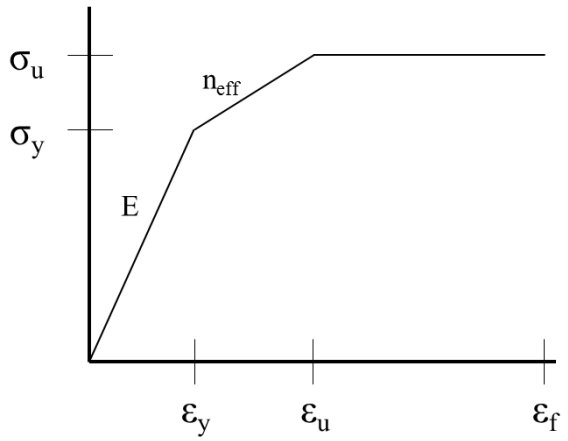

Figure 7.10: A schematic of the idealized hardening behavior used here to calculate n_{eff}.

The n_{eff} hardening parameter was calculated by finding the first strain value that had a stress within a certain tolerance of the ultimate strength seen during the test. This point was used to calculate ε_u, shown in Figure 7.10. The data was analyzed using two different tolerance values for the calculation of n_{eff}, both 2% and 5%. The n_{eff} values are shown for all samples in Figure 7.11.

As can be seen, the effective hardening parameter using a 2% tolerance is much more consistent across all samples. The high amounts of work hardening seen in the E2 and E3 samples is still observed, and the relatively low work hardening rates seen in the C2, C3, and D4 samples is also captured. This suggests that this n_{eff} hardening parameter is an effective measure of capturing work hardening. In addition to being simple and easier to calculate than K and n from the Ramberg-Osgood model, using n_{eff} as a measure of work hardening also has the advantage of being better suited as an output for a neural network or other simple computational predictive tool which required a numerical output.

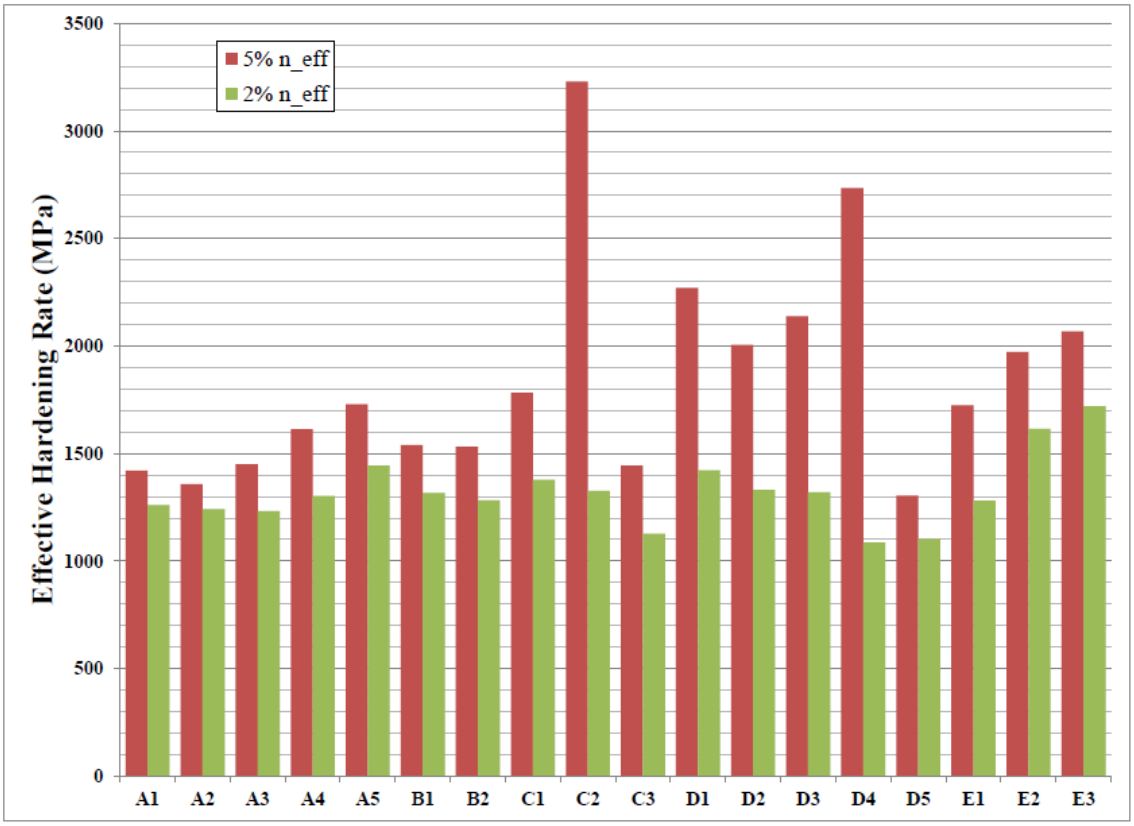

Figure 7.11: The effective hardening values calculated for all samples.

7.4.3 Ductility

It has already been observed that significant variation in the ductility was also achieved in the various samples. The observed range in the transverse direction, from 6.53% in A3 to 13.71% in C, was greater than the range observed in the longitudinal direction, from 10.00%in C2 to 13.80% in C1 and 13.89% in E1. The average ductility for each sample in both directions is shown in Figure 7.12.

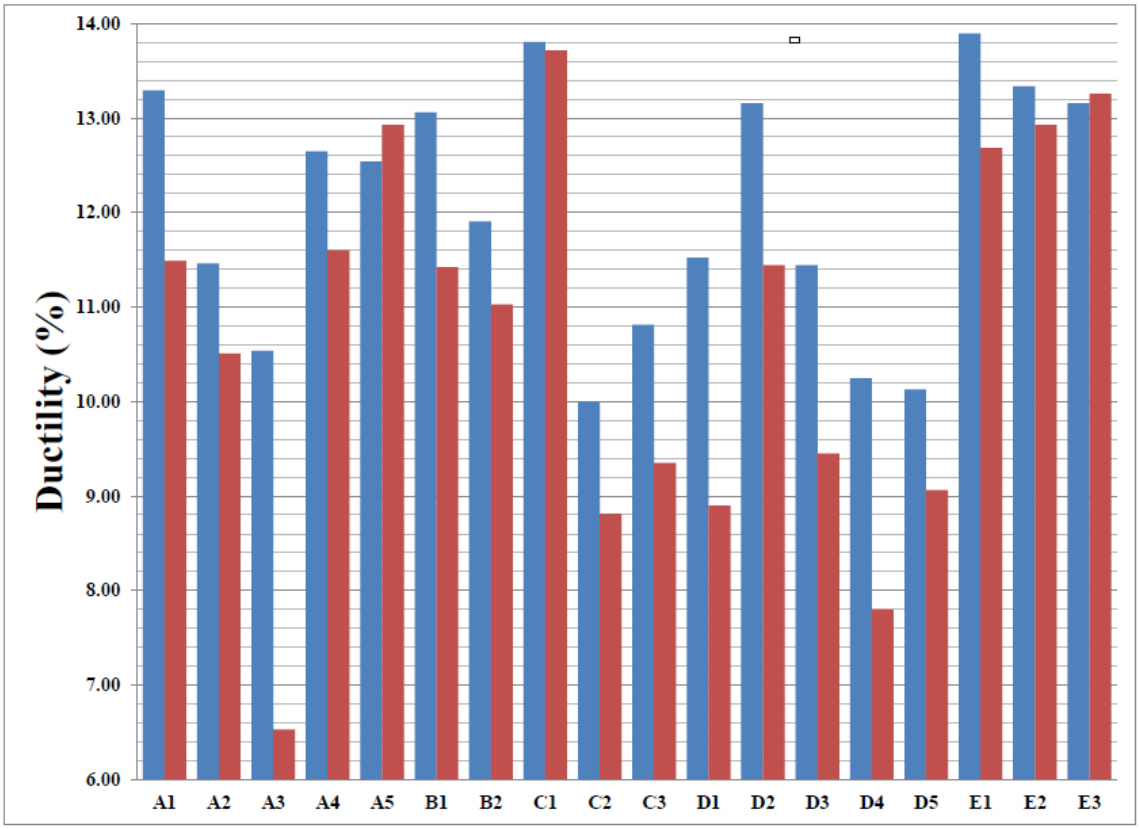

Figure 7.12: The ductility values that were measured in both the longitudinal and transverse directions for all specimens

7.5 Summary

The main goal of the experimental data generation in this project was to produce a sample set possessing a wide variation in microstructural features and all the mechanical properties of interest, and to examine the ease and feasibility of measuring these properties using commonly available mechanical testing methods. Here significant variation was achieved not only in the yield strength and ultimate strength of the different samples, but also in the work hardening behavior, the ductility, and the relative anisotropy of each property. Such variation across multiple different properties, observed independently from each other, in such a succinct data set means that this data set should contain the effects of various physical mechanisms which may be interacting to result in these various types of behavior. When couple with information

characterizing the microstructural features that determine these properties, as shown in the map developed in Chapter 4, this data should be well suited to examine the structure-property relationships that are defined in this space.

7.6 References

[1] ASTM International. B557: Standard test methods for tension testing wrought and cast aluminum- and magnesium-alloy products, August 2010.

CHAPTER 8

FRACTURE TOUGHNESS TESTING

Test coupons from the different plates were subjected to plane-strain fracture toughness testing according to ASTM standards in order to assess the toughness in both the minimum (S-L) and maximum (L-T) orientations. This chapter will discuss the details of machine and test-rig set up, the designing and machining of test specimens, the details of the test itself including the pre-cracking procedure, the post-processing, and analysis of the data. Once again, the aim of this work was to produce test specimens that possessed a wide variety of toughness properties, and to examine the ease and feasibility of measuring these properties using commonly available mechanical testing methods.

8.1 Specimen Preparation

Fracture toughness specimens were machined from the 1.5"x3.0"x3.0" 'R1' and 'R2' series test coupons, oriented as shown in Figure 8.1. The 'R1' test coupons represented the maximum fraction toughness direction (the L-T orientation), while the 'R2' test coupons represented the minimum fracture toughness direction of the material (the S-L orientation) [1].

The ASTM standard for K_{IC} toughness testing, E399, has strict requirements on the specimen dimensions that are used, which are generally shown for a compact tension (CT) specimen in Figure 8.2[1].

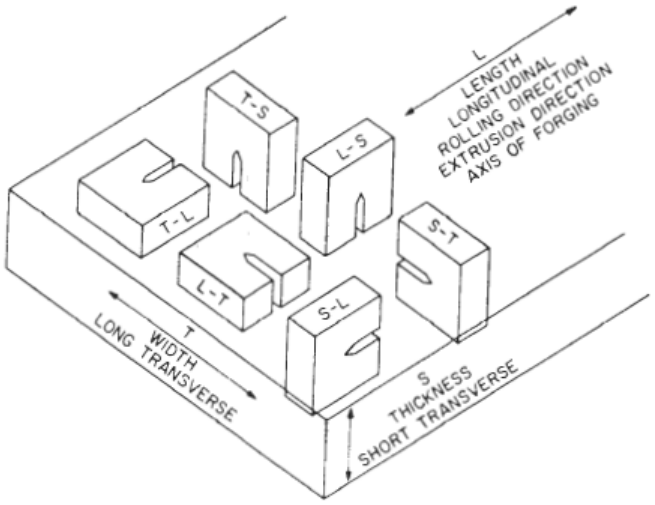

Figure 8.1: Crack plane orientation code for compact tension specimens in plate material, according to the ASTM E399 standard[1].

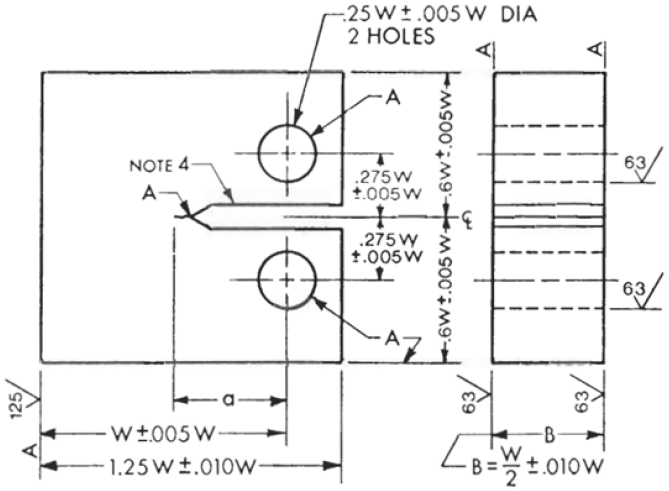

Figure 8.2: The general requirements for compact tension test specimens, according to ASTM E399 [1].

The minimum thickness generally allowed for plane-strain requirements to be met is

$$B, a > 2.5 \left(\frac{K_{IC}}{\sigma_{ys}} \right)^2 \tag{8.1}$$

Therefore, estimating a typical high K_{IC} value of 32MPa$\sqrt{\text{m}}$ and estimating a typical low yield strength value of 425MPa, then the specimen sizing requirements according to ASTM E399 are B and a greater than 14.17mm (.56”), W greater than 1.12”, and 1.25W or overall length L greater than 1.40”.

However, ASTM Standard B645 which dictates the requirements for linear elastic plane-strain fracture toughness testing of aluminum alloys, specifically states that the minimum ligament requirement (B,a) should be twice that stated in the E399 standard. Although no physical basis for this is given, it is noted that "experimental studies have shown that more uniform values of KQ are obtained for high toughness aluminum alloys when [these conditions] are met"[2]. Therefore, the specimen sizing requirements used here were B and a greater than 1.12", W greater than 2.24", and 1.25W or overall length L greater than 2.80".

Full specifications for the test specimens used in this work can be found in the drawings, located in the associated data repository. It can easily be seen from the drawings that machining these fracture toughness specimens is significantly more involved than for other specimens, such as those described in Chapter 7 for tensile testing. Here, the complicated geometry and tight tolerances in the machined notch region require either the use of expensive electrical discharge machining (EDM) techniques, or the purchase of a customized tool bit matching the exact geometry in question. Due to the large number of samples required for the scope of this project, the need for expensive machining techniques can quickly compromise project budgets. At one point a requested quote for EDM-ing of the 72 samples involved in this work returned a cost of approximately $17,000 for the machining alone. Therefore, for large specimen numbers such as those involved here, customized tooling on the order of ∼$1,000 is recommended.

8.2 Machine Set Up

Samples were tested on a Materials Testing Systems (MTS) servo-hydraulic test frame outfitted with a 22kip load cell. Samples were suspended by high-strength steel pins

loaded in specialty clevises, specified by ASTM Standard E399. Due to the large, non-standard thickness of the specimens tested in this work new clevises had to be machined from high-strength steel, adding to the time and expense of the project. To assist with the proper alignment of the test specimen, spherical washers capable of up to 3 degrees of rotation were located on the back of each clevis. A dummy specimen was loaded into the machine and the load was offset to 0lbf. Shims were inserted between the specimen and the clevis on both sides to hold the specimen correctly in place, and the spherical washers were tightened down to fix the apparatus at the necessary angle. Poor alignment of the specimen within the clevises can cause binding, uneven distribution of the load, and non-symmetrical fatigue crack growth during the pre-cracking stage, an example of which is shown in Figure 8.3. Therefore, ensuring proper alignment of the test frame is critical.

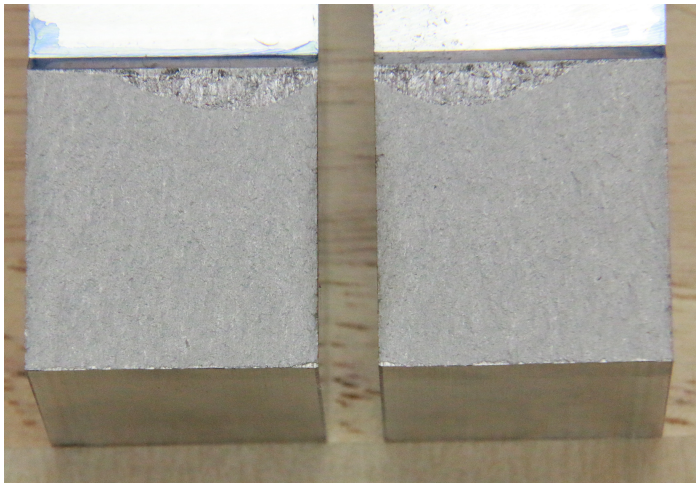

Figure 8.3: An example a non-symmetric crack caused by binding between the specimen and the clevis.

8.3 Pre-Cracking of Specimens

Machining alone cannot produce a suitably sharp crack tip for consistent and reliable fracture toughness testing[1]. Therefore, as a part of specimen preparation, it is necessary to grow a small crack at the end of the machined notch by fatigue loading. This pre-cracking procedure that precedes the actual fracture toughness test is a critically important step in the overall determination of a valid K_IC measurement. It necessary to control the fatigue cracking process so that the crack produced is unaffected by the procedure that produces it. This ensures that no additional variables are added to the materials design space defined in Chapter 4. To assist in this, the ASTM standard dictations that the fatigue pre-cracking procedure must meet the following requirements to constitute a valid test[1]

- The fatigue crack must be grown using 10^4-10^6 cycles
- The maximum stress-intensity factor K_{max} shall not exceed 80% of the K_Q value determined in the subsequent test if K_Q is to qualify as a valid K_{IC} result
- K_{max} shall not exceed 60% of the K_Q value during the final 2.5% of the overall crack length, called the terminal stage
- The ratio of K_{max} to the Youngs modulus of the material, should not exceed $.0003\sqrt{\text{m}}$ (or $.002\sqrt{\text{in}}$) during the terminal portion of the crack
- The R ratio used to grow the fatigue crack must by between -1 and +0.1
- The total fatigue crack length must be at least .025W
- The overall crack length, including both the machined notch and the fatigue crack, must be between .45W and .55W
- The loading frequency used during fatigue crack growth cannot exceed 100Hz

The large number of requirements not only increases the risk that a test may be invalidated, but also means that extensive dummy testing is required to determine appropriate loading conditions during the fatigue crack growth stage. This can be a particular challenge when a large range of K_Q values across specimens is not only possible, but the goal.

In this work, the fatigue crack growth was accomplished in two distinct stages. During the initial loading stage, the load was oscillated between 100 and 4100lbf at a frequency of 1Hz. A traveling optical microscope was used to observe starter-crack region. To assist with the observation of the fatigue crack the samples were painted with a dark blue quick dry machining paint in the region where the crack would be grown. To more easily track the progress of the fatigue crack length relative to the minimum length required, the predetermined minimum crack length was marked using a scribe across the inked surface.

The initial loading stage was completed after a fatigue crack was observed to have initiated at the site. The loading parameters during this stage were designed to initiate a load after approximately 1000 cycles. Once the fatigue crack has been clearly initiated, the final loading conditions were applied. During this stage, the maximum load during oscillation varied to ensure that the fatigue crack would not be grown in less than 10,000 total cycles, but still within a reasonable time frame. As a result the maximum load during final conditions ranged from 1900lbf to 2500lbf depending on the sample. Generally, the maximum loading condition was initially chosen to be 2100lbf, and if the fatigue crack showed little progress after 100,000 cycle had been reached, then the maximum load was increased to 2500lbf. In situations where a fatigue crack was initiated during the first set of loading conditions at much less than 1000 cycles, the maximum load chosen during final conditions was lowered to

1900lbf to ensure that 10,000 cycles were reached. Regardless, of the maximum load, the minimum load during oscillation was always chosen to be 100lbf and thereby maintain an R ratio of less than 0.1. In an effort to decrease the time required for pre-cracking, the frequency during the final stage was maintained at 10Hz, the practical limit given the machine and specimen size. However, observing the crack growth at this frequency was challenging and the procedure had to be periodically slowed down to 1Hz to observe the progress of the crack length.

There were many challenges in growing the fatigue crack under valid testing conditions, including the difficult having such a wide range of K_Q values. Without knowing the expected K_{IC} value of a particular sample, it is extremely difficult to apply appropriate loading conditions during this stage. Since it is impractical to determine individual pre-cracking loading conditions for each individual specimen being tested, it is necessary to pick a set of loading conditions that will obtain the necessary fatigue crack length in a moderate number of cycles, approximately 200,000-500,000. Then if a much lower K_Q sample is tested in the minimum orientation, the crack is not in danger of growing to completion in less than the minimum 10,000 cycles. And if a particularly high K_Q sample is tested in the maximum orientation, the fatigue crack can still be grown in less than the 1,000,000 cycle limit. In general, overly aggressive pre-cracking conditions are more detrimental to the subsequent data that is collected than overly conservative conditions.

However the significant drawback to such conservative conditions is once again in the scale of the samples necessary for testing. At a practical frequency limit of 10Hz a targeted 500,000 cycles means that a single pre-cracking procedure can take 14 hours to execute. Considering that the crack must be constantly observed, this should be considered an upper limit of acceptable testing time. Even if a test does fit in a more

manageable 6-8 hour work window through a combination of increased frequencies or decreased cycles, the high number of samples that require pre-cracking accelerates the problem. For example, the pre-cracking procedure detailed here was designed to grow the prescribed crack in approximately 100,000 cycles, which at 10Hz takes approximately 3 or more hours to execute. Considering the practical limitations of machine availability and work-schedules, the 72 specimens involved in this work would require, at the most optimistic limit, at least 6 weeks to pre-crack and prepare for testing. Therefore, it should be noted that the pre-cracking step required in this testing procedure can be considered the limiting step when considering both schedules and budgets.

8.4 Testing Procedures

Once specimens have been pre-cracked, the fracture toughness test itself can be carried out. Samples were tested in the same set up used for pre-cracking, described previously, but with the addition of a MTS Model 632.02E-20 clip gage. Specimens were pulled in tension until failure as the clip gage recorded the crack tip opening displacement (CTOD). The test was load-controlled with a loading rate of 10,000lbf/min, which is within the specified range given in ASTM E399. After failure, the fatigue crack length, which was observable in the fracture surface, was recorded at three different points, including the two ends of the specimen and the maximum length observed. Fatigue crack measurements for all samples are reported in full in the associated data repository.

8.5 Data Processing

Raw data collected directly from the test controller included the time, the load measured, and the crack tip opening displacement (CTOD) measured by the clip gage at each time step. Data for these tests were collected at 100Hz, which provided sufficient resolution for analysis and generated moderately sized data files with less than 10,000

data points. Since more than 2,000 data points were produced, and the MTS software rewrites the header every 2,048 data points it was necessary to remove these headers from the file before analyzing them. The code used to parse these files is included in the associated data repository with the rest of the Matlab scripts used for processing.

For each test, the maximum load obtained during the test, P_{max} is calculated and compared with P_Q, which is calculated as described in the standard. If $\frac{P_{max}}{P_Q}$ is valid, then K_Q is calculated using the measured crack values and the shape factor provided for CT specimens in Appendix A4 of ASTM E399. The crack values, which were measured experimentally, are reported in a separate excel spreadsheet. This spreadsheet calculates the average of the three reported values and reports whether or not they passed a series of checks. If there is less than a 10% difference between each of the three reported crack values and the averaged value, then the averaged value is the value used in the K_Q calculation. If this set of conditions is not met, then the crack value used to calculate K_Q is 90% of the maximum reported crack length. These crack lengths, the results of these checks, and the value used for K_Q calculation are all included in the associated data repository.

The script also reads in the corresponding yield strength value for the correct specimen and direction that were calculated and reported in Chapter 7. This yield strength value is used to check to see if the K_Q value that was measured can be considered a valid K_{IC} measurement. If the K_Q measurement is considered valid, then this value is written out as both the K_{IC} and the K_Q value. If not, then the K_{IC} value is not a number, and the K_Q value is still reported. Other values that were used that are written out to the processed file for completeness include the P_Q and P_{max} values, the strength ratio (which is useful if the $\frac{P_{max}}{P_Q}$ ratio is invalid), the crack value that was read from the crack values spreadsheet, and the calculated shape factor.

8.6 Results and Analysis

As discussed elsewhere, the main goal of the experimental data generation in this project was to produce a sample set with a wide variety of mechanical property values, and to examine the ease and feasibility of measuring these properties using commonly available mechanical testing methods. This section discusses the toughness values that were reported, including the values that were not considered to be valid K_{IC} measurements. Unlike the tensile test measurements discussed in Chapter 7, the fracture toughness tests that were conducted have many constraints on validity. These standards and constraints serve the very valuable purpose of ensuring that data is comparable regardless of the specimen geometry, the pre-cracking loading conditions used, and other test condition variations. If these conditions are not met, then the resulting measured value is a function of an uncontrolled input variable which is not accounted for in the PSPP map constructed in Chapter 4.

8.6.1 Plane-Strain Fracture Toughness

The average valid K_{IC} values that were measured are reported in Figure 8.4 for both the minimum (S-L) and the maximum (L-T) orientation. Valid K_{IC} values were obtained for all specimens in the minimum direction. These values varied from 20.20MPa$\sqrt{\text{m}}$ for the peak-strength D2 sample to 37.55MPa$\sqrt{\text{m}}$ and 38.24MPa$\sqrt{\text{m}}$ for the secondary precipitation-hardened E2 and E3 samples, respectively. This result is unsurprising, since it is generally expected that the T6 peak-aged temper will have the lowest available fracture toughness, especially amongst the traditional tempers. Similarly, the most impressive reported benefit of secondary precipitation-hardening in the interrupted treatment processes was the ability to significantly increase the toughness of the material over the T6 condition. Even though valid K_{IC} values in the maximum orientation were not obtained for all the samples tested, a significant range was still reported amongst those that did meet the validity conditions. The smallest

of these were 24.48MPa$\sqrt{\text{m}}$ for the retrogression and re-aged D4 and 24.57MPa$\sqrt{\text{m}}$ for the slightly over-aged C2. Although higher K_Q values were obtained, the highest valid K_{IC} measurement was reported for the peak-aged D2 sample, at 37.31MPa$\sqrt{\text{m}}$. Although the samples on the low end of this range are not surprising, it is slightly surprising that the peak-aged material which reports the lowest fracture toughness in the minimum orientation has such a high toughness in the maximum orientation. However, since 7050 is typically used in thick plate applications, the mechanical properties are typically only guaranteed in the minimum direction. Therefore, although the reported toughness value for this temper may be high in the maximum orientation, it comes with an extremely strong directional dependence, which can be seen in Figure 8.5.

These two figures clearly show that a significant variation in both the plane-strain fracture toughness and the directional dependence of this toughness was achieved. It is reasonable to suspect that those samples which showed a strong directional dependence in strength also exhibit a strong directional dependence in their toughness values, based on the discussion in Chapter 3. However, Figure 8.6, which plots the relative change in both yield strength and ultimate strength values with direction versus the relative change in the fracture toughness with direction, show that this is not always the case. In the majority of cases the directional dependence of the properties does correlate. However there are significant exceptions to this trend seen in samples D1, E1, and A5 shown in the top left and bottom right regions of the graph.

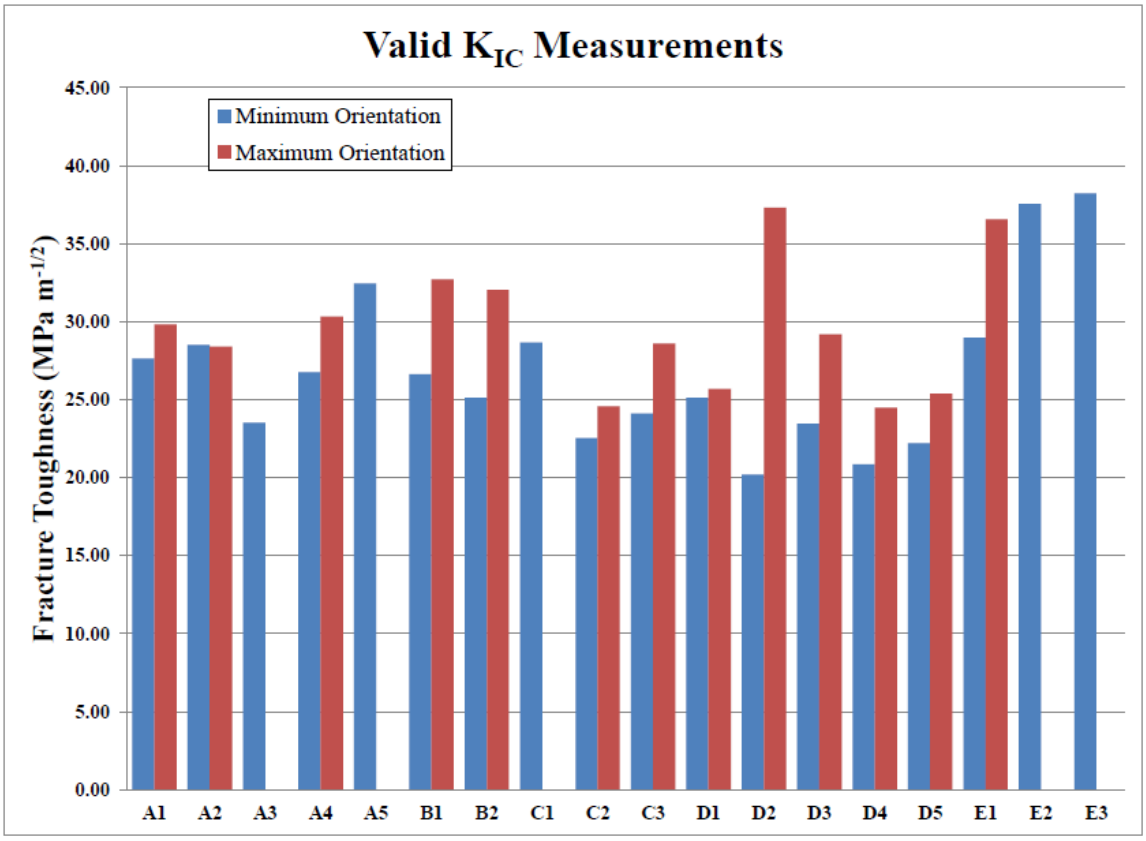

Figure 8.4: Threshold stress intensity factors for test specimens which were considered to have failed under plane strain, in both the maximum (L-T) and the minimum (S-L) orientations.

8.6.2 Validating Pre-Cracking Conditions

Many of the difficulties that were encountered in applying the pre-cracking fatigue conditions in this work have already been discussed. One of those difficulties included selecting appropriate loading conditions that would grow the crack at a fast enough rate without exceeding the maximum loading conditions, especially since the expected K_Q values were unknown. A summary table, included in the associated data repository, reports the maximum loads seen during pre-cracking and indicates which of the tested samples saw fatigue crack loading conditions that were higher than allowed, which may have caused some plastic deformation near the crack tip prior to the start of testing.

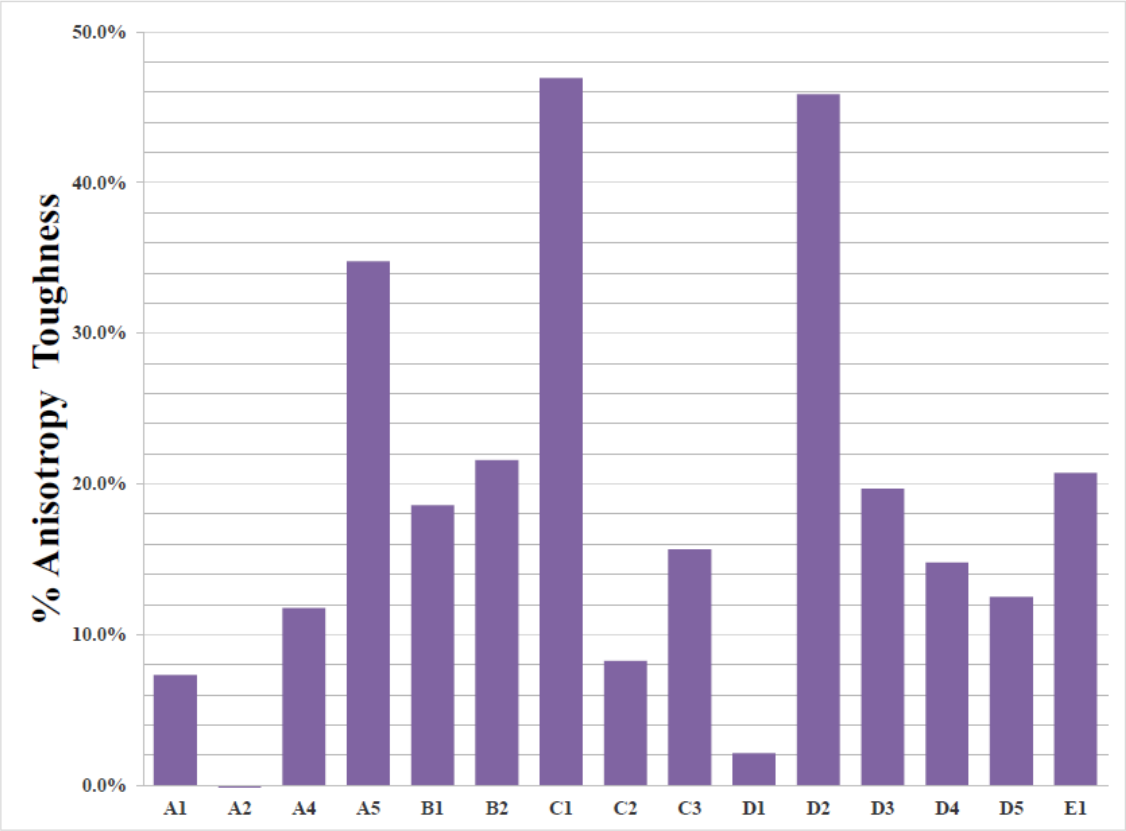

Figure 8.5: The directionality of the calculated threshold stress intensity factors when both orientations were considered to have failed under plane strain.

It is important to note that sample D4-R2-1 fast fractured during the initial loading conditions at only 700 cycles. Similarly C2-R2-2 was not checked often enough near the end of the test and the crack was allowed to grow until the sample failed at approximately 155,000 cycles. The E2-R1 and E3-R1 samples were fracture tested, but did not produce valid K_Q measurements due to an invalid $\frac{P_{max}}{P_Q}$ ratio. Therefore, despite the difficulty in applying appropriate pre-cracking loads to the various samples with unknown K_Q values, only a few samples would be considered invalid, and all of them occurred in samples oriented in the minimum toughness direction where K_Q values were significantly lower than expected when pre-cracking loads were initially calculated.

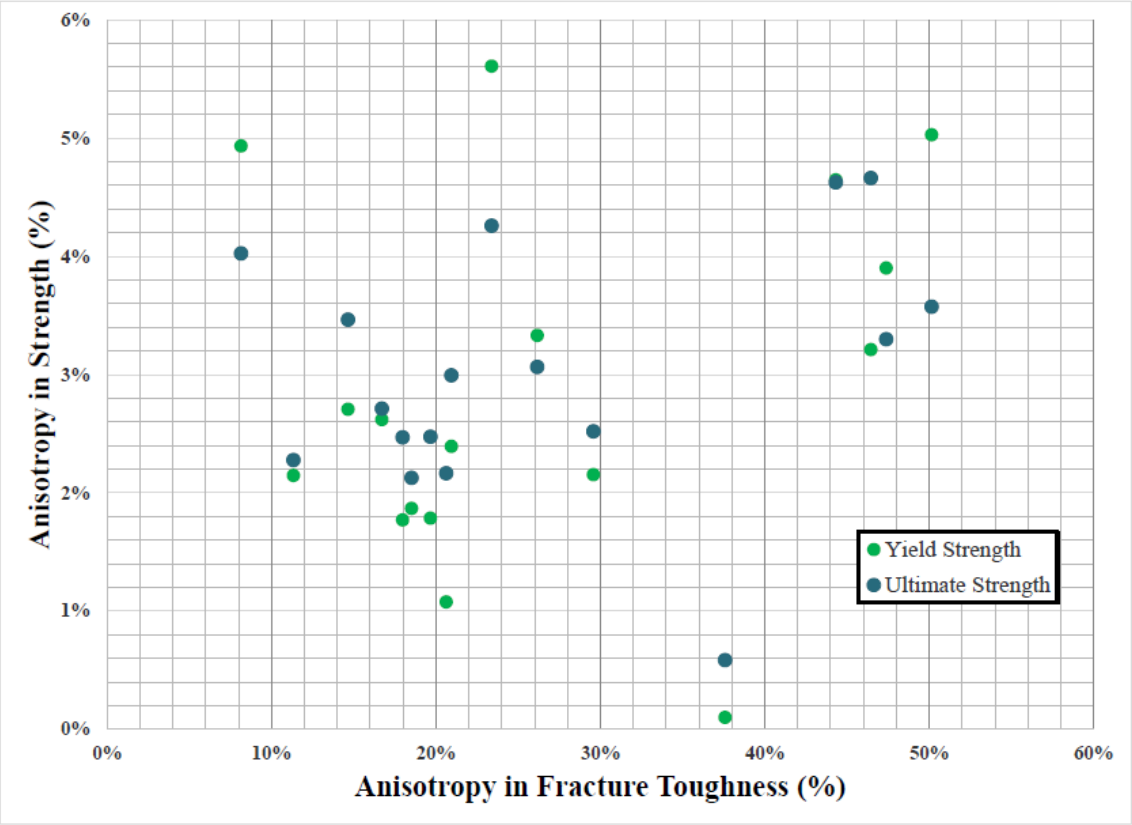

Figure 8.6: The relative change in fracture toughness with respect to the relative change in yield and ultimate strength for the various test specimens.

In addition to validity requirements concerning the maximum loading conditions, the ASTM standard also has requirements that must be met concerning the fatigue crack profile, measured experimentally after the fracture test has occurred. In particular, the standard calls for five different measurements of the fatigue crack length to be made: 1 at each end of the sample (a_1 and a_5), 1 at mid-thickness where the penny-shaped crack should have reached a maximum (a_3), and 2 at the quarter thickness points(a_2 and a_4). The three measurement made in the body of the sample (a_2, a_3, and a_4) should be averaged to get the reported crack length for K_Q calculation. However, this value is only considered to be valid if[1]

- The difference between any two of a_2, a_3, and a_4 does not exceed 10% of the

average a

- No part of the fatigue crack front is closer than .025W to the machined starter notch
- Neither a_1 or a_5 differs from the average a by more than 15%
- The difference between a_1 and a_5 is not more than 10% of the average a

However, these requested measurements and conditions largely assume that a symmetric penny-shaped crack results from the fatigue pre-cracking procedure. While many of the samples oriented in the minimum fracture toughness direction did experience this kind of crack growth, many other samples, especially those oriented in the maximum fracture toughness direction did not. Examples of representative penny-crack profiles are shown in Figure 8.7.

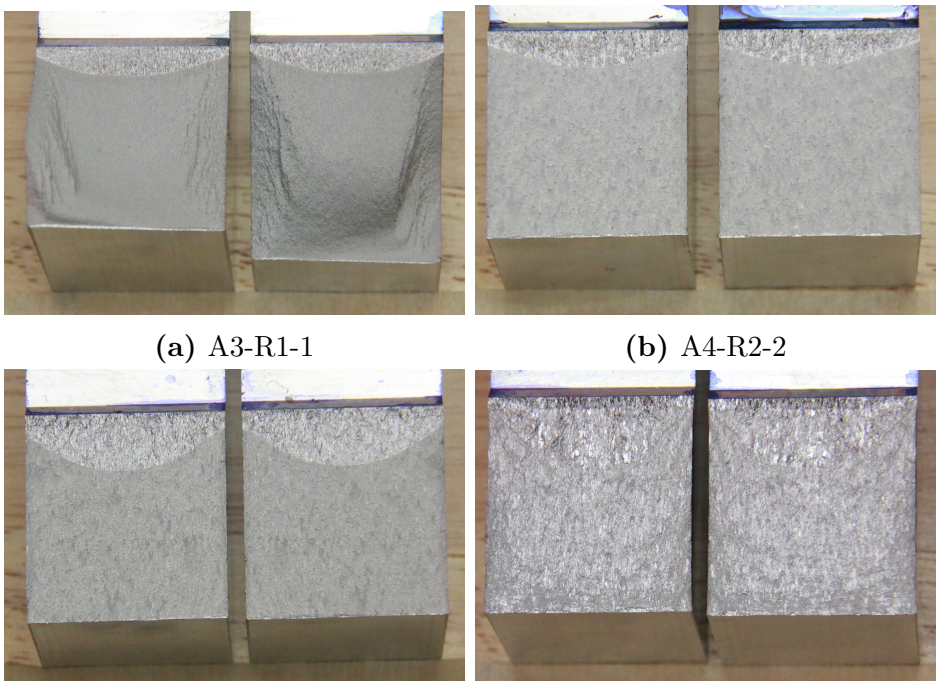

(a) A3-R1-1 **(b)** A4-R2-2

(c) D5-R2-1 **(d)** E3-R2-1

Figure 8.7: Representative examples of penny-shaped fatigue crack profiles.

In this work, only three measurements of the fatigue crack length were taken and

averaged, including two measurements at the specimen surfaces and a measurement at the maximum crack length observed, regardless of its location with respect to the specimen thickness. As long as none of these three measurements differed from the averaged value by more than 10%, the averaged value was used to calculate K_Q. If one measurement did differ from the average by more than 10%, usually as a result of either a severe penny-shaped profile or a highly non-uniform crack profile then a crack value of 90% of the maximum reported value was used to calculate K_Q. As seen in Figure 8.7, the criterion applied in this work was just as successful as the ASTM criterion at catching extreme penny crack formations and recognizing which samples needed to use a higher crack length than the calculated average to determine K_Q.

However, only about half of the tested samples showed penny-shaped fatigue crack profiles. In most samples that were oriented in the maximum fracture toughness direction, highly non-uniform crack profiles were observed. Some representative profiles are shown in Figure 8.8.

In the measurement of these non-uniform crack lengths, the ASTM criterion was, for the most part, not observed to be more successful at determining non-uniform crack profiles. Therefore, the criterion used here was determined to be just as suitable as the ASTM methods of measurement, and involves almost half as many measurements to be taken.

8.6.3 Validating K_{IC}

As discussed in earlier in this section, only four of the samples that were oriented in the maximum fracture toughness direction (L-T) did not give valid K_{IC} measurements. Of those four, A5 and C1 both produced valid K_Q values but did not meet the plane-strain condition based on their K_Q and yield strength values. Therefore,

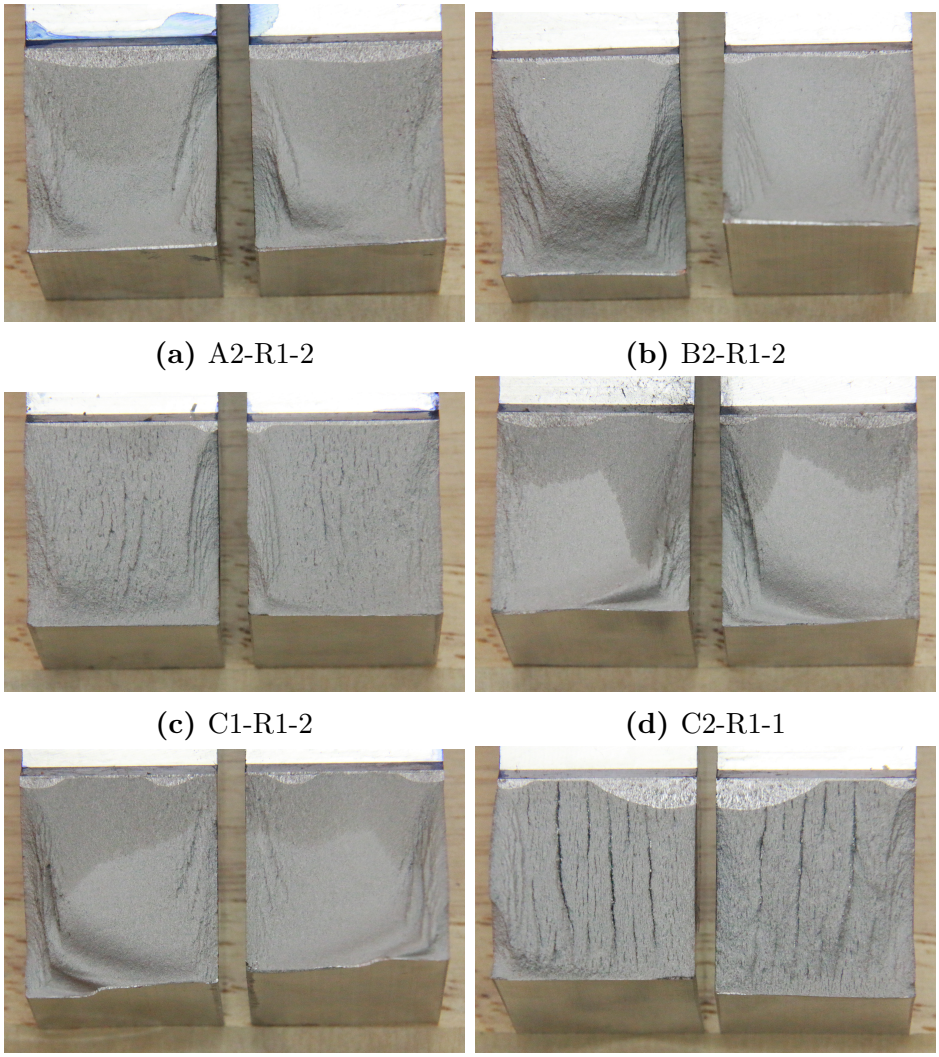

(a) A2-R1-2 **(b)** B2-R1-2

(c) C1-R1-2 **(d)** C2-R1-1

(e) D5-R1-1 **(f)** E3-R1-2

Figure 8.8: Some representative examples of penny-shaped fatigue crack profiles.

these K_Q values, shown in green in Figure 8.9, will be artificially high compared to the other K_{IC} values reported, since these measurements were collected under a plane stress condition.

The other two samples that didnt produce valid K_IC measurements were E2 and E3, which had P_max/P_Q ratios that exceeded 1.10 and therefore didnt even generate meaningful K_Q values. However, their K_Q value, had it been calculated, would

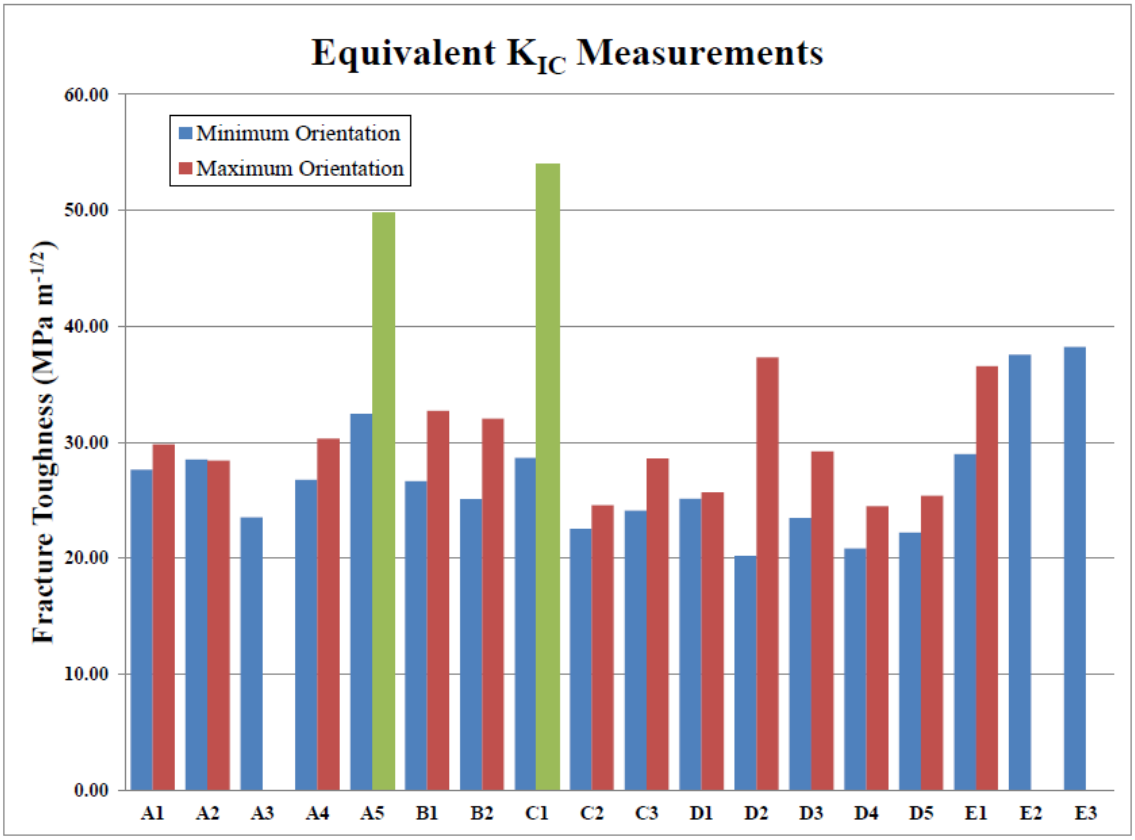

Figure 8.9: Threshold stress intensity factors in both the maximum (L-T) and the minimum (S-L) orientation for all test specimens, regardless of if they are considered to have met the plane strain condition.

have been even higher than those reported for A5 and C1, at 67.44MPa$\sqrt{\text{m}}$ and 71.41MPa$\sqrt{\text{m}}$, respectively. While it may be obvious that the plane-strain condition is not met in these samples, it is clear from observing the fracture surfaces, shown in Figure 8.10, that something even more complicated may be causing these abnormally high results.

These fracture surface show that the method of failure in these specimens was by the growth of penny-shaped cracks in the plane of minimum fracture toughness orientation. Once these penny-shaped cracks grew across the ligament, the specimen failed. These results are reminiscent of those seen by Kaufman in 1967, in multi-layered adhesive-bonded panels. Kaufman showed that when sheets of aluminum

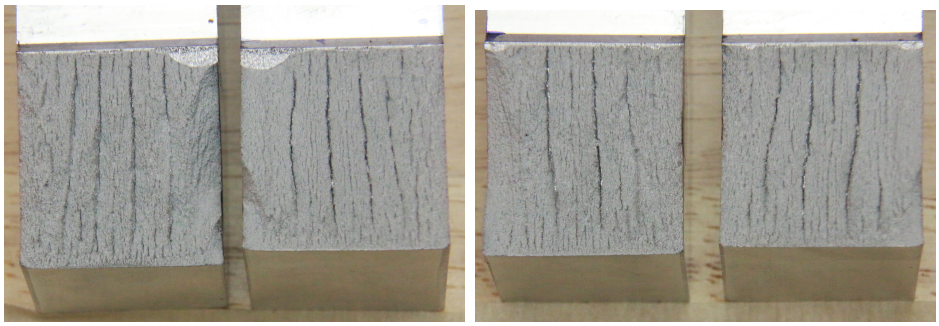

(a) E2-R1-1 **(b)** E2-R1-2

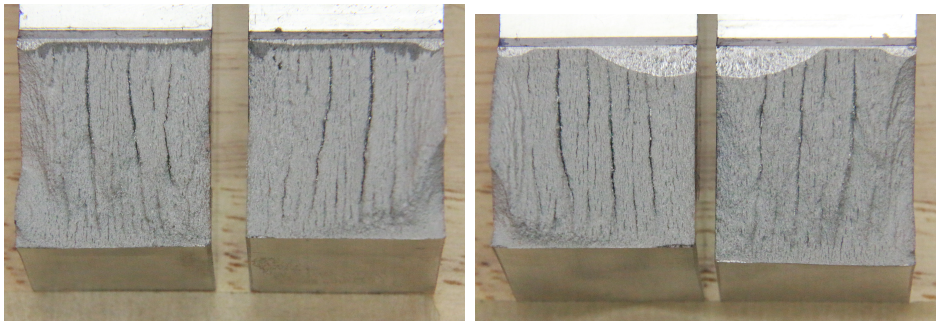

(c) E3-R1-1 **(d)** E3-R1-2

Figure 8.10: Fracture surfaces from the E2 and E3 samples oriented in the maximum fracture toughness direction. The penny-shaped cracks protruding in to the specimen are oriented in the direction for minimum toughness.

were bonded together and tested for toughness in a similar orientation, the fracture toughness of the laminated specimen was equal to the fracture toughness of one the sheets tested individually. Since these thin sheets are subject to plane-stress loading, which produces a significantly higher toughness, the observed toughness of the laminated structure is also significantly higher and is dictated by the thickness of the laminated sheets[3]. This phenomenon matches the fracture surface observed in Figure 8.10, and suggests that the E2 and E3 samples are behaving as laminated structures.

However, since these values are also clearly inflated due to their lack of plane-strain condition, it is impossible to draw more than qualitative comparison conclusions for these samples, as well as the A5 and C1 samples. This does mean, however, that the

valid K_{IC} measurements can be compared in a quantitative sense, and can be used to examine the PSPP relationships within the materials design space defined in Chapter 4. But only if the plane-strain condition which is being assumed is actually met in the material, otherwise these measurements must be considered a function of the loading condition as well as the various microstructural features outline in previous chapters. Plane-strain conditions can be confirmed visually by examining the fracture surface and noting the relative size of the shear lips compared to the flat brittle fracture area that should be seen in the center of the specimen. When the shear lips occupy a large portion of the fracture surface, it is typically a sign that plane-strain conditions were not met in the material. In this work, all specimens that were oriented in the minimum fracture toughness direction very clearly met the plane-strain condition, since there are no observable shear lips on any fracture surface. However, in the specimens oriented in the maximum fracture toughness direction, a wide variety of fracture surfaces were observed. Some representative fracture surfaces from those samples that generated valid K_{IC} measurements can be seen in Figure 8.11.

As can been seen, some fracture surfaces such as C2 and D4 have shear lips that are relatively quite small compared to the rest of the fracture surface. Others, such as A4 and B2, and to a lesser extent A2, have very large shear lips, even larger than those seen in the A5 sample found in Figure 8.12. The E1 fracture surface has very small shear lips as well, however is does seem to suggest a laminate-like effect as observed in E2 and E3. C1, which did not produce a valid K_{IC} measurement despite having small shear lips, also hints at this effect.

This suggests that the ASTM validity check for the plane-strain may be a poor measure of whether or not plane-strain is actually observed in the material. Additionally, replacing this condition with one based on the area fraction of the shear-lips

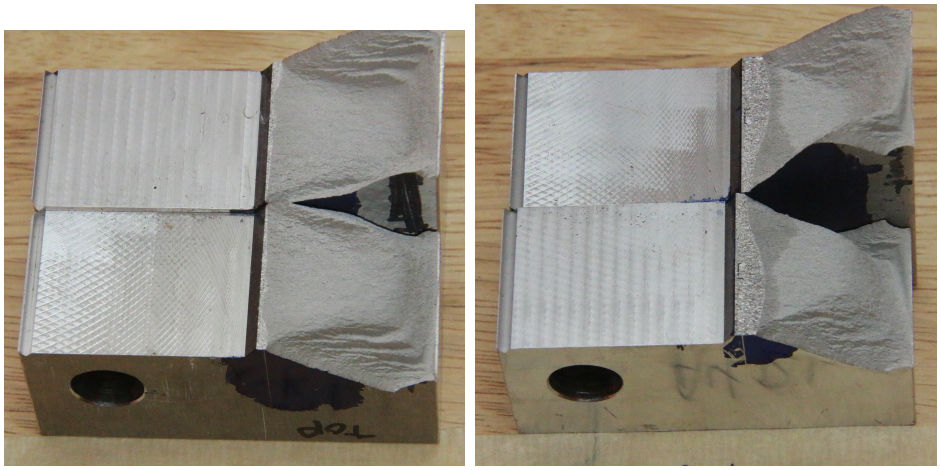

(a) A2-R1-1

(b) A4-R1-2

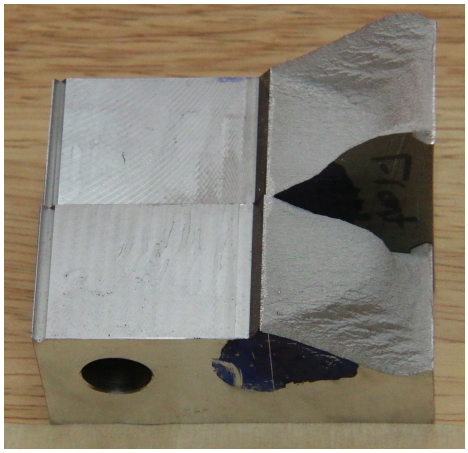

(c) B2-R1-2

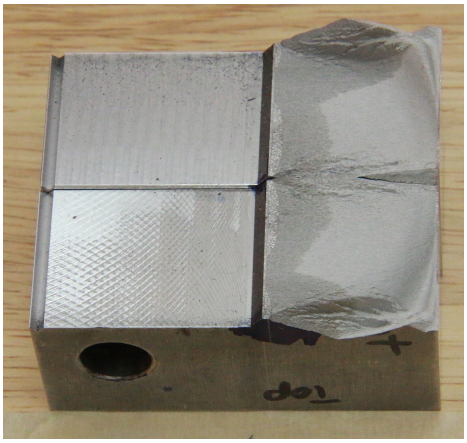

(d) C2-R1-1

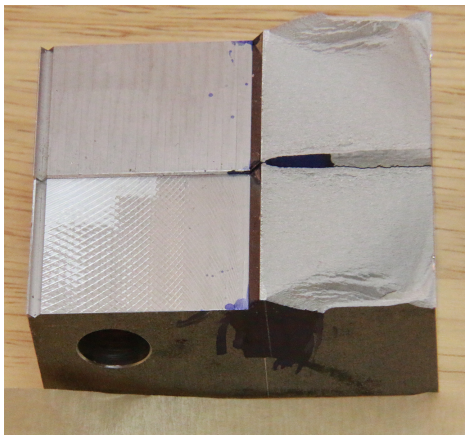

(e) D4-R1-2

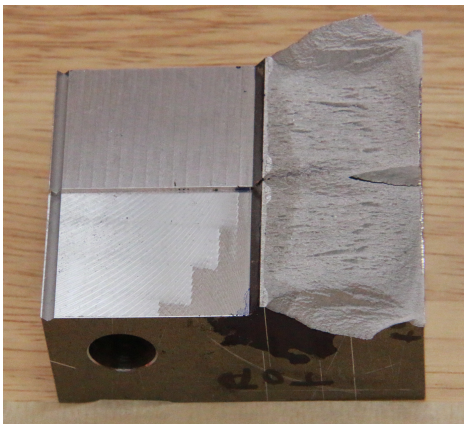

(f) E1-R1-2

Figure 8.11: Representative fracture surfaces from samples oriented in the maximum toughness direction which produced valid K_{IC} values according to the ASTM standard.

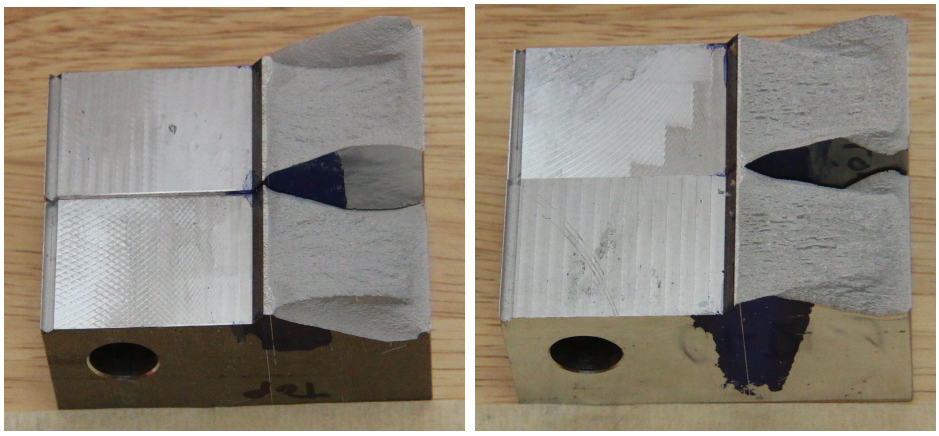

(a) A5-R1-1 **(b)** C1-R1-2

Figure 8.12: Fracture surfaces from the A5 and C1 samples which did not produce valid K_{IC} values.

may not perform significantly better, unless observation of a possible laminate-like effect can be ruled out. Together, these observations suggest that although fracture toughness is an extremely important parameter that needs to be measured in a quantitatively comparable way, the standard fracture toughness measurement which is complicated, difficult to execute for a wide variety of samples, time-consuming, and material-expensive may not be achieving this goal. However, more work needs to be done to ensure that this phenomenon is not a result of the through-thickness various that can accompany thick-plate material.

8.7 Summary

Ultimately, the fracture toughness of the material is an important design parameter, and therefore it is critical that consistent, high-fidelity data be obtained that is quantitatively comparable and independent of geometry, loading condition, and other variable testing parameters. However, the ASTM E399 standard plane-strain fracture toughness test, which is meant to ensure this kind of quantitatively comparable data, may not be suitable when applied consistently to a large set of samples

that are expected, and indeed designed, to exhibit a large variation in toughness values. This is largely due to the various sizing, geometry, and loading requirements involved in this standard, which must all be estimated based on the expected K_Q value. Therefore, while this is still an excellent testing standard especially in the certification and qualification of particular materials and tempers, it is not suggested as the preferred method of toughness testing for MGI and ICME projects such as the one demonstrated here. Instead, either faster and less time-intensive measurements which are not a function of additional input variables like specimen geometry or loading condition, should be used (such as ASTM E1820). Or alternatively, the added input variable must be somehow incorporated in to the PSPP map as it is defined in Chapter 4 in order to communicate the necessity of measuring and including this variable within the space.

8.8 References

[1] ASTM International. E399-90: Standard test method for plane-strain fracture toughness of metallic materials, November 1990.

[2] ASTM International. B645: Standard practice for linear-elastic plane-strain fracture toughness testing of aluminum alloys, May 2010.

[3] J. G. Kaufman. Fracture toughness of -t6 and -t651 sheet plate and multilayered adhesive-bonded panels. *Journal of Basic Engineering*, 89:503–507, 1967.

CHAPTER 9

CORROSION TESTING

The goal of this work was to produce samples that had a variety of mechanical properties, including different resistances to failure by stress corrosion cracking (SCC), and to examine the ease and feasibility of measuring these properties using commonly available mechanical testing methods. As discussed in Chapter 3, this SCC resistance can be estimated in many different ways, often through the use of other familiar mechanical property tests (such as those described in Chapter 7 and 8) under a corrosion environment. Similar to the fracture toughness tests discussed in Chapter 8, most corrosion test measurements, are also difficult to separate from their specimen geometry or test conditions. Since these tests must be performed under a corrosive environment, the selection of that environment adds another potential variable that must be controlled (or measured and accounted for). These necessity of controlling these additional input variables, along with the long time scales required for more traditional corrosion tests, may help to explain the recent popularization of potentiodynamic polarization as a high-throughput testing method for corrosion resistance in high-strength aluminum and other alloys. This work conducted potentiodynamic polarization and open circuit potential measurements to examine if any of the various parameters that could be collected might be potential candidates to correlate with corrosion behavior. For a parameter to be a promising indicator of corrosion behavior it must show wide variation across the sample set tested here and be a reliable, consistent, and quantitative measurement with minimal subjectivity and bias involved in its collection and analysis.

9.1 Specimen Preparation

Corrosion samples were taken from the 1"x1"x1" 'D' blocks, as detailed in Chapter 5, and were further reduced to 0.5"x0.5"x0.5" cubes. An abrasive cut-off saw was used to minimize the damaged layer while maximizing the efficiency of cutting. After cutting, samples were backed with double-sided carbon tape and a threaded bolt used for attachment in the test set-up was inserted. The configuration was then cold mounted in an epoxy and dried under vacuum to prevent the formation of bubbles and the interference of moisture. Cold-mounting was preferred in this application over hot-mounting, since hot-mounting usually requires temperatures of at least 120 °C. Even though the time at this temperature is short, usually only about 15 minutes, exposure at these temperatures can artificially age the material slightly. Cold-mounting does not expose the sample to elevated temperatures, and even though setting times can be long (up to 24 hours) it is relatively easier to prepare many samples at once. Therefore, cold-mounting was used to advantage in this application. One 0.5" cube sample from each of the two different 'D' blocks were mounted for testing, in order to capture a small amount of microstructural variation. This would ensure that any anisotropy in the grain structure was accounted for. In this work, only the LT plane was measured, but ideally three samples could be run from three different specimens oriented according to the trisector method discussed in Chapter 6. After samples were fully mounted, they were hand-polished with 120, 600, and then 2000 grit paper to obtain a smooth surface prior to testing. To ensure a consistent exposure area for testing, the polished surface was covered in tape punched with 1 cm^2 circle.

9.2 Test Set Up and Procedures

Samples were tested in a typical three electrode electrochemical cell. Here the specimen being tested served as the working electrode, a platinum rod served as the counter electrode used to supply the current flowing at the working electrode during

the test, and a standard Saturated Calomel Electrode (SCE) served as the reference electrode.

Gamry Echem Analyst Software was used to conduct both tests. The open circuit potential test, which measures changes in potential over time was used to determine the open circuit potential (OCP), also known as the corrosion potential E_{corr}. In these tests the potential, which was allowed to fluctuate as the system attempted to reach steady state, was measured every second for the duration of the one hour test.

Potentiodynamic polarization tests changed the potential in small increments over a set range. After each increment the current was measured. In this work, tests were automatically designed to start the cyclic polarization scan 100mV below the E_{corr} potential that was measured in the OCP test. Therefore, if poor OCP data is collected in the first test, this could significantly impact the range of voltages scanned for the dynamic test. From this initial potential, the forward scan rate was 0.5mV/s through both the cathodic and anodic reactions and continued until the current density reached 100mA/cm^2 before being reversed at 0.5mV/s back to the E_{corr} value collected from the OCP test.

Tests are typically conducted in a 0.1M (3.5%) sodium chloride solution. While other molarities can be used, 0.1M solution is typically the most common and has been shown to induce stress corrosion cracking in 7050 aluminum. Since a wide variety of corrosion behavior is expected from the samples being tested, two different molarities were tested to see which gave the best resolution for a small section of samples. Five samples, A5, C1, C3, D1, and D2 were tested in both 0.001M and 0.1M solutions are plotted in Figures 9.1 and 9.2, below.

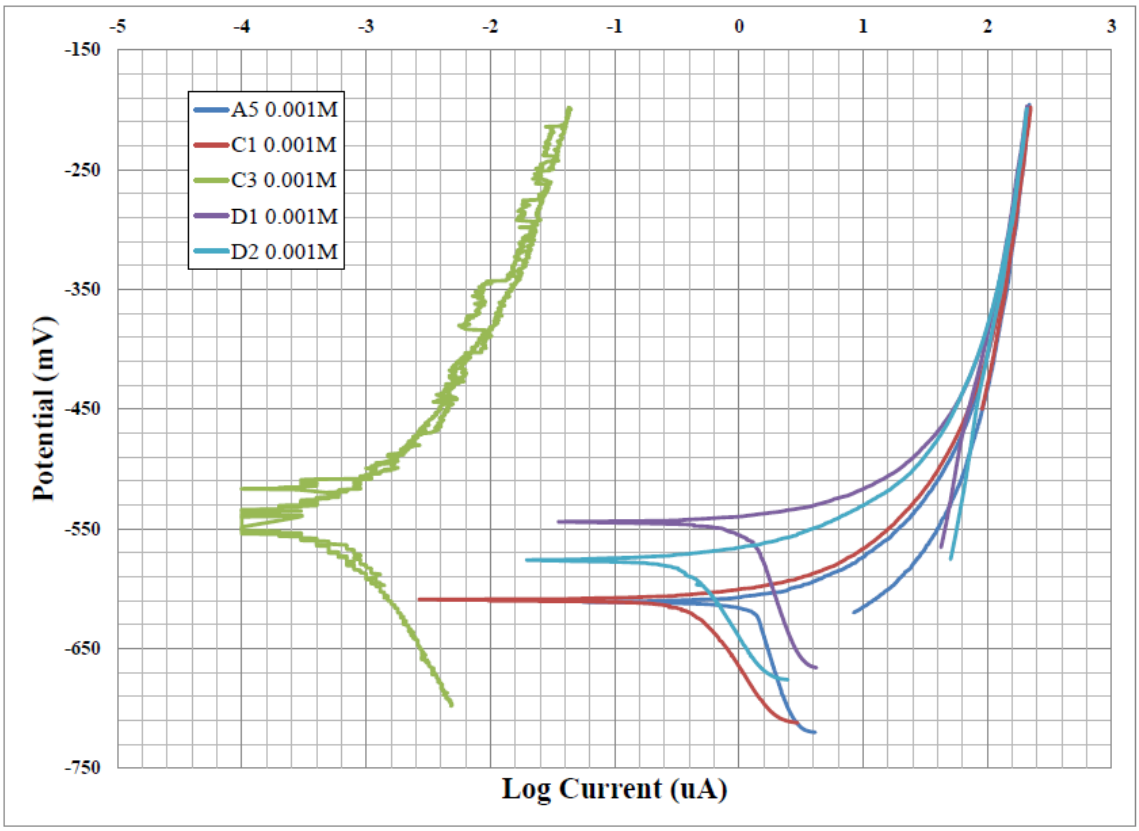

Figure 9.1: Five specimens tested in a 0.001M NaCl environment.

As seen in these plots, both molarities showed a similar range in the E_{corr} values, but 0.1M showed a greater range in the I_{corr} values that were measured for the different samples. Therefore, 0.1M solution was used in this work.

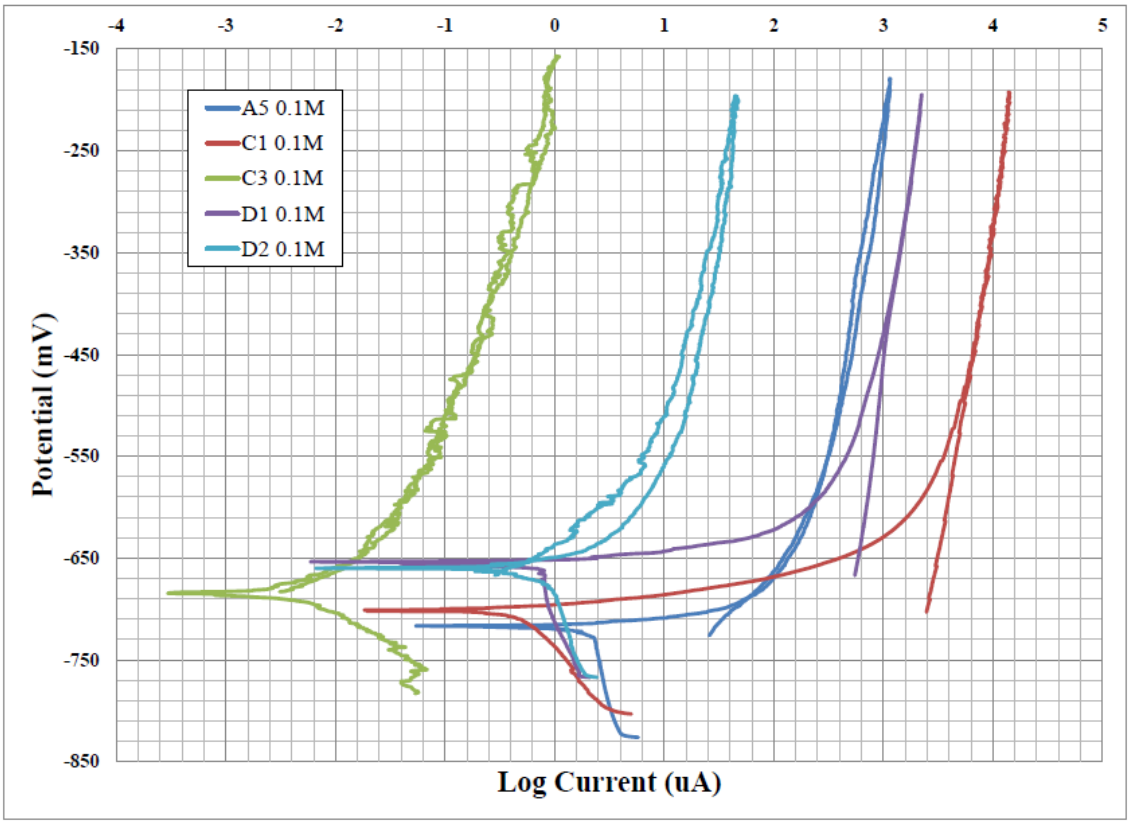

Figure 9.2: Five specimens tested in a 0.1M NaCl environment.

9.3 Results and Analysis

9.3.1 Open Circuit Potential

The open circuit potential test, which measures changes in potential over time is used to determine the open circuit potential, also known as the corrosion potential E_{corr}, and is characteristic of the metal-solution interface. Therefore, E_{corr} should theoretically change with changes in the metal. While changes in the OCP of a freshly fractured surface have been shown to correlate well with changes in the plateau crack velocity other work has shown that changes in the OCP of a polished surface may not sensitive enough to small changes in microstructure to be reliably resolved in this type of test [1, 2, 3].

Ideally, the potential should approach a steady-state value with time. However, examining plots of the potential with time for the various samples shows that a wide variety of different types of behavior occur in the tests conducted here. Figure 9.3 shows some representative OCP curves that were observed.

Some samples, such as D1-1 and even A2-1, showed stable OCP values after relatively short times. Others, such as B1-2 fluctuated through what appears to be some sort of reaction that occurred at the surface before finally reaching a steady state. Others seem to have gone through some type of possible reaction, but had potentials which continued to increase steadily to the end of the test. It is possible that if the test were continued these samples would have eventually reached at steady state, but this behavior cant be confirmed. Approximately eight samples, including A3-2, showed an extreme variation in the potential with time. But since this random oscillation occurred across a stable mid-point it is unclear if this was due to "noise in the data or some other physical phenomenon. A few samples, such as C1-1, showed steady increases or decreases in the potential with time and don't appear to approach a steady state potential at all during the test. Still others, such as D2-1, appeared to reach a steady state quite early in the test, only to experience a sharp change to a new steady state potential halfway through testing. Ultimately, some of these behavior meant that deriving a steady state OCP value from the data collected was often difficult even when analyzed individually. When automated processing with Matlab was attempted, determining a reliable OCP value was made even more difficult by the wide variation in behaviors that were seen. Values that were calculated are reported in Figure 9.4, below.

Ultimately, this variation in behavior could be caused either by an environmental effect, such as oxidation due to the presence of oxygen in the corrosive solution, or by

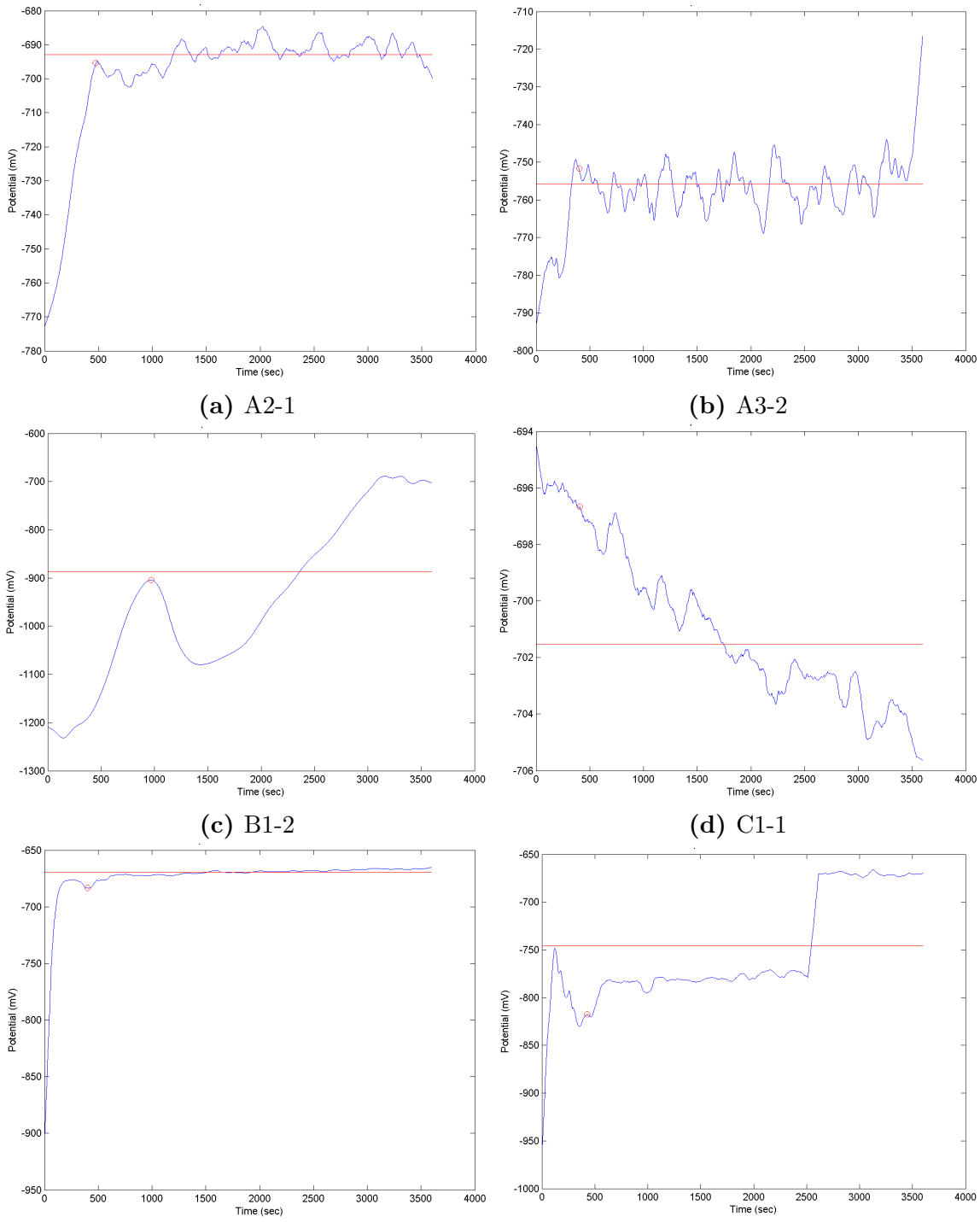

(a) A2-1 **(b)** A3-2

(c) B1-2 **(d)** C1-1

(e) D1-1 **(f)** D2-1

Figure 9.3: Representative potential-time plots from the open circuit potential tests conducted on various samples, showing the different types of behavior that were observed.

various localizations in the microstructure. In an attempt to rule out the presence of oxygen within the environment playing a role, some deaerated tests were conducted, but the behavior continued to fluctuate. Therefore, since this type of test does measure the local corrosion behavior of the material, it is likely that such variation in the behavior of the system is the result of the highly inhomogeneous microstructure.

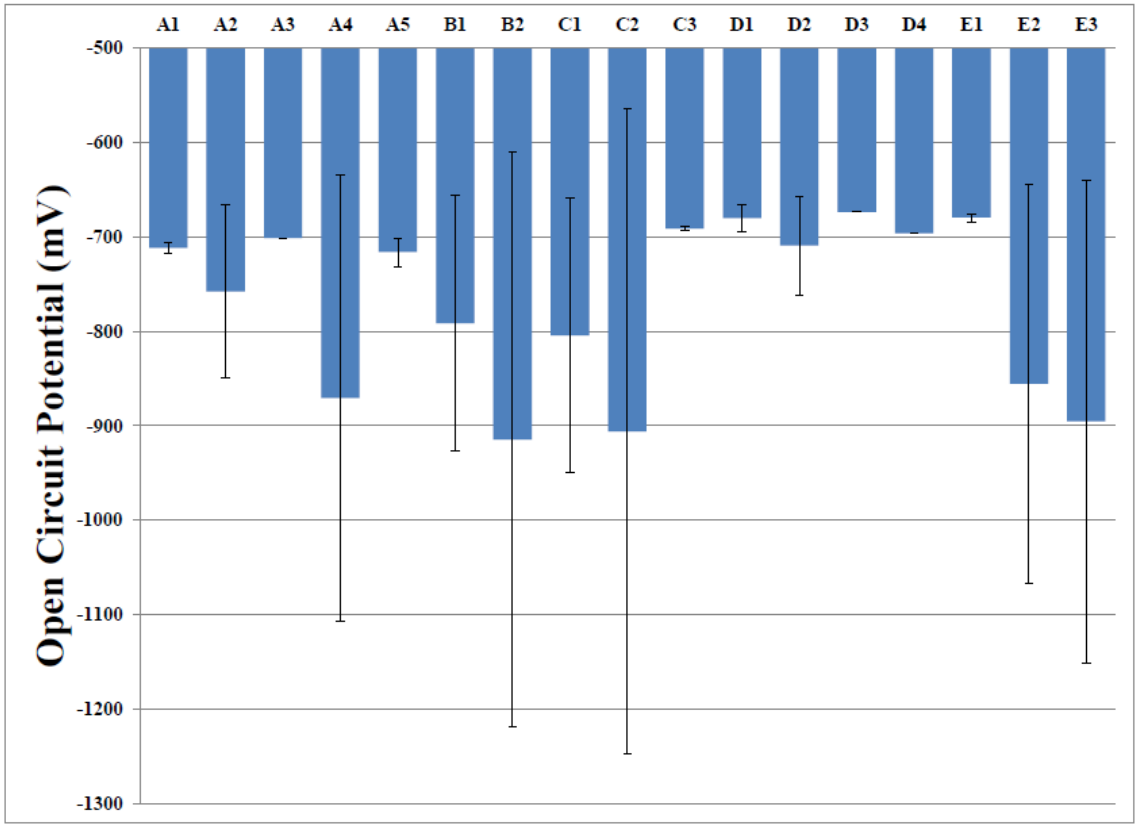

Figure 9.4: The open circuit potential values that were measured, plotted with their corresponding small sample error.

One of the main uses of the open circuit potential test is to inform the scan range for the potentiodynamic polarization test. In order to be sure that the potential range will include both the cathodic and anodic Tafel plots, it is important to start the test at a potential below that of E_{corr}. Tests conducted in this work aimed to start at a potential of 100mV below the expected E_{corr} value, though 250mV below the

corrosion potential is more common in Tafel plots [4, 5]. If the initial potential of the test is not sufficiently below the corrosion potential then it is possible that an inaccurate cathodic Tafel slope will be calculated, resulting in an incorrect measure of the corrosion current I_{corr}.

However, based on the open circuit potential measurements that were collected, as well as the initial polarization curves obtained during the molarity tests, it seems that for a given environment the corrosion potential does not vary much across all of the samples in the set. Therefore, one future approach would be to run a small sample of initial tests to determine the OCP of the samples within the environment and then begin the test at a potential sufficiently lower (by at least 250mV) than the average OCP observed. Not only does this provide a more accurate measure of the corrosion potential, which is critical if good data is to be obtained during the polarization scan, but it is also much more efficient when such a large number of samples are involved.

9.3.2 Polarization Scans

Potentiodynamic polarization scans of the kind conducted here should encompass both the cathodic and then anodic Tafel plot region before an increase in the current and potential are observed. If the current increases sharply with respect to the potential change then pitting has occurred. If pitting does occur, the curve will typically form a loop before crossing itself, indicating that the material has re-passivated. The potential where the loop closes is considered the passivation potential. If pitting does not occur then once the current density predetermined in the test parameters has been reached, the potential will be reversed and the curve will follow back on itself. A typical potentiodynamic polarization scan showing pitting and re-passivation is shown in Figure 9.5[4].

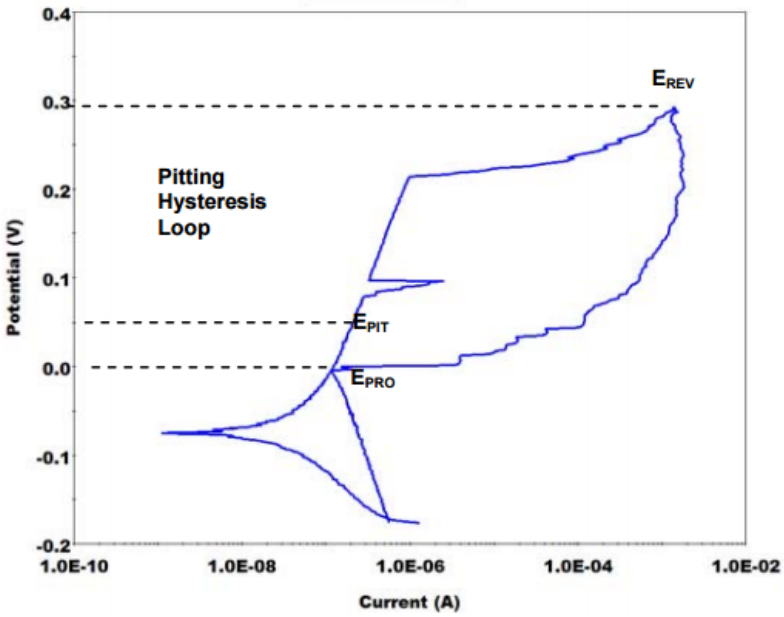

Figure 9.5: A typical potentiodynamic polarization curve in which pitting is observed.

From this scan, the parameters that are typically of interest includes the pitting potential, E_{pit}, which is easily identifiable if pitting occurs and in which case E_{pot} is also of interest. Whether or not pitting occurs, E_{corr} and I_{corr} can be calculated from the Tafel slopes of the two reactions. E_{corr}, which is identifiable by the sharp asymptotic-like intersection point of the two reactions, can be measured easily and more reliably in these scans than in the steady state open circuit potential tests previous mentioned. I_{corr}, however, cannot be measured directly and is usually calculated by fitting a straight line to the linear region of each reaction. The slope of these lines, known as the Tafel constants or Tafel slopes, can be used to extrapolate the lines through E_{corr}. The intersection of the line with E_{corr} represents I_{corr}. However this method of calculating I_{corr} is based on a very simplistic model of the reaction, and does not always give an accurate measure of the corrosion current. In scans such as those conducted here, where both the cathodic and the anodic reactions are measured, the two tafel slopes should intersect each other at E_{corr} and therefore give a consistent measure of I_{corr}. As observed in many of the scans included both in

this chapter and in the associated data repository, this intersection point does not occur at E_{corr}. This is usually an indication that at least one of the reactions is not kinetically controlled and therefore does not exhibit a linear Tafel region. In these situations the most linear of the two Tafel regions should be used to extrapolate the slope through E_{corr} to determine the corrosion current [4, 5]. The calculated values for E_{corr} and I_{corr} based off the cathodic Tafel slope are shown in Table 9.1.

Table 9.1: Calculated values for the corrosion potential and the corrosion current for all specimens.

Specimen	E_{corr} (mV)	I_{corr} (μA)	Specimen	E_{corr} (mV)	I_{corr} (μA)
A1	-695.75	1.464	C3	-678.25	0.511
A2	-699.25	0.694	D1	-662.75	0.657
A3	-746.50	0.227	D2	-660.75	1.052
A4	-847.75	0.806	D3	-641.50	0.070
A5	-705.25	1.404	D4	-691.25	0.077
B1	-690.75	0.721	D5	-682.75	0.059
B2	-899.00	0.908	E1	-672.00	1.076
C1	-713.75	0.450	E2	-849.75	0.228
C2	-876.00	0.729	E3	-882.50	0.325

Many of the polarization curves that were measured as a part of this work, such as those shown in Figure 9.6, do exhibit this expected behavior. Though none of the samples tested showed a single breakdown potential, the presence of pitting, followed by re-passivation as indicated in the example above.

However, quite a few of those showed rapid fluctuations in the current, even as the curve progressed through the various reactions as expected. Some samples that

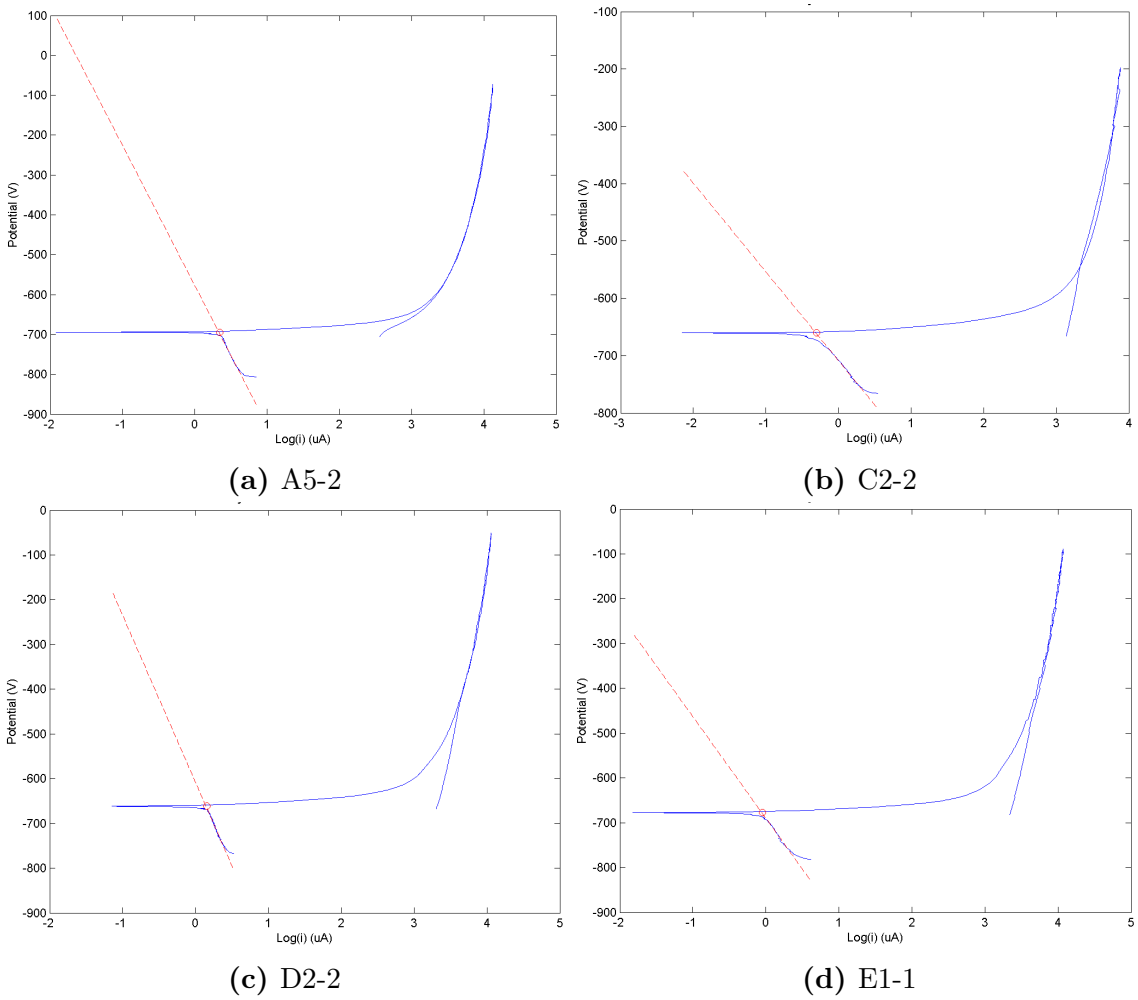

(a) A5-2 **(b)** C2-2

(c) D2-2 **(d)** E1-1

Figure 9.6: Representative potentiodynamic polarization curves showing the expected single breakdown potential with no pitting and re-passivation observed.

showed this behavior quite clearly are depicted in Figure 9.7. Just how a sharp steady increase in the current indicates pitting, sharp fluctuations in the current such as those seen here could be indicative of metastable pitting like that observed by Gupta et al. [2]. Most of the samples tested in this work show this type of behavior during the cathodic reaction, though a few, such as A3-1, experience it during the anodic reaction. Even the samples shown in Figure 9.6 exhibit this behavior, though the behavior is not as strong. Again, it is unknown if this behavior is the result of an environmental affect that was not controlled, a local heterogeneity in the exposed

microstructure, or if this behavior can actually be considered to be representative of the bulk material specimen being tested.

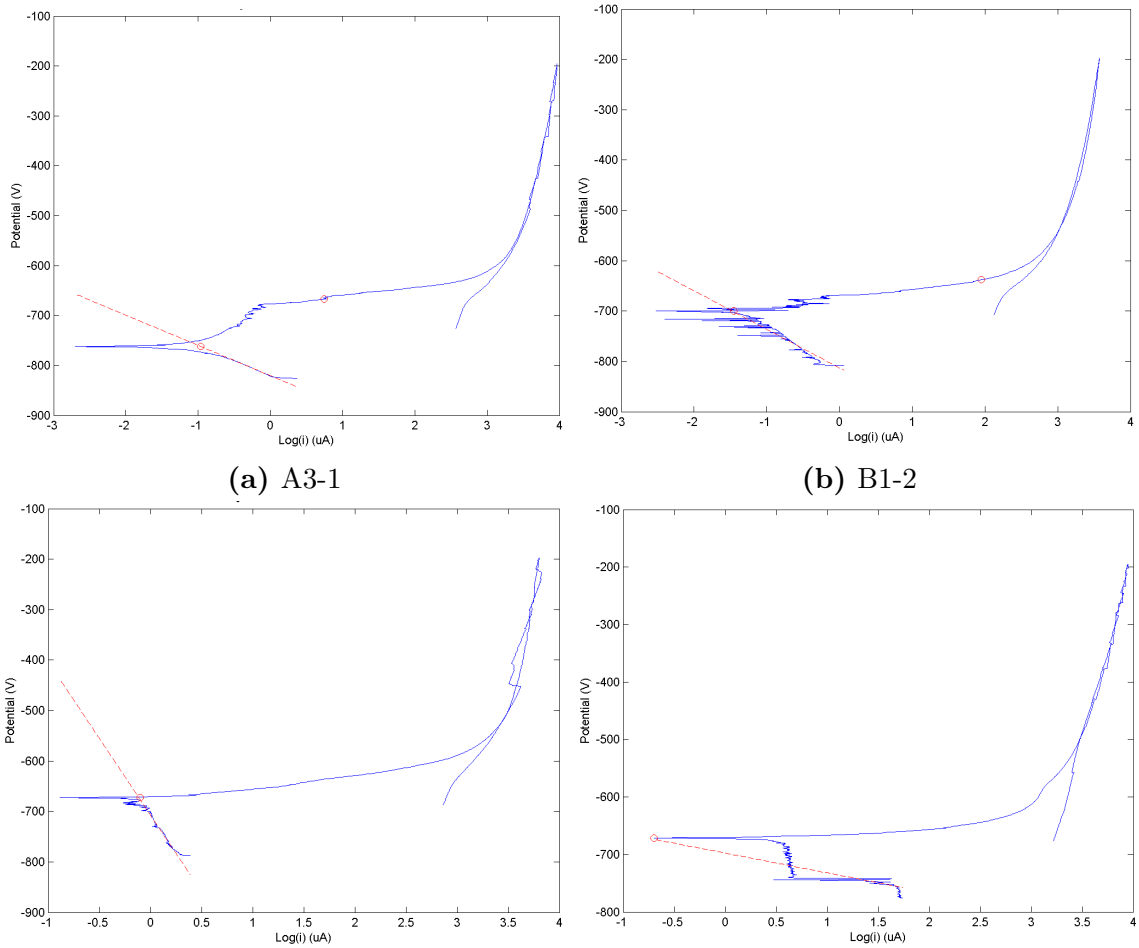

(a) A3-1 **(b)** B1-2

(c) C3-2 **(d)** D1-2

Figure 9.7: Representative potentiodynamic polarization curves showing the expected single breakdown potential with sharp variations in pitting that may indicate metastable pitting.

Unfortunately, some of the tests resulted in a messy, chaotic curve that only vaguely approximates a tafel plot. Some of these curves are shown in Figure 9.8. This noisey behavior is almost certainly indicative of a failed test, though it is unclear whether this failure is the result of an uncontrolled environmental effect or due again to a local heterogeneity within the microstructure such as the presence of a large constituent

particle or an oxide layer which has formed. Since additional variables have been introduced in to the system which have not been either measured or controlled, it is impossible to understand the significance of the behavior observed here.

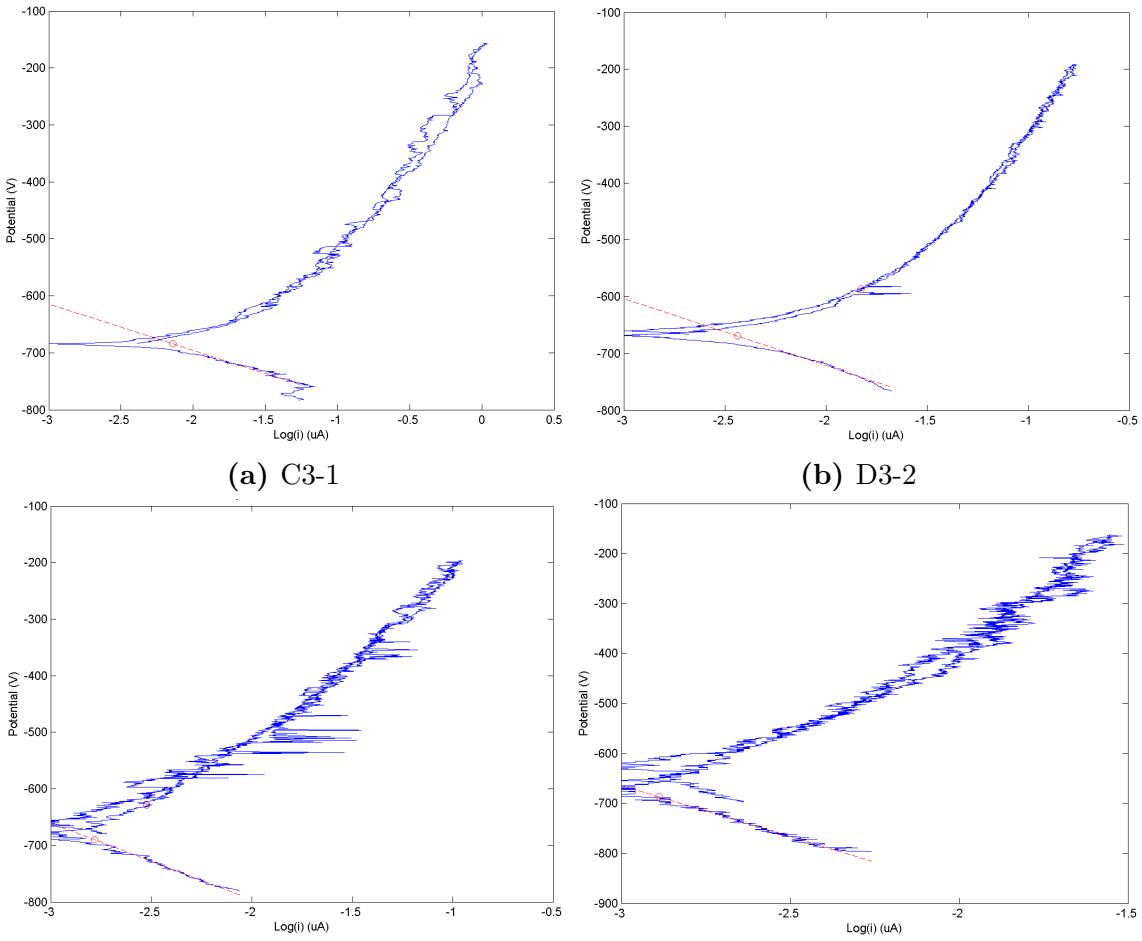

(a) C3-1 **(b)** D3-2

(c) D4-2 **(d)** D5-1

Figure 9.8: Representative curves showing the messy, chaotic behavior that was observed in some tests.

9.4 Summary

This work conducted potentiodynamic polarization and open circuit potential measurements aiming to determine if any of the various parameters that could be collected

might be potential candidates for quantitative measurements that indicate the relative likelihood for a material to undergo stress corrosion cracking. Some of the measurements that were suggested for examination were the steady state corrosion potential measured in open circuit potential tests, the corrosion potential E_{corr} measured in the polarization scans, the corrosion current I_{corr}, and the pitting potential E_{pit} if pitting was observed. It has been shown here that this testing method, which has recently become the preferred method of evaluating the relative corrosion susceptibility of aluminum alloys over the last decade, must be carefully understood and applied if meaningful experimental data is to be generated. In particular, these scans measure the local intergranular corrosion behavior of the material, and when only two samples per specimen are tested over a relatively surface area it is impossible to draw conclusions on the bulk behavior of the microstructure. In the future, additional work should be done to ensure that the sample size tested is sufficient enough to homogenize the system response so that conclusions about the bulk behavior can be made. Without the ability to control for this heterogeneity and without better control over potential environmental reactions within the system, this data cannot be used to explore PSPP relationships like those discussed in Chapter 4.

Once full potential scans are collected for the various samples, it should be possible to calculate the various breakdown potentials that are observed, and to estimate the corrosion currents associated with them. Other work recently reported in the literature suggests that the metastable pitting rate may be a good candidate for the types of measurements sought in this work, and qualitative observations of the data presented here confirm that the metastable pitting rate does change significantly with small changes in the microstructure. Further work should be done to evaluate the different corrosion current and potential pairs and the metastable pitting rates of the samples produced in this work, and to compare their values with high-fidelity

corrosion experiments to understand what these high-throughput values correlate to. Since potentiodynamic polarization testing has only recently become popularized as a high-throughput method in this material, it is important to make sure that these scans are being conducted in a manner to ensure consistent, accurate, and complete data is collected that will result in meaningful quantitative parameters that can be correlated to high-fidelity corrosion data. Until this is the case, correlation studies such as those that have been published over the last 3 years will remain in question.

9.5 References

[1] S. P. Knight, N. Birbilis, B. C. Muddle, A. R. Trueman, and S. P. Lynch. Correlations between intergranular stress corrosion cracking, grain-boundary microchemistry, and grain-boundary electrochemistry for al-zn-mg-cu alloys. *Corrosion Science*, 52:4073–4080, 2010.

[2] R. K. Gupta, A. Deschamps, M. K. Cavanaugh, S. P. Lynch, and N. Birbilis. Relating the early evolution of microstructure with the electrochemical response and mechanical performance of a cu-rich and cu-lean 7xxx aluminum alloy. *Journal of The Electrochemical Society*, 159:492–502, 2012.

[3] R. Goswami, S. Lunch, N. J. H. Holroyd, S. P. Knight, and R. L. Holtz. Evolution of grain boundary precipitates in al 7075 upon aging and correlation with stress corrosion cracking behavior. *Metallurgical and Materials Transactions A: Physical Metallurgy and Materials Science*, 44A:1268–1278, 2013.

[4] Princeton Applied Research. Application note corr-4: Electrochemistry and corrosion overview and techniques. www.princetonappliedresearch.com, Retrieved Jan 2016.

[5] Gamry Instruments. Application note: Getting started with electrochemical corrosion measurement. https://www.gamry.com/application-notes/corrosion-coatings/basics-of-electrochemical-corrosion-measurements/, Retrieved January 2016.

SIGNIFICANCE AND FUTURE WORK

In Part I of this work, we proposed a standard method of communicating information about the important variables that must be accounted for in a given materials design space, as well as the process-structure-property-performance (PSPP) relationships in-between them. Here we developed a PSPP map for wrought high-strength Al-Zn-Mg-Cu alloys which are typically utilized in aircraft applications by first examining the known knowledge database in this system to deduce what the important process, microstructure, and mechanical property variables were of interest. Once a PSPP map has been developed for a materials system, it is able to act as a living standard and to be continually updated as more information about the system is discovered. Additionally, these maps can be used to communicate information about models that are developed within this system. If a variable or mechanism which is depicted within the map, such as the ability to handle different recrystallized grain sizes, is not included in a computational modeling tool, then the map can be used to communicate the constraints of the model within the materials design space. Similarly, when experimental data is collected within this same space, the map can be used to clearly communicate which variables in the space were held constant, which variables were tracked and accurately measured, and if any variables were unaccounted for. This information can help to communicate what situations the data can be used in, and how the space that the experimental data can be used in is constrained.

In Part II of this work, we varied multiple parameters within such a materials design space and attempted to track and measure as many of the variables within the space as possible using commonly available testing and characterization methods. In

tackling such a large project in the complicated materials system of high-strength wrought Al-Zn-Mg-Cu alloys, we were able to understand which current testing and characterization methods are well suited to tracking these variables when the number test specimens becomes quite large and when variability among those specimens is involved. We were also able to identify opportunities for future work in this area, which could be focused on improving our ability to implement projects of the scope that is required here. In addition to evaluating the feasibility of the various measurement and characterization methods, the raw data and the analyzed results for this work are cataloged in an associated data repository and have been made available for use in future work in this and other areas.

In the microstructure characterization, discussed in Chapter 6, an increased ability to automatically analyze optical images, particularly when subjective decisions are required by the researcher, such as identifying a recrystallized grain boundary versus a subgrain boundary, could lead to faster analysis and data processing. Since the analysis of the images is one of the limiting steps in the amount of time required for characterization of that microstructural feature, improvements in this area could greatly speed up the entire characterization process. Additionally, combining traditional direct high resolution imaging methods, such as transmission electron microscopy, with indirect methods of characterizing nanometer size particles within the matrix like resistivity curves, could be a way of improving the amount of information that is collected on small scale microstructural features without significantly increasing the time, budget, and overall scope of projects beyond what exists now.

In many mechanical tests that are currently conducted, we introduce additional variables that are not currently included in the PSPP map, which must then also be held constant or must be tracked and measured. In the fracture toughness tests discussed

in Chapter 8, various aspects of the test must be optimized and tightly controlled to ensure that the threshold stress intensity is calculated for a plane-strain condition. Without these additional validity requirements, the measured value cannot be divorced from variables such as specimen geometry, fatigue pre-cracking history, or test loading conditions. If it is necessary to include one or more of these variables in the materials design space, the map can be updated to include them. However, it is far more preferable if they are either held constant, or if an alternative test method that is not a function of these additional variables, such as the methods proposed in the ASTM E1820 standard, are used instead. Similarly, in the corrosion tests discussed in Chapter 9, additional variables must be introduced. While stress corrosion cracking susceptibility is typically a property that is considered of much interest in this materials system, the work conducted here suggests that this should more properly be considered a material performance. Indeed, stress corrosion cracking, or environmentally assisted fracture, can be considered to be a performance parameter that is a combination of the ability of the material to resist fracture and to resist intergranular corrosion. If either of these properties is improved the resistance of the material to stress corrosion cracking should also improve. Based on the results of Chapter 9, in which we were unable to use the corrosion data collected to examine the structure-property correlations because of unaccounted variables such as environmental affects and local heterogeneity within the microstructure, we can update the map to better reflect the relationships and variables that must be accounted for in the system. The updated map then, would have intergranular corrosion located in the property column, with stress corrosion cracking in the properties column as a function of both fracture resistance and resistance of the material to intergranular corrosion. Additionally, the environment in which the corrosion is taking place is a directly controllable parameter that will affect various aspects of the microstructure and should be included in the processing column, perhaps as a service history.

Therefore, even though the data discussed in Chapter 9 was unable to be used to model the structure-property relationships as intended, it still yielded valuable information about the mechanisms within the system and resulted in an updated iteration of the PSPP map developed in Part I. As such, the PSPP map which was developed here as a standard method of communicating information about the important variables within the material system in addition to the relationships between them, does act as living standard. This is critical because material systems are being continuously improved and developed. Therefore, we expect that maps developed using the method proposed here will be able to successfully communicate what relationships in the material system have not been explored or are not adequately understood and successfully act as a living standard which can be continually updated and changed as new information becomes available.

VITA

Ashley Goulding grew up in Austin, Texas, where she attended St. Stephen's Episcopal School. Following encouragement from her physics teacher, Mr. Mikan, she decided after graduating to pursue an Engineering degree from Harvey Mudd College, which she obtained in 2011. While at Mudd, she conducted research in nanocomposite polymer memberanes for gas separation applications under Professor Nancy Lape before beginning her PhD in Materials Science and Engineering at Georgia Tech in the Fall of 2011. After a year of developing anode geometries for lithium-ion battery applications, she joined the Mechanical Properties Research Lab under Professor Richard Neu in June of 2012, and began jointly pursuing a Masters degree in Mechanical Engineering.